MUNI
PŘÍRODOVĚDECKÁ
FAKULTA

STUDYING THE HEATING/COOLING BALANCE IN GALAXY CLUSTER WITH THE ATHENA X-RAY OBSERVATORY

EVA BAŤKOVÁ

Školitel: prof. Mgr. Norbert Werner, Ph.D.
Ústav teoretické fyziky a astrofyziky
Přírodovědecká fakulta
Masarykova Univerzita

Brno – 2023

BIBLIOGRAFICKÝ ZÁZNAM

Autor:	Bc. Eva Baťková Přírodovědecká fakulta, Masarykova Univerzita Ústav teoretické fyziky a astrofyziky

Název práce:	Studie rovnováhy ohřívání/chlazení v kupě galaxií s rentgenovou observatoří Athena
Studijný program:	Fyzika
Obor:	Astrofyzika
Vedoucí práce:	prof. Mgr. Norbert Werner, Ph.D.
Akademický rok:	2022/2023
Počet stran:	xxiv + 83
Klíčová slova:	Kupy galaxií; Rentgenová spektroskopie; Multiteplotní plasma; Strojové učení; Analýza hlavních komponent; Random Forest klasifikátor; Observatoř Athena; Chandra satelit; Mise XRISM

BIBLIOGRAPHIC ENTRY

Author:	Bc. Eva Bať ková Faculty of Science, Masaryk University Department of Theoretical Physics and Astrophysics

Title of Thesis:	Studying the heating/cooling balance in galaxy cluster with the Athena X-ray observatory
Degree Programme:	Physics
Field of Study:	Astrophysics
Supervisor:	prof. Mgr. Norbert Werner, Ph.D.
Academic Year:	2022/2023
Number of Pages:	xxiv + 83
Keywords:	Galaxy clusters; X-ray spectroscopy; Multi-temperature plasma; Machine learning; Principal Component Analysis; Random Forest Classifier; Athena observatory; Chandra satellite; XRISM mission

ABSTRAKT

Kupy galaxií jsou jedny z nejhmotnějších gravitačně vázaných struktur ve vesmíru, které se skládají ze stovek až tisíců jednotlivých galaxií. Studium těchto masivních objektů může odhalit poznatky o vývoji velkorozměrových struktur, povaze temné hmoty nebo tepelných i netepelných procesech v mezigalaktickém prostředí. Pochopení složitých fyzikálních procesů v kupách galaxií však vyžaduje podrobnou spektrální analýzu rentgenového záření, která je časově náročná a se současnými metodami obtížně proveditelná. V této práci zkoumáme přístup strojového učení využívající *Analýzu hlavních komponent* s *Random Forest* klasifikátorem k analýze víceteplotních oblastí v kupách galaxií s využitím dat z rentgenové observatoře Athena, která poskytne tisíce spekter ke zpracování.

Efektivita metody byla také testována na simulovaných a reálných datech rentgenové observatoře Chandra, pro porovnání současných pozorovacích možností, a na simulovaných datech rentgenové zobrazovací a spektroskopické mise XRISM, která má své zahájení naplánované mnohem dříve než mise Athena a její parametry cílí k vyššímu spektrálnímu rozlišení než má observatoř Chandra. Naším cílem je vyvinout a prozkoumat méně výpočetně a časově náročnou metodu zpracování dat, která by mohla být v budoucnu implementována do spektrální analýzy reálných pozorování jako první krok pro nalezení žádoucích a zajímavých oblastí.

ABSTRACT

Galaxy clusters are the most massive gravitationally bound structures in the universe, consisting of hundreds to thousands of individual galaxies. Studying these massive objects can reveal insights into the evolution of large-scale structures, the nature of dark matter, or the thermal and non-thermal processes in the intra-cluster medium. However, understanding the complex physical processes in galaxy clusters requires detailed spectral analysis of the X-ray emission, which is time-consuming and challenging to do with current methods. In this study, we explore a machine learning approach based on *Principal Component Analysis* with *Random Forest Classifier* to analyze the multi-temperature regions in galaxy clusters using data from the Athena X-ray observatory, which will provide thousands of spectra to process.

The effectiveness of the method was also tested on simulated and real data from the Chandra X-ray Observatory to compare the current observational capabilities and on simulated data from the upcoming X-ray Imaging and Spectroscopy Mission XRISM, which is scheduled to launch earlier than the Athena mission and whose parameters aim for higher spectral resolution than Chandra. Our aim is to develop and study a less computationally and time-consuming method of processing spectral data that could be in the future implemented in the spectral analysis of real observations as the first step to finding desired and interesting regions.

MUNI
SCI

MASARYKOVA UNIVERZITA
PŘÍRODOVĚDECKÁ FAKULTA
KOTLÁŘSKÁ 2, 611 37 BRNO
IČ: 00216224
DIČ: CZ00216224

ZADÁNÍ
DIPLOMOVÉ PRÁCE

Akademický rok: 2022/2023

Ústav:	Ústav teoretické fyziky a astrofyziky
Studentka:	Bc. Eva Baťková
Program:	Fyzika
Specializace:	Astrofyzika

Ředitel *ústavu* PřF MU Vám ve smyslu Studijního a zkušebního řádu MU určuje diplomovou práci s názvem:

Název práce:	Studying the heating/cooling balance in galaxy cluster with the Athena X-ray observatory
Název práce anglicky:	
Jazyk závěrečné práce:	angličtina

Oficiální zadání:
We will investigate the capability of the Athena X-ray observatory to determine the atmospheric cooling rates by using temperature-sensitive line ratios over a broad temperature range. Deep observations of nearby galaxy clusters with the Athena X-IFU will produce thousands of high resolution spectra the analysis of which would be demanding if not impossible with current techniques. We will introduce and discuss new data analysis techniques for maximum utilisation of the rich X-IFU data. These techniques, which employ elements of machine learning, allow us to use spectral and spatial information optimally, while speeding up the data analysis considerably

Vedoucí práce:	prof. Mgr. Norbert Werner, Ph.D.
Konzultant:	Dr. Martin Topinka, PhD. Mgr. Tomáš Plšek
Datum zadání práce:	16. 11. 2021
V Brně dne:	14. 5. 2023

Zadání bylo schváleno prostřednictvím IS MU.

Bc. Eva Baťková, 16. 12. 2021
prof. Mgr. Norbert Werner, Ph.D., 7. 1. 2022
Mgr. Dušan Hemzal, Ph.D., 25. 1. 2022

ACKNOWLEDGEMENTS

First and foremost, I would like to thank my supervisor, Norbert Werner, and my consultant, Tomáš Plšek, for their guidance, patience, and support throughout the process. Their knowledge and expertise have been instrumental in shaping the direction of this work.

Special thanks go to Carter Rhea, who not only provided me with academic expertise and his *Pumpkin* code for multi-temperature analysis but also showed a genuine interest in my professional development. I would also like to thank all members of the High Energy Astrophysical group for their insightful comments, critiques, and suggestions that have helped me to improve the quality of my research.

Finally, I would like to express my wholehearted appreciation to my husband and the entire family for their unwavering support, encouragement, and understanding throughout my academic journey.

Overall, thank you to everyone who has helped to make this thesis possible.

DECLARATION

Hereby I declare that I have prepared my diploma thesis independently under the guidance of the supervisor with the use of cited works.

Brno, 2023

Eva Baťková

The universe is like a safe to which there is a combination,
but the combination is locked up in the safe.

— **Richard Feynman**

CONTENTS

LIST OF FIGURES

LIST OF TABLES

LIST OF SYMBOLS

ρ	Plasma density
ρ_{DM}	Dark matter density
v	Fluid velocity; Particle velocity
e, q	Electron charge
Φ	Gravitational field
T	Energy per particle
n_H	Hydrogen number density
n_e	Electron number density
n_i	Ion number density
Λ	Cooling function
G	Gravitational constant
P	Power radiated by single particle
c	Speed of light
Z	Charge of an ion
m_e	Electron mass
b	Shortest distance between electron and nucleus
x	Variable distance between electron and nucleus
g_{ff}	Gaunt factor
k_B	Boltzmann constant
r	Distance from the GC center
$M(r)$	Enclosed mass within the radius r
$\dot{M}_{cool}$	Cooling rate
T_X	Global temperature of cluster
R	Universal gas constant [J mol^{-1} K^{-1}]
r_{ij}	Original spectral data
C_jk	Covariance matrix; Transition probability coefficient

X	M-dimensional vector representing spectrum
λ	Eigenvalue
$\vec{e}$	Eigenvector
$\vec{\mu}$	Mean spectrum
a_{ij}	Original values projected into principal component basis
$\sigma(E)$	Absorption cross-section of neutral hydrogen
D_A	Angular diameter distance [cm]
g	Statistical weight
z	Redshift
N_1^{min}	Minimum normalization range for the main thermal component
N_1^{max}	Maximum normalization range for the main thermal component
N_2^{min}	Minimum normalization range for the second cooler thermal component
N_2^{max}	Maximum normalization range for the second cooler thermal component
N_3^{min}	Minimum normalization range for the third cooler thermal component
N_3^{max}	Maximum normalization range for the third cooler thermal component
R^{min}	Ratio between the minimum normalization values of the second and first components.
$R_{2/1}$	Ratio between normalization of the second and first components ($= N_2/N_1$).
M_{acc}	Prediction accuracy of our trained models
C_{var}	Parameter variability coverage of our models
A_i	Number of observed counts in the spectrum
E_i	Number of predicted counts in the spectrum
χ^2_R	Reduced χ^2 statistic

INTRODUCTION

The majority of baryonic matter in galaxy clusters (GCs) exists in the form of hot gas emitting X-ray radiation. The origin of this emission was proposed only recently and was initially met with skepticism (Gorenstein P. et al., 1973; Gursky H. et al., 1971). First observations proving this theory were done by Ariel V Sky Survey Experiment, which discovered a bump in the spectrum corresponding to an iron line and thus confirmed that the X-ray emission originates from thermal plasma within the cluster (Mitchell R. J. et al., 1976).

The confirmation of the origin of this emission marked a significant breakthrough in our understanding of the intracluster medium (ICM). The ICM is a dynamic and complex environment, and its properties are shaped by various physical processes such as heating, cooling, and turbulence (Böhringer H. et al., 2007; Fujita Y. et al., 2020). By studying the heating and cooling balance of the ICM, we can gain insight into the processes that regulate its temperature, pressure, and entropy profiles. These properties can provide us with a deeper understanding of the formation and evolution of GCs, as well as the role of feedback from active galactic nuclei, supernovae explosions, or thermal conduction in shaping them (Yang H.-Y. K. and Reynolds Ch. S., 2016).

Scheduled for launch in the early 2030s, the *Athena* mission promises to deliver unparalleled capabilities for investigating the heating and cooling balance in GC. With cutting-edge X-ray spectroscopy, imaging, and timing technologies, *Athena* will enable high-resolution mapping of the thermodynamic properties of the ICM with exceptional precision, facilitating deeper exploration and understanding of the characteristics of GC (Nandra K. et al., 2013). Moreover, the *Athena* instruments are designed to perform with remarkable sensitivity and broad energy coverage, which will allow the detection of faint X-ray lines and thus unlock a profound understanding of the underlying properties and dynamics of GC (Lotti S. et al., 2021).

This study is motivated by the large number of high-resolution spectra that are expected to be produced by *Athena*'s deep observations with an X-IFU detector. Analyzing all these spectra manually using current XSPEC analysis procedures would be a very demanding and time-consuming task. In response to this challenge, machine learning (ML) techniques have gained popularity in astrophysics for analyzing such large datasets. The ability of ML algorithms to quickly and accurately identify trends and patterns in complex data sets has made them an invaluable tool in various fields (Belabbas M. A. and Wolfe P. J., 2021; Ntampaka M. et al., 2019; Rhea C. et al., 2021; VanderPlas J. et al., 2012).

In order to gain a better understanding of the thermodynamic state of GC, it is crucial to identify the number of underlying components in their spectra. In this thesis, we aim to advance our understanding of the thermodynamic properties of galaxy clusters by utilizing machine learning techniques to identify the multi-temperature components present in spectra simulated for the *Athena* mission. Additionally, these techniques were investigated on simulated spectra for the *Chandra* and *XRISM* satellites to compare their capabilities.

In Chapter 1, we outline the fundamental characteristics of galaxy clusters, highlighting the significance of their intracluster medium and X-ray emission in determining their thermal structure. This Chapter also explores the theoretical background of the heating and cooling processes in these clusters, as well as the challenges posed by existing theories. Chapter 2 is dedicated to the observatories *Chandra, XRISM* and *Athena*, their description, and technical specifications. The analysis techniques we used for data handling are presented in Chapter 3. Chapter 4 gives a detailed insight into the methodology and our models, as well as their application to real observations and comparison with the XSPEC platform. Finally, in Chapters 5 and 6, we provide a summary of our research, including the key takeaways and directions for future investigation.

1

CLUSTERS OF GALAXIES

Galaxy Clusters (GC) are massive, gravitationally bound structures that contain hundreds to thousands of galaxies. The total mass of these objects goes from 10^{14} to above 10^{15} $M_\odot$ (Peterson J.R. and Fabian A.C., 2006). To depict a full image of the GCs, such as their mass distribution or the information about all the obscured physical processes, the observational studies developed into broad, multi-wavelength fields. One of the fields focuses on the bright X-ray emission, which is a good tracer of hot, intracluster plasma trapped in the GC's potential well and represents most of the baryonic matter in the cluster (see Figure 1.1). The trapped gas has a temperature up to several keV ($\sim$ millions of Kelvin), thus making GCs one of the most luminous X-ray emitters in the universe (Böhringer H., 2002).

Figure 1.1: Observations of Abell 1689 galaxy cluster obtained by Hubble Space Telescope (on the left) and the same image combined with X-ray observation from *Chandra* X-ray Observatory (on the right). Hot intracluster gas is represented by the purple color. Adapted from NASA et al., 2022.

Early observations showed the hot intracluster medium (ICM) at a typical temperature around T $\sim 10^8$ K (Sarazin C. L., 1986). The relation between the cluster temperature and their total X-ray luminosity L_X in the absence of gas cooling and heating emerging from simulations of cluster formation is proportional to T^2. However, observations and recent studies using methods to correct selection bias follow L-T relation $L_X \propto T^3$ (Connor T. et al., 2014; Ettori S. et al., 2004; Giles P. A. et al., 2016). Numerous possible scenarios were presented to explain this deviation from theoretical expectations, including mainly non-gravitational energy input, such as supernovae feedback,

pre-heating, thermal conduction, or heating from active galactic nuclei (AGN). Most of these mechanisms were and still are being investigated (Fujita Y. et al., 2020; Jennings F. et al., 2022; Ubertosi F. et al., 2022). Although satellites have made significant efforts to collect data with sufficient resolution, there is still a need for better data acquisition capabilities, particularly in the softer energy band, to enable a more thorough analysis.

With current satellites, such as the *Chandra X-ray observatory*, the temperature measurements and identification of multi-temperature plasma in GCs are technically challenging. However, future X-ray missions will be able to provide the necessary resolution and thus revolutionize our understanding of the energy transfer into the ICM and the processes behind it (see Chapter 2).

1.1 THE INTRACLUSTER MEDIUM

The intracluster medium consists of hot, diffuse, X-ray-emitting plasma representing approximately 85% of the baryonic matter in the cluster. The composition of the ICM is mainly ionized hydrogen and helium. The medium is also enriched with heavier elements (Sparke L. S. S., 2007), whose quantity rises towards the center of GC along with the X-ray brightness (see Figure 1.1).

The dissipative physics of baryons and detailed modeling of the non-gravitational processes in the core are the key requirements for the full description of cluster formation (Kravtsov A. V. and Borgani S., 2012), and this field still faces more open questions regarding the energy transport between the cluster core and the ICM than answers. However, some promising theories suggest that part of the energy might be transported by bubble-generated turbulence (Norman M. L. and Bryan G. L., 1999) or sound waves (Ruszkowski M. and Begelman M. C., 2002). Additionally, the observations of ICM revealed a complex multi-phase structure within several tens of kpc from the cluster's center (see Figure 1.2), containing volume-filling hot X-ray emitting gas ($\geq 10^8$ K) with dense cold co-existing structures ($\geq 10^4$ K), possibly formed by local thermal instabilities (Das H. K. et al., 2021; Yang H.-Y. K. and Reynolds Ch. S., 2016). The existence of these cold gas clouds is closely related to one of the biggest open problems of cluster physics known as *cooling flow problem*, described in detail in Section 1.4.3.

On large scales, the ICM plasma can be described by magneto-hydrodynamic (MHD) equations while assuming an optically-thin plasma in collisional equilibrium (more in Section 1.3). The equations can be significantly simplified for the case of unmagnetized single subsonic flow in a steady state with neglection of viscosity, resistivity, conduction terms, and assumption of spherical symmetry. The first equation 1.1 is the mass conservation equation outlining the constant mass of the fluid as:

$$\nabla \cdot (\rho \vec{v}) = 0. \tag{1.1}$$

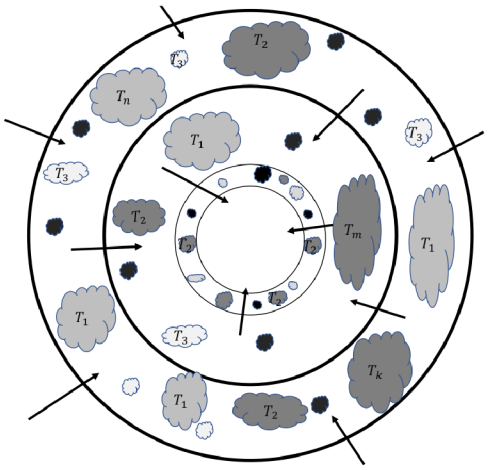

Figure 1.2: Schematic illustration of gas clouds with different temperature distributions due to local cooling (represented by arrows) and heating flows. Adapted from Haghighi M. H. Z. et al., 2019.

The second equation 1.2 expresses momentum conservation with gravitational compression term on the left side and thermal pressure term on the right side:

$$\rho \frac{d\Phi}{dr} = \frac{d(\rho T)}{dr}. \tag{1.2}$$

The third equation 1.3 is the energy equation, where the left side describes the compression and energy of the plasma, and the right side outlines the energy loss due to radiative cooling with the potential interactions between other matter (cosmic rays, dust, dark matter) and studied plasma:

$$\rho v \frac{d}{dr}\left(\frac{5}{2}T - \Phi\right) = -n_e n_H \Lambda(T, Z) + \text{interactions}. \tag{1.3}$$

The last, fourth equation 1.4, sets the gravitational field with the contribution of both the plasma and dark matter:

$$\frac{d}{dr}\left(r^2 \frac{d\Phi}{dr}\right) = 4\pi G(\rho + \rho_{DM}). \tag{1.4}$$

The individual variables describing the four MHD equations are the density ρ, the fluid velocity v, the gravitational potential Φ, the temperature T express the energy per particle, the electron and hydrogen number densities n_e, n_H, the cooling function $\Lambda(T, Z)$, the density ρ and the dark matter density ρ_{DM} (Peterson J.R. and Fabian A.C., 2006). Understanding these equations and their implementation for more generic models is crucial for explaining future observations with more sensitive detectors.

1.2 X-RAY EMISSION

Thorough observations and imaging of the heart of GCs revealed the presence of many exciting features, such as cavities, line-emitting filaments, and weak shocks. In theory, X-ray instruments could enable distinguishing some of these non-thermal processes. However, in practice, the detection of their signature X-rays is limited by the instrument's resolution, and most of their emission is overshadowed by the dominant thermal ICM signal. This obscured field thus opens many opportunities for future X-ray missions, including the *Athena* and *XRISM* observatory. With their new spectrometers, it will be possible to detect the fine resonant scattering effect, non-equilibrium, non-thermal ionization, or line emissions yet unseen.

Three fundamental emission processes contribute to the radiation from ICM: Bremstrahlung radiation (free-free emission), recombination (free-bound emission), and de-excitation (bound-bound emission). The first two processes produce continuum radiation, and the final process gives rise to line radiation (Fabian A. C. and Ross R. R., 2010). The ICM's very low plasma density allows for the occurrence of all 'forbidden' transitions. Consequently, to accurately model the spectral spectrum of thermal plasma, we have to take into consideration all the ion-electron collisional rates along with their branching ratios (Böhringer H. and Werner N., 2010).

In the low-density ICM, the collision rates between electrons and ions in the thermal plasma depend on the temperature. The shape of the resulting spectrum is dictated by the temperature and chemical composition of the plasma, while its normalization is directly proportional to the densities of electrons and ions under the assumption of a low plasma density limit.

1.2.1 *Thermal Bremsstrahlung*

In the ICM of a galaxy cluster, the essential source of continuum emission and thus the most crucial contributor to the cooling mechanism for high-temperature plasma is the *Bremstrahlung* or *free-free emission*. Radiation from this process arises from an acceleration of a charged particle in the Coulomb field of another charged particle. Power radiated by a single particle P is given by Larmor's formula first stated in 1897 (Larmor J., 1897):

$$P = \frac{2}{3}\frac{e^2\dot{v}^2}{c^3}, \tag{1.5}$$

where e is the elementary charge, $\dot{v}$ its proper acceleration derived from Coulomb's law $\dot{v} = Ze^2/(m_e x^2)$, where Z is the ion's charge, m_e is the mass of the lightest particle

(electron in our case), x is the distance between the electron and the nucleus, and c is the speed of light (see Figure 1.4). The total energy emitted in the interaction is:

$$P\Delta t = \frac{2e^2}{3c^3}\left(\frac{Ze^2}{m_e x^2}\right)2\tau, \tag{1.6}$$

where τ represents the collision time defined as $\tau \equiv b/v$. Parameter b is the distance of the closest approach between the two interacting particles, and v is the relative velocity at which the particles approach each other before the interaction.

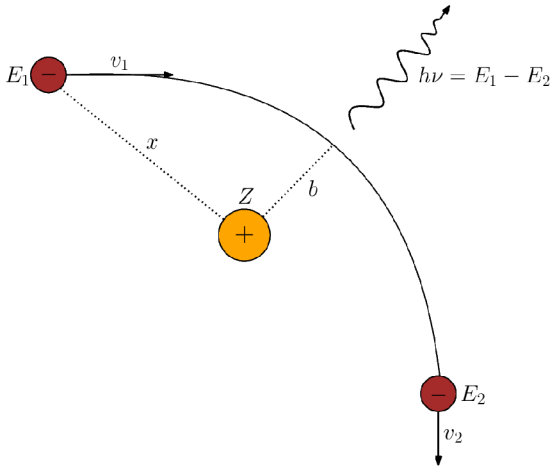

Figure 1.3: Schematic illustration of Bremsstrahlung produced by a deflection of a high-energy electron in the Coulomb field of an atomic nucleus (own illustration).

Since the emissivity is defined as the energy emitted per frequency ν, volume V, and unit time, the emissivity of free-free interaction is defined as:

$$\epsilon^{ff} = \frac{2^5 e^6}{3m_e c^2}\left(\frac{2\pi}{3m_e k_B T}\right)^{1/2} Z^2 n_e n_i g_{ff}(Z,T,\nu)\exp\left(-h\nu/k_B T\right), \tag{1.7}$$

where k is the Boltzman constant, T is the kinetic temperature of electrons n_e, n_i are the electron and ion number densities, and $g_{ff}(Z,T,\nu)$ is the Gaunt factor. This factor corrects for the quantum mechanical effects, and its values for the intracluster plasma can be found in Nozawa S. et al., 1998. The equation 1.7 indicates that the X-ray spectrum is nearly exponentially dependent on the frequency, meaning that the emission should quickly fall off at high frequencies, as is observed.

1.2.2 *Line emission*

Although current instruments for spectral analysis are known to have limited resolution for detecting fine structures of spectral lines, significant improvements were

made in studying the intercluster medium (ICM). These include the discovery of fundamental elements in the ICM (Mushotzky R. et al., 1996), the absence of cold gas in the cores of galaxy clusters observed by *XMM-Newton* (PetersonJ. R. et al., 2001), and the recent detection of Fe-peak elements by the micro-calorimeter onboard the *Hitomi* observatory (Hitomi Collaboration et al., 2018a).

In the energy range of $1 - 10$ keV, where most of the radiation of a typical GC is emitted, the emission lines arise from transitions between the inner shell states of heavy elements such as oxygen, neon, and iron. These transitions can originate from several processes, such as ionization, excitation, resonant scattering, and following radiative cascades (Bonamente M. et al., 2002). In the soft X-ray range, the Fe-L and Fe-K lines are particularly important due to their strong emission and characteristic properties that can be examined (Lindtroth E. and Indelicato P., 1993).

The Fe-L complex, which spans the energy range of $0.7 - 1.1$ keV, is a mix of many lines from different charge states of iron. The ratios of Fe-L lines to themselves and other lines such as the H-like and He-like oxygen lines can be used as diagnostic tools for determining the temperature and metallicity of the ICM (Werner N. and Mernier F., 2020). On the other hand, the Fe-K line at 6.7 keV is produced by transitions between the K and L shells of iron and can provide information about the ionization state of the gas and the presence of a turbulence (Urdampilleta I. et al., 2019).

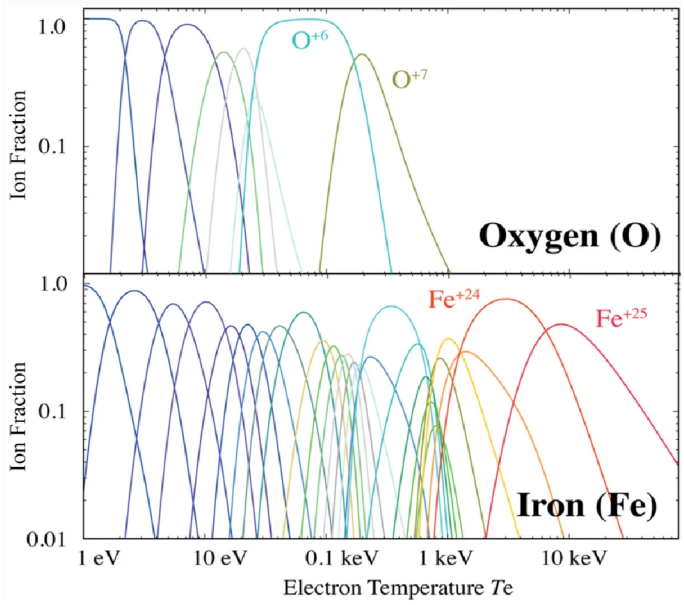

Figure 1.4: Example of ion fraction for Oxygen and Iron in collisional ionization equilibrium as a function of temperature, where the different ionization states are represented by different colors. Adapted from Ezoe Y. et al., 2021

If the gas can be described as a single-temperature plasma in collisional ionization equilibrium (see Section 1.3), the temperature determined from the mentioned ratios should match the temperature obtained from the continuum shape. Any deviations from a single-temperature CIE plasma may indicate the existence of a multi-temperature or non-equilibrium ionization region (Hitomi Collaboration et al., 2018b).

1.3 COLLISIONAL IONIZATION EQUILIBRIUM

The X-ray emission from ionized atoms can exhibit complex behavior. However, when it comes to plasma on larger scales such as in the GCs, several approximations, collectively known as the *coronal approximation*, can effectively capture its properties. These approximations depict an image of optically-thin plasma in collisional equilibrium.

The first estimate assumes that photons do not interact with ions or electrons, making photo-excitation and photo-ionization processes relatively rare compared to collisional processes. This statement is suitable for describing larger scales in galaxy clusters, where radiation densities are very low. However, some strong emission lines may still exhibit spectral and spatial distortions due to resonant scattering.

The second estimate assumes that all electrons are in their ground state, which cannot be described using the commonly used Boltzmann distribution in the local thermodynamic equilibrium (LTE) approximation. However, this approximation only holds when excitations dependent on density are less frequent than radiative decays at densities below $< 10^{10}$ cm^{-3}. This condition is met in the ICM as both the electron and radiation densities are $< 10^{-1}$ cm^{-3} (Dekel A. and Ostriker J.P., 1999).

The final assumption is that the plasma's age or cooling time (see section 1.4.2) significantly exceeds the time scale of elastic collisions between particles. As a result, the free particles will eventually relax to a Maxwellian distribution around a single kinetic temperature, known as the general kinetic temperature.

Despite their usefulness, these approximations limit our ability to study obscured non-thermal processes, which are tangled in the web of hot intracluster plasma.

1.4 STANDARD COOLING FLOW MODEL

The Standard Cooling Flow Model is a widely accepted theoretical model suggested to occur in various environments, from clusters of galaxies (Fabian A. C. et al., 2022) to accreting white dwarfs in binary systems (Goldman S. R. et al., 2022; Munari U. et al., 2022), where the cooling flow is present in the material, which is settling onto the surface from the accretion disk and has to dissipate its rotational energy. The model was first proposed by Fabian in 1984 (Fabian A. C. et al., 1984) and has since been refined and improved by many authors.

The model simplifies the physics of general flows based on the assumption that the gas is in hydrostatic equilibrium and is cooling dominantly through radiative processes, which in GCs leads to a cooling flow that transports mass and energy from the center of the cluster to the outer regions. The model also neglects any heating processes, which can transport thermal energy into cold gas clouds.

1.4.1 *Hydrostatic equilibrium*

Hydrostatic equilibrium is an inseparable part of the Standard Cooling Flow Model. It is the state in which the gravitational forces acting inward are balanced by the pressure of the hot gas pushing outward, resulting in a stable system. In spherical symmetry, the equation describing this balance is:

$$\frac{dP_{\text{gas}}}{dr} = -\rho(r)\frac{GM(r)}{r^2}, \tag{1.8}$$

where $\frac{dP}{dr}$ is the gradient of the gas pressure to the radius, $\rho(r)$ is the gas density as a function of radius, G is the gravitational constant, $M(r)$ is the mass enclosed within a radius r, and r is the distance from the center of the cluster.

1.4.2 *Cooling rates*

The ICM is depicted as a hot, ionized, dense environment that emits photons mainly in the X-ray band. This leads to substantial energy losses and cooling (radiative cooling), particularly in the central brightest X-ray regions of the galaxy cluster. The simple estimation of ICM's susceptibility to radiative cooling can be obtained by analyzing the timescale, during which the gas can continuously release energy at its present rate (Sanderson A. J. R. et al., 2006). The timescale for the ICM to dissipate all its energy through cooling is called the 'cooling time'. If the pressure in the ICM is constant, the cooling time of a plasma t_{cool} is determined as:

$$t_{\text{cool}} \equiv \frac{3nk_{\text{B}}T}{2n_i n_{\text{e}}\Lambda(T,Z)}, \tag{1.9}$$

where n is the particle number density, k_{B} is the Boltzmann's constant, T is the gas temperature, n_i and n_e are the ion and electron number density, and $\Lambda(T,Z)$ is the cooling function dependent on both temperature T and metallicity Z. Defined cooling time can be interpreted as the thermal energy $\frac{3}{2}k_{\text{B}}T$ divided by energy loss per unit volume.

The gas in the central part of GCs has a radiative cooling time approaching 5×10^8 yr (Haghighi M. H. Z. et al., 2019), which is much shorter than the age of the cluster itself. From the view of the standard cooling flow model, this indicates the presence of

cooling flows. The cooling rate (mass deposition rate within the cooling flow model) in the absence of heating $\dot{M}_{\rm cool}$ can be calculated from the excess X-ray luminosity $L_{\rm X}$ as:

$$L_{\rm X} = \frac{5}{2}\frac{\dot{M}_{\rm cool}}{\mu m} k_{\rm B} T, \tag{1.10}$$

where μm is the mean mass per particle and T is the gas temperature. Typical cooling rates are predicted to range between 10 to 100 $M_{\odot}{\rm yr}^{-1}$, which would result in strong spectral line emission in the soft X-ray band (Liu H., 2021). However, no evidence of such extreme cooling is evident from the current high-resolution spectroscopy observations (see Section 1.4.3).

1.4.3 *Cooling flow problem*

The cooling flow problem in galaxy clusters is a long-standing issue in astrophysics that refers to the discrepancy between the predicted and observed amount of gas cooling in the center of clusters. Theoretical models indicate that the gas located in the central regions of galaxy clusters should go through rapid cooling and condensation, resulting in a high star formation rate in this region, which is not observed (McDonald M. et al., 2013; McNamara B.R. and Nulsen P.E.J., 2007; Werner G. R. et al., 2018). Observations also suggest that while the cooling flow model seems to agree with the data at higher temperature ranges, it falls short in the soft X-ray band. At lower temperatures, the model captures Fe XVII lines that are not evident in the observed data. (see Figure 1.5).

Mathematically the cooling flow problem could be described by a set of equations (continuity equation, momentum equation, energy equation, radiative transfer equation) that model the evolution of the ICM and take into account various physical processes such as radiative cooling and heating (Voit G. M., 2005).

One promising solution to the cooling flow problem is a mechanism that heats the gas in cluster cores and prevents it from cooling as quickly as expected. Therefore, the energy equation can be modified to include heating sources, which can provide additional energy to the gas and counteract the cooling. Another potential solution to the cooling flow problem could be provided by non-thermal mechanisms in the ICM. For example, magnetic fields or cosmic rays could impact the detected X-ray radiation and diminish the apparent cooling rates of the gas (Peterson J.R. and Fabian A.C., 2006).

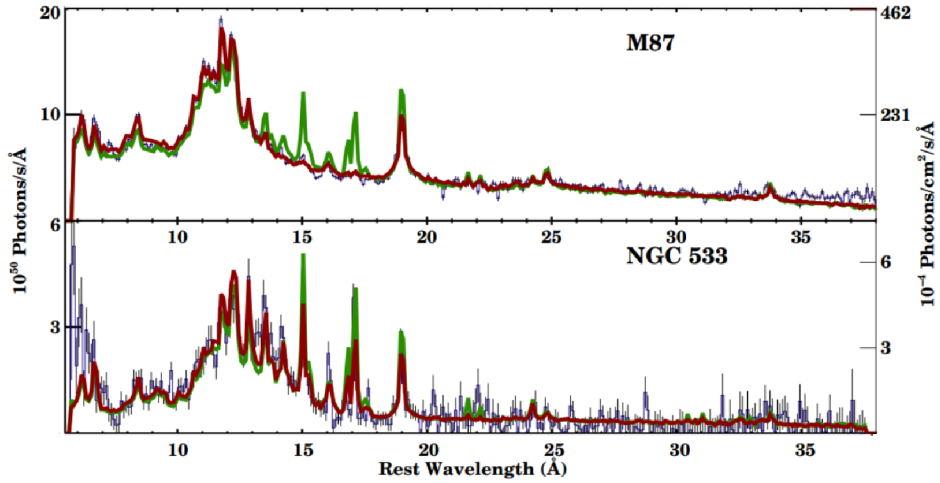

Figure 1.5: Spectra from Chandra satellite of M87 and NGC533 (blue line) fitted with standard cooling flow model (green line), where the red line represents fit that allows the normalization of the cooling flow model to be adjusted for several temperatures. Adapted from Peterson J. R. et al., 2003

1.4.4 *Heating vs cooling*

The first thorough overview of the temperature structure of the GCs was depicted in Pratt G. W. et al., 2007, which analyzed X-ray temperature profiles of 15 nearby representative clusters (see Figure 1.6).

These results and other observations of the cores of galaxy clusters have revealed their several underlying X-ray properties. At small radii, we observe profound changes in the temperature profiles, which are specific for two types of observed clusters: cool core (CC) clusters with high-density cores and decreasing temperatures towards the center, resulting in short cooling times for the ICM; and non-cool core (NCC) clusters, with moderate densities (below 10^{-2} cm^{-3}), flat temperature profiles and longer central cooling times. Additionally, cool core clusters show a very bright peak in X-ray surface brightness. The CC cluster scenarios were found in at least 50% of the observed GCs (Fabian A. C., 1994) and imply the existence of cooling flows. Since the standard cooling flow scenario does not represent well the spectra in the entire X-ray band of the GC as we established earlier, recent research has focused on finding a suitable mechanism that would fill these missing gaps in our theories. However, before delving into potential solutions, let us examine the issue more closely.

The basic assumption for the cooling flow model was that the X-ray photons come from the thermal energy content of the ICM. If the gas at the center of clusters were not disturbed or mixed with the outer part of ICM, the gas would cool radiatively. Thus all the energy that escapes from the core is in the form of X-ray photons which we detect (Sarazin, C.L., 2007). As the center of GCs loses enormous amounts of energy,

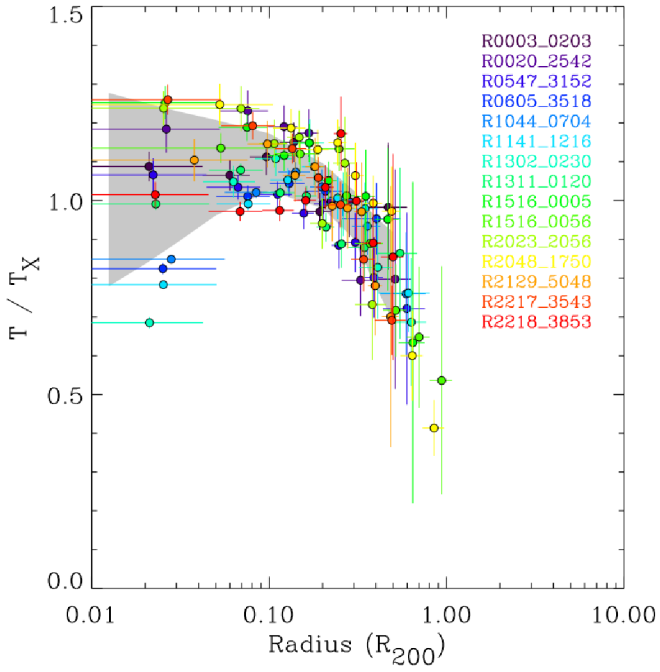

Figure 1.6: Projected temperature profiles of 15 nearby GCs, normalized by a global temperature of the cluster T_X. Adapted from Pratt G. W. et al., 2007.

the temperature of the attending gas drops, and the pressure will decrease simultaneously concerning the state equation $pV = nRT$. The weight of the surrounding gas will compress the central cooling gas, and it will start to fall toward the center of GC. The density in the core increases, causing the gas to heat up and thus emit more X-ray photons carrying away the core's energy, further cooling the center. If this scenario was correct and no heating processes were present to balance the cooling, we should observe catastrophic cooling in the central regions of GC. However, this extreme cooling and associated star formation have not yet been observed, thus giving rise to the theoretical research of possible heating sources present in the system (see for example, Ley F. et al., 2022; Nath B. B. and Roychowdhury S., 2002; Petrosian V. and East W. E., 2008).

During the early stages of hierarchical structure formation simulations, the models considered only the gravitational effects, but soon it became clear that clusters did not follow these predicted self-similar relations. Consequently, non-gravitational heating effects, such as supernovae and AGN feedback, were necessary to be incorporated. Recent models and observations suggest that the AGN is the most probable source of heating, capable of preventing the ICM's runaway cooling (refer to Figure 1.7). The feedback is provided through the accretion of infalling material onto a supermassive black hole (SMBH), which self-regulates its fuel supply by either radiation pressure or mechanical energy (Calzadilla M. S. et al., 2022).

Although heating is considered a feasible approach to counterbalance cooling flows, its effectiveness relies heavily on precise adjustments. Excessive heat generation can disperse both the dense gas cores and cooling flows that have been observed. Moreover, the presence of entropy profiles that progressively increase towards the cluster's outer regions (refer to Figure 1.8) raises yet another question: how can the heating sources operate without disrupting these entropy profiles and, subsequently, causing heat dissipation through convection (Böhringer H. and Werner N., 2010). These discoveries emphasize the importance of delving deeper into understanding how nature achieves such a delicate balance, making this an exciting topic.

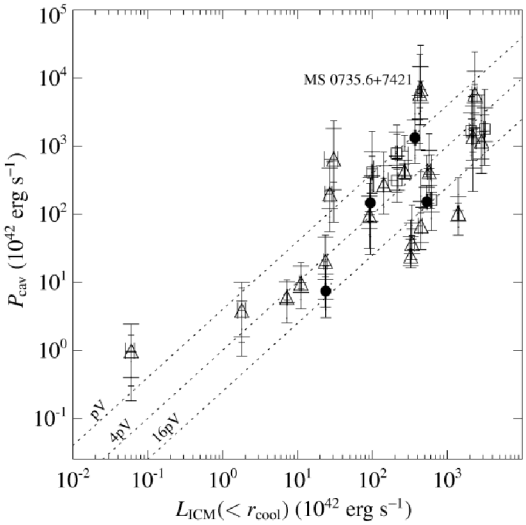

Figure 1.7: AGN heating expressed by the cavity power P_{cav} as a function of the X-ray luminosity in the ICM within the cooling radius for a sample of 33 cluster central dominant galaxies. The radiative losses are balanced by AGN in over half of the systems. Adapted from Rafferty D. A. et al., 2006.

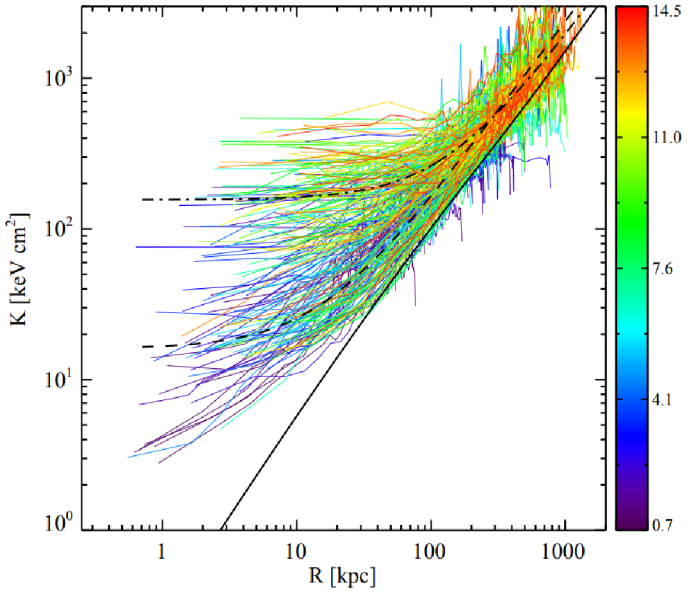

Figure 1.8: Entropy profiles of 239 galaxy clusters. Adapted from Cavagnolo K. W. et al., 2009.

2

SATELLITE SELECTION AND DESCRIPTION

In this Chapter, we will explore the capabilities of *Chandra*, *XRISM*, and *Athena* observatories for detecting multi-temperature gas as well as their structure and technical characteristics.

All mentioned X-ray observatories utilize the Wolter-I type nested mirrors, designed to collect and focus X-ray photons through grazing incidence reflection onto a detector. The detectors employed in these observatories are typically fabricated using semiconductors (*Chandra*) or, more recently, microcalorimeters (*XRISM* and *Athena*). They provide information about the energy and intensity of the detected X-ray photons, allowing us to gain a deeper understanding of the fundamental properties of high-energy objects (more details in Section 2.1.1 and 2.2.1). The mirrors themselves are arranged in nested cylindrical shells, each with a slightly different radius of curvature to achieve the desired grazing incidence angles. The mirror design enables efficient photon collecting and enables the satellites to detect faint and distant X-ray sources (see Figure 2.7). However, each observatory has different mirror sizes, coating materials, and detector technology, resulting in different capabilities and scientific goals.

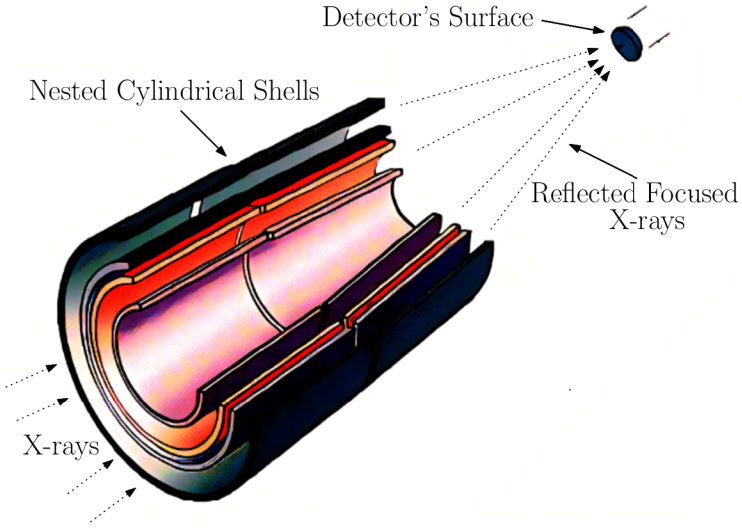

Figure 2.1: Graphical illustration of Walter-I type nested mirror assembly (own illustration).

While all three observatories share some elements, there are essential differences in their designs and instruments that affect their performance.

2.1 CHANDRA X-RAY OBSERVATORY

The *Chandra* X-ray Observatory is a NASA satellite that has played a crucial role in our understanding of the high-energy universe. Its ability to detect X-rays from celestial objects with relatively good resolution and sensitivity has made it, in the past years, an ideal tool for studying the hot gas that fills GCs.

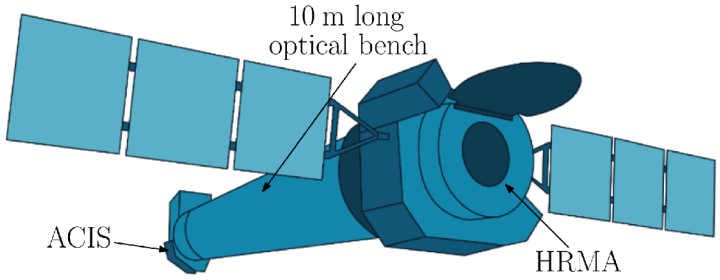

Figure 2.2: Graphical illustration of *Chandra* X-ray observatory. Adapted from NASA, 2022a.

One of the key structure components enabling *Chandra* to focus and detect X-ray photons is the High-Resolution Mirror Assembly (HRMA), which consists of four pairs of nested mirrors that focus the X-rays onto detectors. The mirrors are coated with a thin iridium layer and can focus photons with energies ranging from 0.08 to 10 keV onto the focal plane of *Chandra*'s detectors (Weisskopf M. C. et al., 2000).

2.1.1 *ACIS*

For imaging and spectroscopic studies, *Chandra* is equipped with an X-ray detector known as the Advanced CCD Imaging Spectrometer (ACIS). The detection of X-ray photons using the ACIS instrument is done through a set of ten Charge-Coupled Devices (CCDs).

CCDs comprise a large array of individual pixels, each containing a photosensitive material capable of converting X-ray photons into an electrical charge that can be read out and processed to form an image. More explicitly, when an X-ray photon strikes the photosensitive material, it ionizes atoms within the material, producing free electrons that are then collected by a potential well in each pixel. The number of electrons collected by each pixel is proportional to the intensity of the X-ray radiation that the pixel was exposed to (Li J. et al., 2004). After the electrons are collected, they are read out from each pixel using a series of shift registers that transfer the charge from one pixel to another. This process, known as charge-coupling, allows for the transfer of the charge from the photosensitive material to the readout electronics without the need of physical contacts or wires (Garmire G. P. et al., 2003).

Since the CCD detector can effectively transfer charge, its noise in the signal has an average value of around 2 electrons (Burke B.E. et al., 1997), and the ACIS detector can achieve a moderate spectral resolution of about $150 - 200$ electron volts (eV) at 1 keV (CXC, 2023). The CCDs also impact the spatial resolution, which is limited by their physical size (~ 0.429 arcsec).

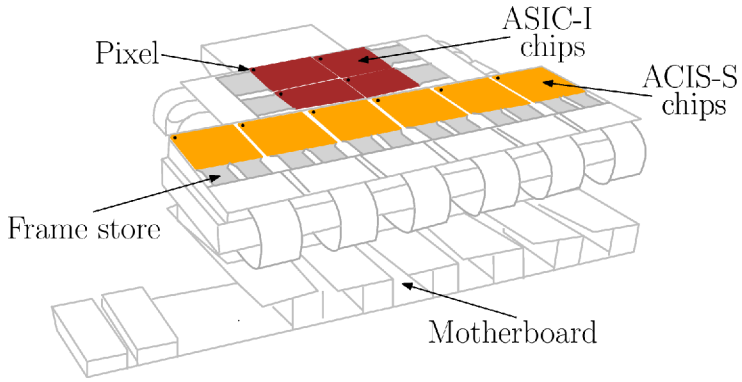

Figure 2.3: Illustration of ACIS focal plane (own illustration).

Chandra's ACIS is composed of two detector arrays: ACIS-S (Spectroscopic) and ACIS-I (see Figure 2.7). ACIS-S contains more sensitive back-illuminated CCDs, and due to its smaller field of view (8.3x8.3 arcmin) but better energy resolution, it is optimized for spectroscopic observations. On the other hand, ACIS-I has only front-illuminated chips and with a combination of its more extensive field of view (16.9x16.9 arcmin) it is optimized for imaging observations (Chartas G. et al., 1998).

2.2 X-RAY IMAGING AND SPECTROSCOPY MISSION (XRISM)

The X-Ray Imaging and Spectroscopy Mission (*XRISM*) is one of the latest addition to the fleet of X-ray observatories designed to study the high-energy universe under JAXA-NASA collaboration and is planned to launch in spring 2023. As a successor to the Hitomi satellite, which suffered an unfortunate malfunction shortly after launch, *XRISM* aims to continue the study of high-energy astrophysical phenomena (Ishisaki Y. et al., 2018).

Similarly to the *Chandra* X-ray Observatory, *XRISM*s mirrors are arranged in a Wolter Type-I configuration called X-ray Mirror Assembly (XMA). The XMA consists of 203 nested shells coated with a thin layer of gold, with a maximal diameter of 45 cm (JAXA, 2018). The angular resolution attained by *XRISM* is 17 arcseconds, which is substantially worse than the 0.5 arcsecond resolution achieved by *Chandra*. The mission is equipped with a soft X-ray spectrometer *Resolve* (see 2.2.1) and a soft X-ray imager *Xtend*. Each instrument has its own XMA with a focal length of 5.6 m (Tashiro M. et al., 2020).

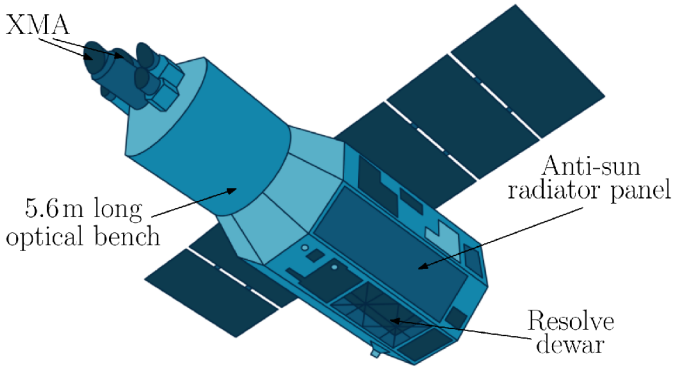

Figure 2.4: Graphical illustration X-Ray Imaging and Spectroscopy Mission. Adapted from NASA, 2022b.

2.2.1 *Resolve*

The Reflection Grating Spectrometer (*Resolve*) is one of the two primary detectors onboard *XRISM*. The instrument consists of an array of 6x6 microcalorimeters, each with 4x4 cm in size (XRISM Science Team, 2020). One microcalorimeter comprises more than 128 transition edge sensor (TES) pixels made of a superconducting thin film, which are connected to a readout circuitry. The TES pixels are designed to detect X-ray photons by converting their energy into heat, which is then measured by a highly sensitive thermometer (see Figure 2.5).

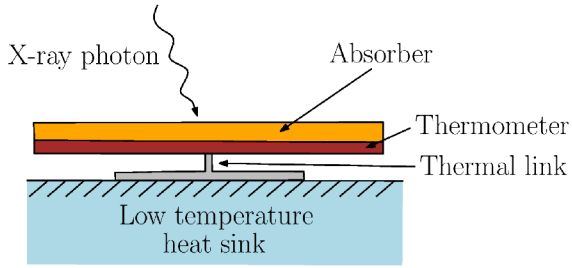

Figure 2.5: Illustration of TES microcalorimeters working principles (own illustration).

More specifically, the temperature rise, caused by incoming photons, causes a change in resistance on TES, which is monitored by a quantum interference device (SQUID). To ensure that the TES pixels remain in their superconducting state, and thus maintain their eV level energy resolution, the detector is cooled to a temperature close to an absolute zero (around 50 mK) inside a dewar with a complex cooling system (Ezoe Y. et al., 2020). The cooling system can use two methods to achieve the final operational temperature, the liquid helium and additional Joule-Thomson coolers. To prevent the mission failure due to the loss of liquid helium, the cooling system was designed with an secondary unit of adiabatic demagnetization refrigerator that could

use a Joule-Thomson cooler as a heat sink to maintain cooling even after the liquid helium is depleted (Sato K. et al., 2023).

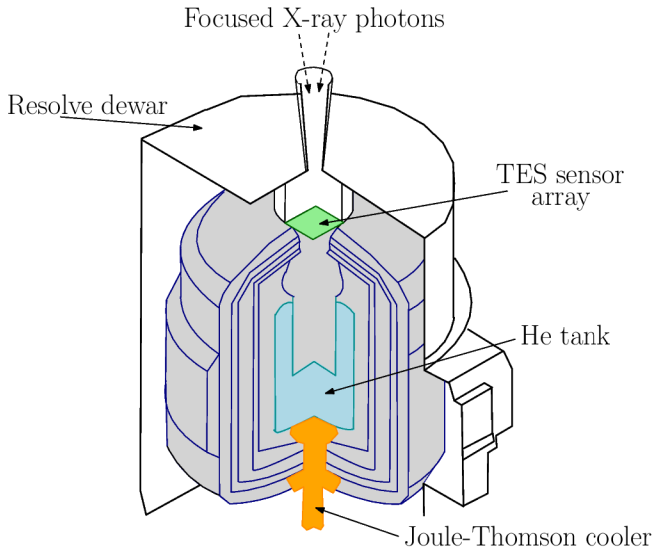

Figure 2.6: Cooling chamber for *XRISM* mission (own illustration).

This architecture will allow *XRISM* to surpass *Chandra* satellite in both sensitivity and resolution (see Table 1) and enable us to address fundamental questions in astrophysics.

2.3 ADVANCED TELESCOPE FOR HIGH-ENERGY ASTROPHYSICS (ATHENA)

The *Athena* X-ray Observatory is a next-generation space observatory developed by the European Space Agency (ESA) designed to study the hot and energetic universe with unprecedented sensitivity and spectral resolution. Similar to *Chandra* and *XRISM* missions, the *Athena* is equipped with a segmented Wolter-I configuration mirror assembly with an effective area of nearly 2 m^2.

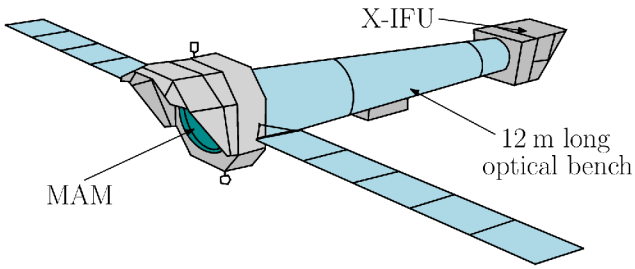

Figure 2.7: Graphical illustration of *Athena* Mission (own illustration).

Scheduled for launch in the early 2030s, *Athena* will be the largest X-ray observatory ever built, with a collecting area five times larger than its predecessor, the *Chandra* X-ray Observatory.

At the heart of *Athena*'s science capabilities is the X-ray Integral Field Unit (X-IFU), an advanced cryogenic imaging spectrometer that offers high-resolution spectroscopy over a wide range of energies, from 0.2 to 12 keV (see Section 2.3.1). The second important instrument that the mission carries onboard is the Wide Field Imager (WFI), which provides a view of the sky with an angular resolution of 5 arcseconds (Nandra K. et al., 2013).

2.3.1 *X-IFU*

The X-ray Integral Field Unit (X-IFU) is an X-ray spectrometer that will be placed on board the *Athena* observatory. Like *Resolve* detector, the X-IFU is based on a Transition Edge Sensor (TES) technology, which involves using a superconducting material to detect small temperature changes caused by incoming X-rays (see Section 2.2.1). However, the X-IFU detector has a much larger array of TES pixels (2376 pixels), allowing for much higher spatial resolution. The detector is stored in a cooling chamber (see Figure 2.6), which keeps it at a temperature of 55 mK (Castellani F. et al., 2022). Moreover, the X-IFU is designed to have a wider energy range, covering X-rays from 0.2 keV to 12 keV.

One of the main advantages of the X-IFU is its high energy resolution, which is currently estimated to be 2.5 eV at 7 keV (Gottardi L. and Smith S., 2022). Its high resolution with a wide field of view allows for simultaneous observation of multiple sources and better identification of X-ray emission lines. These capabilities make X-IFU a powerful tool, that could be used for detailed studies of the physical processes taking place in the hot universe, including the dynamics of galaxy clusters, the feedback of supermassive black holes, and the formation and evolution of galaxies.

Specification	Chandra	XRISM	Athena
Energy range [keV]	$0.2 - 10$	$0.3 - 12$	$0.2 - 12$
Energy resolution @1keV [eV]	140	5	2.5
Angular resolution [arcsec]	0.5	17	5
Field of view [arcmin]	60	3	40
Effective area @1keV [cm^2]	120	160	2000
Focal length [m]	10	5.6	12

Table 1: Selected specifications for satellites introduced in the Chapter 2. Adapted from CXC, 2023; Gottardi L. and Smith S., 2022; Ishisaki Y. et al., 2022; NASA, 2022b; Sato K. et al., 2023

3

DATA ANALYSIS

3.1 MACHINE LEARNING APPROACH

The power of machine learning (ML) in spectral analysis has been proven in multiple studies (Belabbas M. A. and Wolfe P. J., 2021; Kerby S. et al., 2021; Ntampaka M. et al., 2019; VanderPlas J. et al., 2012). However, the most relevant study to this work was presented by Carter Rhea, who investigated hot intracluster medium surrounding the center of galaxy clusters using *Principal component analysis* (see Section 3.1.1), commonly used in the spectral analysis for dimensionality reduction of the data, and then the *Random forest classifier* (see Section 3.1.2) used for categorizing the number of underlying components (Rhea C. et al., 2020). Since the results of his study demonstrated a very reliable and efficient estimate of multi-temperature plasma in GC, we will apply a similar ML technique to our data as well.

3.1.1 *Principal Component Analysis*

Principal Component Analysis (PCA) is a standard data reduction tool in modern data analysis that extracts relevant information from complex, confusing datasets. The technique unfolds complicated relations between variables into their primary components. In other words, the PCA reduces the number of dimensions and reveals obscured simplified structures that often underlie the data (Bro R. and Smilde A. K., 2014). In more detail, PCA rotates the original data to a new, orthonormal basis in which the projection of data, with maximized variance, is included in the first principal component (the first coordinate), the data, with the second most significant variance, is included in the second principal component, and so on (see figure 3.1). This method is closely related to the multivariate statistical technique Singular Value Decomposition (SVD), which calculates values of eigenvectors (Shlens J., 2014).

Mathematically, PCA transforms the correlated data from its original basis of variables to a base where the data isn't correlated. Following the work of Murtagh F. and Heck A., 1987, we outline this tool. Let us consider a spectrum represented as an M-dimensional vector, X, and a dataset composed of N of these individual spectra. The first principal component X_0 represents the direction of maximum variance in M-dimensional vector space, S, generated by the spectra. In general notation, the i-th component, from the total of M principal components in the perpendicular subspace,

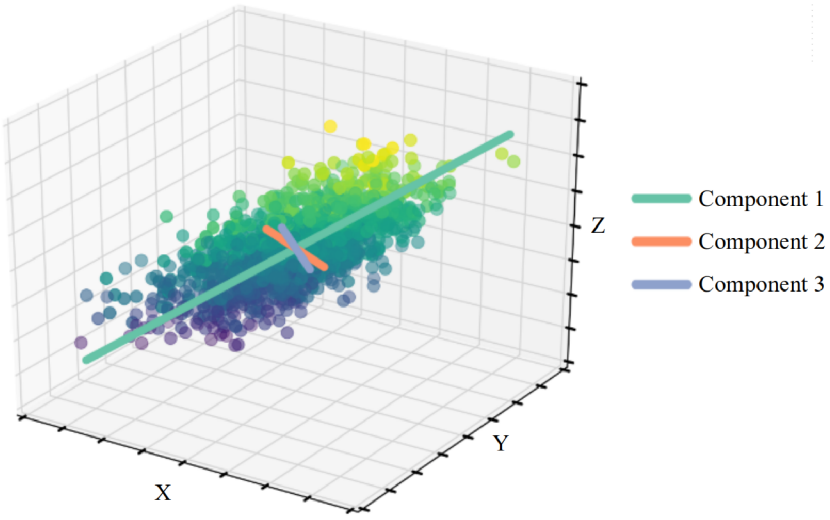

Figure 3.1: Graphical illustration of PCA in 3D vector space. Adapted from Barnett R. M., 2017.

is in the direction of the i-th highest variance. The corresponding equations describing the spectra are, therefore:

$$\langle r_i \rangle = \frac{1}{N} \sum_{i=1}^{N} r_{ij}, \tag{3.1}$$

$$X_{ij} = r_{ij} - \langle r_i \rangle, \tag{3.2}$$

where r_{ij} are the initial spectra measurements, including the spectrum's number represented by i and the wavelength bin represented by j. The covariance matrix will be then constructed as:

$$C_{jk} = \frac{1}{N} \sum_{i=1}^{N} X_{ij} X_{jk}, \tag{3.3}$$

where $M \geq i, j \geq 1$. The first principal component is then defined as:

$$\vec{C}\vec{e_1} = \lambda_1 \vec{e_1}, \tag{3.4}$$

where $\vec{e_1}$ is the first eigenvector and λ_1 is the first eigenvalue. Since our work focuses on emission spectra from ICM, the equations above can be rewritten and described in terms of spectra:

$$\vec{x_i} = \vec{\mu} + \sum_{j=1}^{N} a_{ij} \vec{v}_j, \tag{3.5}$$

where $\vec{x_i}$ corresponds to a given spectrum, $\vec{\mu}$ represents the mean spectrum evaluated from the whole dataset, and $a_{ij}\vec{v}_j$ are the decomposed eigenspectra (Yip C. W. et al., 2004).

3.1.2 *Random Forest classifier*

The Random Forest (RF) classifier, introduced by Leo Breiman in 2001, is an ensemble algorithm that builds upon a fundamental set of uncorrelated decision trees (Breiman L., 2001). The method extends the concept of decision trees by generating an ensemble of decision trees working together to make predictions (see Figure 3.2). The RF employs a seemingly counter-intuitive strategy that ensures the divergence of individual trees within the forest. It achieves this through two distinct steps (Yi Z. and Pan J., 2010).

In the first step, each decision tree is constructed using different bootstrap samples of the original dataset. By generating these bootstrapped samples, RF introduces diversity into the ensemble, enabling each tree to capture unique patterns and information from the data. In the second step, at each node of every tree, the algorithm randomly selects a subset of predictors from the available features. This subset of predictors is again randomly chosen for each tree, and the split is determined based on the best fit of selected variables (see Figure 3.2). This random selection of predictors further enhances the diversity of the trees within the forest, supporting its robustness and reducing the risk of overfitting (Hastie T. et al., 2009).

The process via which the RF model learns its parameters is known as *training*. During training, each tree in the ensemble independently learns from the data, and their decisions are then integrated to form the final prediction. By combining the predictions of multiple trees, the RF classifier can effectively handle complex patterns and capture the underlying relationships within the data (Belgiu M. and Drăguţ L., 2016).

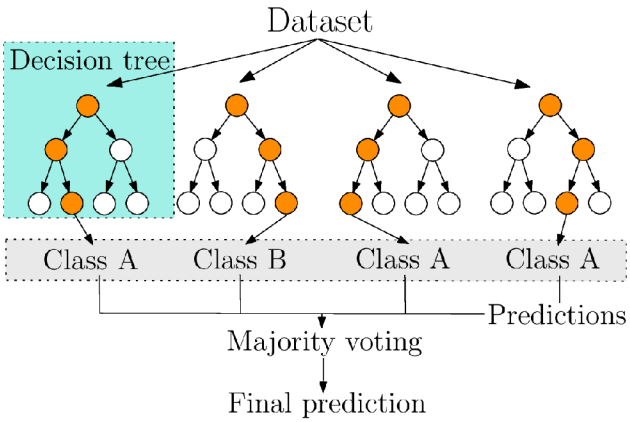

Figure 3.2: Simplified working principle of RF classifier (own illustration).

RFs are one of the most popular machine learning techniques available due to their advantages, such as speed, simplicity of implementation, and robustness to overfitting. On the other hand, the mechanism is extremely complex and comprises several driving

forces, making the result all the more difficult to interpret (Biau G., 2012; Liaw A. and Wiener M., 2001).

Despite its limitations, the RF classifier with the combination of PCA has shown to be a valuable tool for classification problems, displaying outstanding accuracy and robustness in various scientific domains. By harnessing the collective decision-making power of multiple trees and leveraging the insights from PCA, the RF classifier with PCA offers a comprehensive approach to solving complex classification tasks.

3.2 XSPEC MODELS

The XSPEC software package is widely used in X-ray astronomy for modelling and fitting the spectra of astrophysical sources and was developed by Keith Arnaud at NASA Goddard Space Flight Center (Arnaud K. A., 1996). The platform offers an extensive library of spectral models that can mathematically describe X-ray emissions from different physical processes. These models can be combined to build and investigate the physical properties of any required sources in detail (Arnaud K. A., 1996-2021).

To study multi-temperature gas in GCs, the most relevant models for synthetic spectra are PHABS, which represents the absorption of X-rays by neutral hydrogen, and APEC, which represents the thermal emission from diffuse hot gas. The physics behind these XSPEC models will be discussed in the following section.

3.2.1 *PHABS model*

The PHABS model in XSPEC is a photoelectric absorption model that calculates the absorption of X-ray photons by interstellar gas or dust (Wilms J. et al., 2000). The model is based on the cross-sections for photoelectric absorption, calculated from the atomic cross-sections and energy levels of the absorbing atoms and ions. It assumes that the absorbing material is fully ionized and can be described by only one parameter: the hydrogen column density, which describes the total number of hydrogen atoms along the line of sight to the X-ray source and is a measure of the amount of material capable of absorbing X-ray photons. The equation expressing this model is:

$$M(E) = exp[-N_H \sigma(E)], \tag{3.6}$$

where N_H is the hydrogen column density in units of 10^{22} cm^{-2} and $\sigma(E)$ is the absorption cross-section of neutral hydrogen as a function of photon energy (Balucinska-Church M. and McCammon D., 1992).

3.2.2 *APEC model*

The APEC (Astrophysical Plasma Emission Code) model in XSPEC is based on the assumption that the X-ray emitting diffuse gas is in ionization equilibrium (Brickhouse N. S. and Smith R. K., 2005). The model calculates the X-ray spectrum emitted by the plasma as a function of temperature and elemental abundances from the *AtomDB* atomic database (Foster A. and Smith R. K., 2017).

The model is characterized by several parameters: temperature $k_{\rm B}T$, abundance Z cosmological redshift z, and normalization N, which is given as

$$N = \frac{10^{-14}}{4\pi[D_{\rm A}(1+z)]^2} \int n_{\rm e} n_{\rm H} dV, \tag{3.7}$$

where $D_{\rm A}$ is the angular diameter distance to the source in cm, $n_{\rm e}$ and $n_{\rm H}$ are the electron and hydrogen densities in cm^{-3}, and V is the volume of the emitting region in cm^3. The model assumes that the plasma is optically thin so that all the radiation escapes from the emitting region (Heuer K. et al., 2021). The X-ray emissivity $\Lambda_i(E,T)$ of an ion i is calculated as

$$\Lambda_i(E,T) = \frac{n_i}{n_H} h\nu_i A_{i,jk}(E,T), \tag{3.8}$$

$$A_{i,jk}(E,T) = (2.30 \times 10^{-6}) \frac{g_j}{g_k} C_{jk} \left(\frac{h\nu_{jk}}{E_i} \right), \tag{3.9}$$

where n_i is the number density of the ion i, $h\nu_i$ is the energy of the emitted photon, $A_i(E,T)$ is the Einstein's A coefficient for the transition between levels j and k of ion i, where g_j and g_k are the statistical weights, C_{jk} is transition probability coefficient and E_i is the ion's ionization energy. The number density of the ion i is given by the Saha equation

$$\frac{n_{i+1}}{n_i} = \frac{n_{\rm e}}{n_{\rm H}} \left(\frac{2\pi m_{\rm e} k_{\rm B} T}{h^2} \right)^{3/2} \exp\left(-\frac{E_i}{k_{\rm B}T} \right), \tag{3.10}$$

where $m_{\rm e}$ is the electron mass, $k_{\rm B}$ is the Boltzmann constant, T is the temperature, h is the Planck constant, and E_i is the ionization potential of the ion i (Peacock J. A., 1999). The total X-ray emissivity of the ion i is then calculated by summing over all possible transitions, whereas the population of level j to the level k is given by the Boltzmann distribution

$$f_{jk}(E,T) = \frac{g_j}{g_k} \exp\left(\frac{E_{jk}}{k_{\rm B}T} \right), \tag{3.11}$$

where E_{jk} is the energy difference between levels j and k. The AtomDB database provides the necessary atomic data for the APEC model calculations, including energy levels, transition probabilities, and collisional excitation and ionization rates (Brickhouse N. S. et al., 2000).

4

METHODOLOGY & RESULTS

In this chapter, we will introduce the procedures, processing, and results of our study that focuses on a machine learning approach to analyze multi-temperature regions in the ICM and the capabilities of the selected missions (*Athena*, *XRISM*, *Chandra*) to recognize different temperature components in the X-ray spectrum. Our focus will be directed towards the hot gas in the Virgo and Perseus clusters, which are among the first proposed targets for the *Athena* observatory.

4.1 DATA SIMULATION

Since the number of underlying temperature components in these clusters is unknown, and *Chandra* does not provide sufficient resolution of real observations to identify them accurately, with the fact that *Athena* and *XRISM* have not yet been launched, we simulated sets of synthetic spectra for each cluster with desired parameters and trained our models on these datasets. This approach enables us to explore the observatories' sensitivity in the soft X-ray bands in a more controlled and precise manner.

4.1.1 *Synthetic spectra*

The synthetic spectra were constructed using CIAO's modelling and fitting package *Sherpa* (CXC, 2022b) with `fake_pha` tool. To produce mock spectra, the tool takes a response matrix file (RMF) and an ancillary response file (ARF) representing the detectors' properties on board studied missions. These files are consistently updated as the detectors' performances are steadily degrading (case of *Chandra*) or are still in development (case of *XRISM* and *Athena*).

For consistency between all three satellites, we selected response files that were calibrated on-axes of the telescopes, and to maximize the spectroscopic capabilities for *Chandra*, we selected response files for the ACIS-S detector, while for *XRISM* and *Athena*, we employed the response files for the Resolve and X-IFU detectors, acquired from CXC, 2022a; JAXA, 2022; X-IFU, 2020 (see Figure 4.1). When simulating the spectra, we used the whole range of energies that are covered by individual files. However, in order to ensure consistency among the satellites, we established a maximum energy range of 4 keV for all observatories during the training process. Additionally, for the Chandra satellite, we introduced a minimum limit of 0.5 keV (see Section 4.2.2).

For each model (described in section 4.2), we generated 10,000 single-temperature component spectra for the Virgo Cluster in the energy range of $1 - 4$ keV and for the Perseus Cluster in the range of $2 - 5$ keV. In addition, we generated 10,000 two-temperature component spectra for each model, with the first thermal component covering the same energy range as the single-temperature spectra, while the second thermal component for the Virgo Cluster ranged from $0.5 - 0.75$ keV and for the Perseus Cluster ranged from $0.6 - 0.85$ keV. Each temperature was randomly sampled from a uniform distribution (see Figure 4.2).

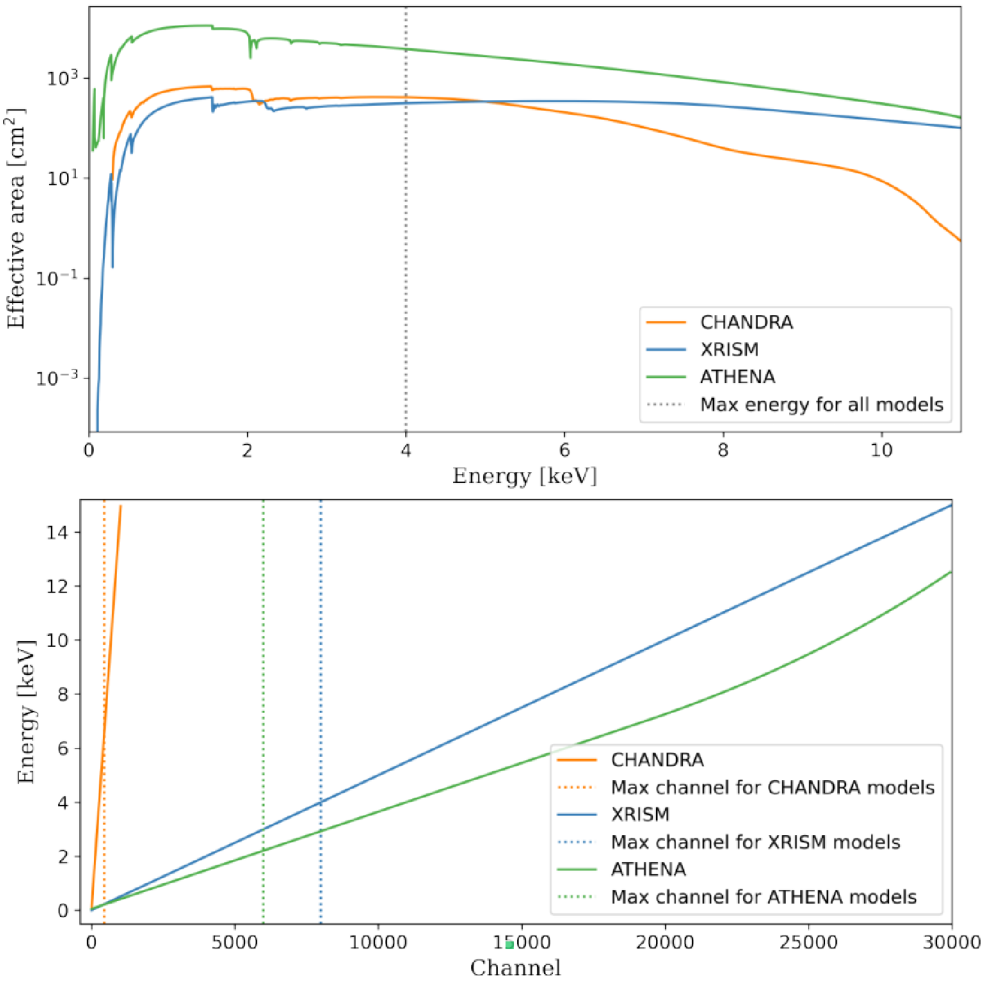

Figure 4.1: Selected on-axis ARF (upper) and RMF files (lower) for observatories in this study.

The parameter values of the primary thermal component were selected by drawing upon the findings of multiple studies investigating the temperature characteristics of the clusters (such as Ichinohe Y. et al., 2019; Young A. J. et al., 2002), while the temperature range for the second component was derived from more detailed examinations

of intriguing filaments within these cluster cores (Sanders J. S. and Fabian A. C., 2007; Simionescu A. et al., 2017). It is important to note that these values do not cover the complete spectrum of temperatures observed in the clusters in the past years. However, to investigate the characteristics of satellites to their utmost limits, these parameters were deliberately selected.

Normalization

Selecting an optimal normalization range for our clusters is crucial as it greatly influences the count statistics within the resulting spectrum and impacts its signal-to-noise ratio (SNR). In this regard, the primary component's normalization N for the two chosen clusters was derived using Equation 3.7. The respective density profiles were adopted from Fabian A. C. et al., 1981; Kartun-Giles A. et al., 2018; Plšek T. et al., 2022; Taylor G. B. et al., 2006. In the calculations we assume the redshift and hydrogen column density of Virgo cluster $z_V = 0.004$, $n_{H_V} = 0.2 \times 10^{21}$ cm^{-2}, the redshift and hydrogen column density of Perseus cluster $z_P = 0.02$, $n_{H_P} = 1.4 \times 10^{21}$ cm^{-2} and the standard ΛCDM model with parameters $H_0 = 70$ km s^{-1} Mpc^{-1}, $\Omega_m = 0.3$, $\Omega_\Lambda = 0.7$.

The derived normalization values for both of the clusters vary between 10^{-3} and 10^{-5}. Consequently, the normalization of the primary temperature component was adjusted accordingly, while the secondary component normalizations were selectively set for each model. This strategic approach enabled us to carefully and effectively explore the satellite's ability to discriminate the multi-temperature regions. In order to minimize the likelihood of generating primary data that could be too easily identified by the satellites (higher normalization = less noise and more recognizable features), each normalization was randomly sampled from a loguniform distribution. (see Figure 4.2).

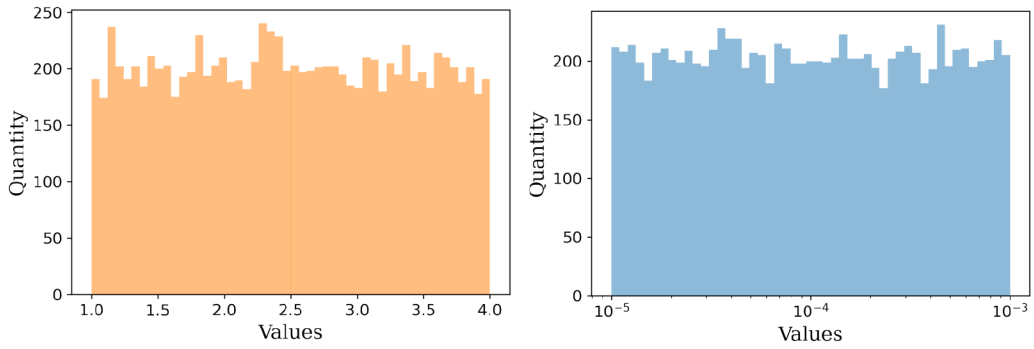

Figure 4.2: Example of 500 temperatures (on the left) and normalizations (on the right), generated from a uniform and logarithmic distribution for single-temperature spectrum in Virgo cluster.

The selection of a suitable normalization for a given spectrum is closely linked to the number of counts it comprises (see Table 2). To generate realistic observation, we

established minimum and maximum count thresholds for the spectra. In doing so, we can adjust the normalization factor to reflect the count values, which can be feasibly observed by *Chandra* X-ray observatory. To better understand the extent to which satellites are able to distinguish multi-temperature components with varying normalization ratios, we must also consider the effects of exposure time on the count rate. However, while normalization is inherently tied to the structure of celestial objects, exposure time can be adjusted as needed. We maintained a constant exposure time of 100 ks in all models to secure a realistic number of counts in spectra and to guarantee any variations in count rate were primarily dependent on the normalization parameter.

To ensure an unbiased performance comparison between all missions, we adopted the same parameters also for *XRISM* and *Athena*. Both satellites offer a significantly higher spectral resolution compared to Chandra, which means that a higher signal-to-noise ratio (SNR) is required to resolve the spectral lines properly. However, XRISM has only a slightly larger effective area than Chandra, which can limit the collection of counts and ultimately affect the SNR. With our specifications, primary normalization set to 10^{-4} and exposure time 100 ks, Athena is capable of collecting around 500 counts per channel, while XRISM can collect approximately 2 counts per channel and Chandra 22 counts per channel. The specific count values corresponding to the minimum and maximum thresholds and their corresponding SNR are presented in Table 2. The SNR was calculated from Poisson statistics as follows:

$$\mathrm{SNR} = \frac{N}{\sqrt{N}} = \sqrt{N}, \tag{4.1}$$

where N is the number of photons in one spectrum.

	Chandra		*XRISM*		*Athena*	
norm	SNR	Counts	SNR	Counts	SNR	Counts
10^{-5}	22	500	33	1100	205	42000
10^{-4}	74	5500	114	13000	742	550000
10^{-3}	265	70000	575	33000	3606	13000000

Table 2: Comparison of signal-to-noise ratio and Counts for specified normalizations for *Chandra*, *XRISM*, and *Athena* satellites.

By employing the parameters described above into SHERPA's `fake_pha` tool, we constructed spectra with single and two thermal components via the application of an absorbed thermal emission model sourced in XSPEC as:

PHABS×(APEC)
PHABS×(APEC1+APEC2)

where the APEC (used version 3.0.9) models the thermal emission (see Section 3.2.2) and PHABS represents the galactic absorption (see Section 3.2.1). Initially, we limited our analysis to only two thermal components, with the primary aim of exploring the extent to which the satellites are capable of distinguishing the cooler component based on the normalization ratios between the first and second components. However, we also conducted a brief analysis of a three thermal component plasma for the Virgo cluster.

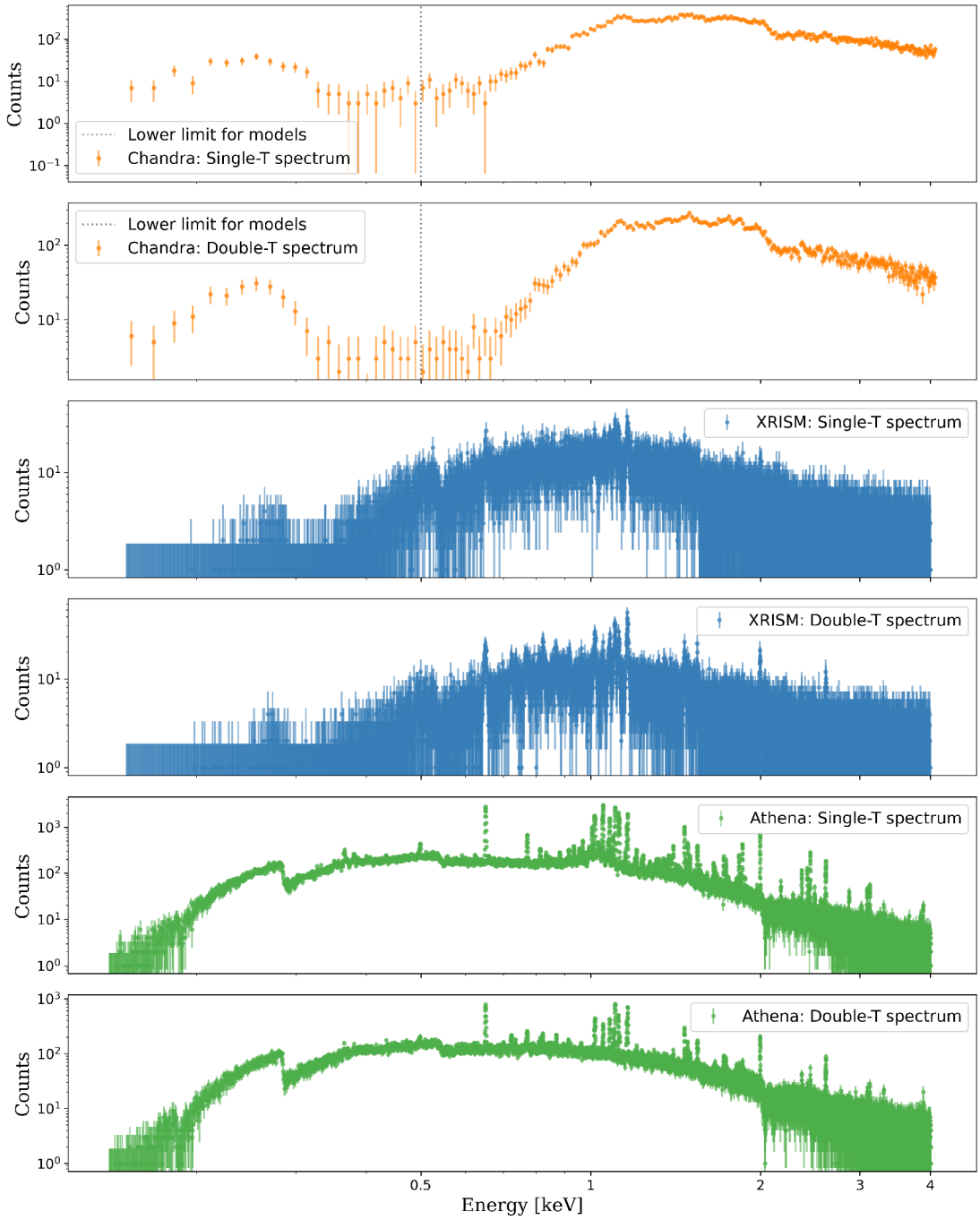

Figure 4.3: Comparison of selected single-temperature and double-temperature spectra, generated for *Chandra*, *XRISM*, and *Athena* observatories.

4.2 RF MODELS

In this section, we will explore the RF models that were trained for the selected satellites to identify multiphase regions in Virgo and Perseus clusters. These models were developed in order to significantly speed up the process of the traditional multi-temperature analysis and to test the capabilities of the future X-ray missions *XRISM* and *Athena* in comparison to the present *Chandra* X-ray observatory.

We will discuss the training process, the architecture of the models, and their performance on simulated and real data. We will also examine the limitations of our ML analysis compared to the XSPEC platform and the potential for future developments in this exciting field.

4.2.1 *Selected spectrum of training data*

As described in the previous chapter, we have generated thousands of spectra with various parameters, which will serve as input for the RF models. The aim is to explore the ability of the *Chandra*, *XRISM*, and *Athena* observatories to distinguish the presence of the cooler component, depending on the normalization ratio between the two temperature components presented in the spectra. To achieve this objective, we have divided the simulated spectra into five distinct categories for each satellite individually.

$N_1^{\max}$	$N_1^{\min}$	$N_2^{\max}$	$N_2^{\min}$	$R^{\min}$
10^{-3}	10^{-5} (10^{-4})	10^{-5} (10^{-4})	$10^{-6}(10^{-5})$	0.1
			$5 \cdot 10^{-7}(5 \cdot 10^{-6})$	0.05
			$10^{-7}(10^{-6})$	0.01
			$5 \cdot 10^{-8}(5 \cdot 10^{-7})$	0.005
			$10^{-8}(10^{-7})$	0.001

Table 3: Selected normalization parameters for double-temperature models. $N_1^{\min}$, $N_1^{\max}$ represents the minimum and maximum of the normalization range for the main thermal component, $N_2^{\max}$, $N_2^{\min}$ represents minimum and maximum of the normalization range for the second cooler thermal component and the $R^{\min}$ parameter is the ratio between the minimum normalization values of the second and first components. The numbers in brackets were selected for the second set of models for *Chandra* satellite.

For the main temperature component, we set the normalizations the same for all the groups ($10^{-3} - 10^{-5}$) since this parameter should represent the realistic properties of the clusters. However, we made an exception for the *Chandra* satellite and trained the models on a more limited range as well ($10^{-3} - 10^{-4}$) due to the poor accuracy of the models on spectra with such low count rates. For the second cooler component,

these 5 categories are differentiated based on the ratio of the minimum values for normalization ranges (see Table 3)

As can be deducted from Table 3, these categories differ in the normalization ratios of the minimum values between the cooler thermal component and the first main component. Since the normalizations were simulated with a loguniform distribution, this approach can provide insights into the extent to which the satellites can distinguish the second component. In doing so, it tests the limits of the satellites' ability to recognize multi-temperature regions with a significant acceleration of the traditional process. Furthermore, it will enable us to assess the effectiveness of future X-ray missions such as the *XRISM* and *Athena* in comparison with the current *Chandra* X-ray Observatory.

4.2.2 *Training & Testing*

A total number of 100000 spectra corresponding to one cluster were generated for each satellite (twice as much for *Chandra* for the second normalization ranges). To train and test the performance of our models, we used the cross-validation method, which is commonly used in ML analysis, to estimate the accuracy for various splits into training and testing data, allowing us to estimate an average accuracy together with uncertainties. We divided our dataset of 20000 spectra (for each model) into five groups and individually trained the model on four of these groups. We then tested all of the trained models on the fifth set, which had not been seen by our models till then. The final mean accuracy and uncertainty were determined by simply following the standard average calculation steps.

In the training process, we adapted the PCA algorithm for principal component analysis and the standard RF classifier from RandomForestClassifier for classification (see Section 3.1.1 and 3.1.2), both from the Scikit-learn library. Firstly, we applied the classifier to each spectrum individually. Next, we summed the probabilities over the entire ensemble using the definition of the classifier. The final classification is based on the class with the highest summed probability.

Due to the difference in the energy range of the simulated spectra from the various missions, we need to adjust them for the sake of uniformity. To this end, we adopted a maximum limiting value of 4 keV, guided by two factors. Firstly, the high spectral resolution of *XRISM* and *Athena* satellites makes loading all available channels computationally demanding and very time-consuming (see Figure 4.1). Secondly, the principal components derived from PCA exhibited the most variability in the soft X-ray regime from $0.5 - 2$ keV, which is an expected trend since we primarily model diffuse hot gas emitting mostly in these bands. The 'tail' of the spectrum has almost no bearing on the accuracy of the models and is negligible (refer to Figure 4.4).

To further optimize our bounded resources and computing power, as an input for our models, we used a maximal energy limit of 4 keV for both *XRISM* and *Athena* satellites, while for *Chandra* X-ray observatory, the input for models was limited in the range of $0.5 - 4$ keV. The lower limit for *Chandra* is based on the future application of the models on real data, which below 0.5 keV have relatively low sensitivity and lower SNR. Moreover, the systematic calibrations of response files are challenging in these conditions, making it difficult to obtain accurate measurements. With these criteria, the final number of channels that went into the model were for *Chandra* 245, for *XRISM* 8000, and for *Athena* 11000 (see Figure 4.1).

In Figure 4.4, we visualized the first 5 eigenspectra and mean spectra of the *Chandra* training set (16000 synthetic spectra) without the limitations set above. The individual components in the graph represent the eigenspectra projected onto the original domain ($\vec{v}_j$ in Equation 3.5), and the mean emission spectra is their sum.

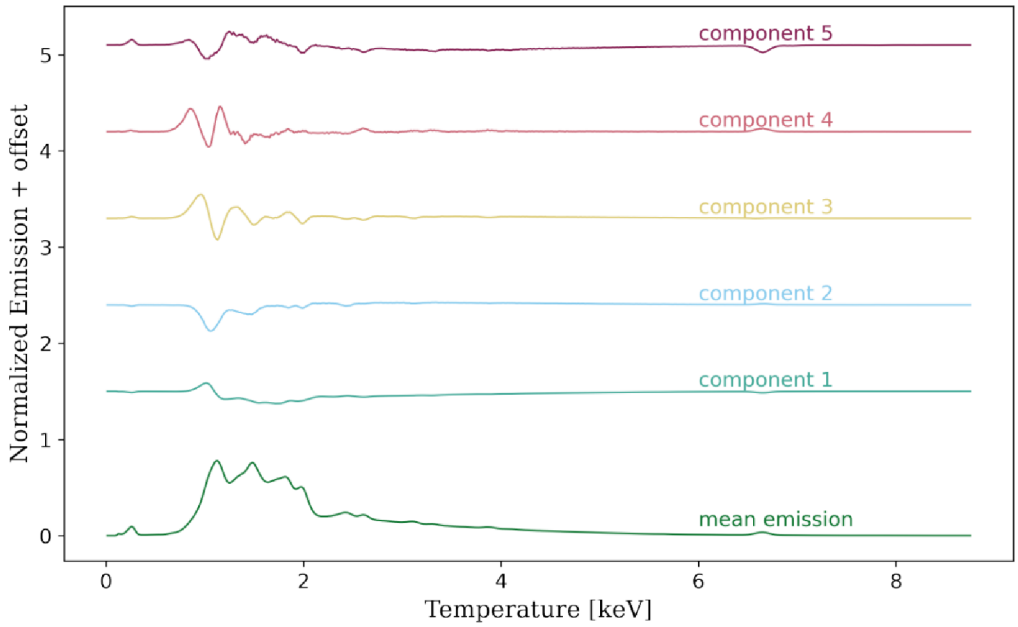

Figure 4.4: Visualisation of the first 5 principal components and their linear combination (mean emission) for the channel range extended beyond the limitations for our models of *Chandra* satellite for configuration $N_1^{\min} = 10^{-5}$ and $R^{\min} = 0.1$.

In order to determine the number of principal components that would be the best to include, we looked at how the number of components affects the accuracy of models. The final number of components was chosen based on the highest parameter variance coverage while still maintaining great accuracy (see Figure 4.5). As the number of principal components increases beyond a certain point, the model's accuracy begins to drop, as can be seen in Figure 4.5. The beauty of principal components lies in their ability to filter out the noise in the data and capture the essential features in the

spectra. Therefore, when the number of components becomes too large, in our case, 30 and more, the components included after tend to contribute significant noise, leading to confusion in the algorithm. After this analysis, we concluded that 25 principal components would be used as the input for our RF classifier.

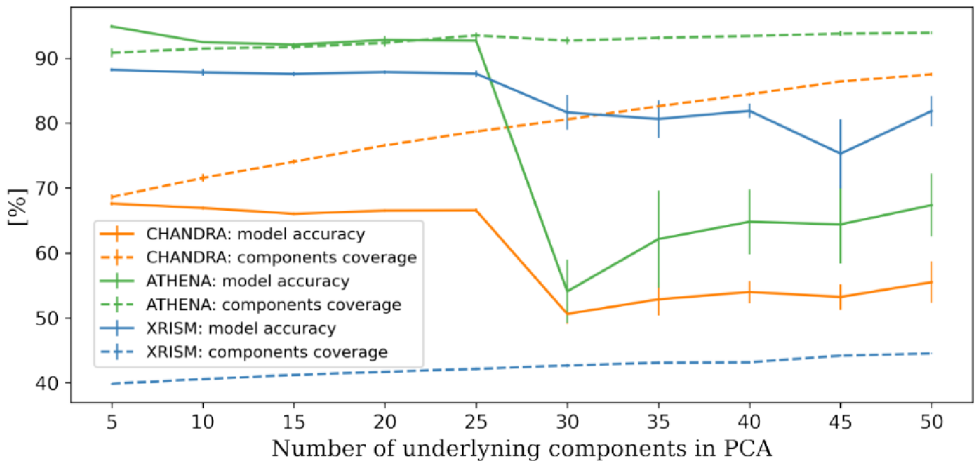

Figure 4.5: Investigation of the dependence between a number of components and the model's prediction accuracy, as well as parameter coverage for model configuration $N_1^{\min} = 10^{-5}$ and $R^{\min} = 0.1$.

Through a careful process of exploring diverse architectures and experimenting with various hyper-parameters, we selected the most optimal configuration for the machine learning model dependent on the parameter coverage, an appropriate number of principal components, and prediction accuracy. The success of the model's predictions was evaluated using confusion matrices. In the employed cross-validation technique, we combined results from 4 confusion matrices to capture the deviation of the model's predictions (one matrix from each model is shown in Appendix A).

The complete training procedure for both *Chandra* normalization limits, including the loading of synthetic spectra, the application of PCA, and the actual training stage, required 0.4 hours for a single cluster. While for *XRISM* and *Athena*, the computing time was 24.2 hours and 17.4 hours for a single cluster, respectively. However, The most time-consuming part was the loading of synthetic spectra, which took about 95% of the entire process.

In summary, we first simulate X-ray spectra for both single and double-temperature plasma. With the implementation of PCA, we reduce the number of free parameters by creating projection matrices for each training spectrum. Subsequently, we train our RF algorithm to classify the input spectra based on the underlying number of components. Finally, we validate the success of the trained algorithm on a test set (see Figure 4.6) that had been fine-tuned using the same approach as the training dataset.

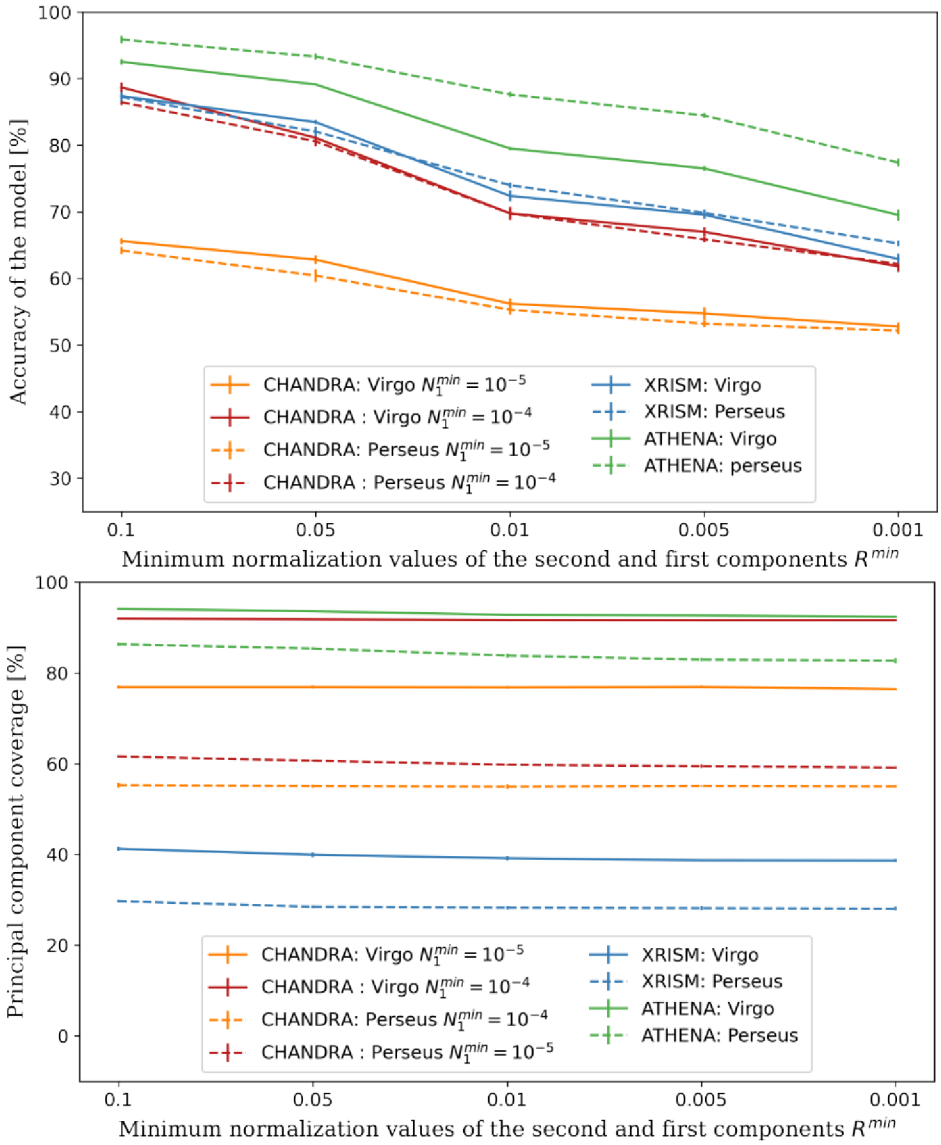

Figure 4.6: Graphical illustration of prediction accuracy (upper graph) and parameter coverage (lower graph) for all models plotted as a function of the normalization ratio between second and first thermal components.

From the results visualized in Figure 4.6, it is evident that the performance of *Athena* surpasses that of *Chandra* and *XRISM* satellites for both galaxy clusters. The *Chandra* satellite's ability to distinguish between single-temperature and double-temperature spectra remains the poorest for both of the investigated normalization ranges. Although the principal component coverage varies between the clusters for all models, it is not reflected in the model's accuracy.

Mission	$R^{\min}$	$M^V_{\rm acc}$[%]	$C^V_{\rm var}$[%]	$M^P_{\rm acc}$[%]	$C^P_{\rm var}$[%]
Chandra (10^{-5})	0.1	65.62 ± 0.43	76.92 ± 0.30	64.20 ± 0.56	55.29 ± 0.54
	0.05	62.82 ± 0.66	76.92 ± 0.34	60.43 ± 0.94	55.08 ± 0.33
	0.01	56.21 ± 0.77	76.85 ± 0.36	55.30 ± 0.73	54.98 ± 0.48
	0.005	54.75 ± 0.96	76.95 ± 0.29	53.21 ± 0.54	55.09 ± 0.18
	0.001	52.77 ± 0.64	76.46 ± 0.07	52.16 ± 0.48	55.02 ± 0.30
Chandra (10^{-4})	0.1	88.69 ± 0.72	91.98 ± 0.04	86.46 ± 0.43	61.61 ± 0.24
	0.05	81.11 ± 0.35	91.80 ± 0.07	80.59 ± 0.74	60.68 ± 0.19
	0.01	69.77 ± 1.00	91.66 ± 0.12	69.76 ± 0.51	59.80 ± 0.17
	0.005	66.99 ± 0.65	91.63 ± 0.08	65.86 ± 0.41	59.48 ± 0.37
	0.001	61.81 ± 0.57	91.63 ± 0.13	62.18 ± 1.18	59.16 ± 0.25
XRISM	0.1	87.38 ± 0.32	41.22 ± 0.43	87.25 ± 0.71	29.69 ± 0.29
	0.05	83.47 ± 0.29	39.92 ± 0.51	82.05 ± 0.71	28.46 ± 0.32
	0.01	72.39 ± 0.83	39.14 ± 0.51	74.00 ± 0.42	28.24 ± 0.33
	0.005	69.57 ± 0.56	38.69 ± 0.23	69.84 ± 0.54	28.14 ± 0.43
	0.001	62.91 ± 0.81	38.63 ± 0.3	65.26 ± 0.44	28.03 ± 0.38
Athena	0.1	92.53 ± 0.43	94.12 ± 0.10	95.87 ± 0.56	86.34 ± 0.33
	0.05	89.12 ± 0.16	93.59 ± 0.09	93.31 ± 0.43	85.39 ± 0.28
	0.01	79.51 ± 0.24	92.80 ± 0.24	87.62 ± 0.39	83.84 ± 0.42
	0.005	76.52 ± 0.34	92.67 ± 0.15	84.46 ± 0.37	82.94 ± 0.38
	0.001	69.53 ± 0.85	92.36 ± 0.21	77.39 ± 0.57	82.71 ± 0.50

Table 4: Results of our trained models for all satellites and their configurations. Prediction accuracy of Virgo and Perseus cluster is represented by $M^V_{\rm acc}$, $M^P_{\rm acc}$ and parameter coverage is represented by $C^V_{\rm var}$, $C^P_{\rm var}$. Listed accuracy values were calculated from the cross-validation method.

4.2.3 *Triple-temperature model*

In addition, we conducted a test on triple-temperature component spectra simulated for the Virgo cluster to evaluate the performance of our algorithm on more than double-temperature plasma. This analysis was motivated by the fact that, according to the current literate (Frank K. A. et al., 2013; Rhea C. et al., 2020; de Plaa J. et al., 2010), in some clusters, we can detect up to 4 thermal components. The dataset for each model consists of 30000 synthetic spectra, with 10000 spectra of single, double, and triple-temperature components included. The temperature ranges were again selected by drawing upon studies investigating multiple-phase characteristics of the Virgo cluster (Liu H. et al., 2020; Werner N. et al., 2013). The single-temperature component

spectra were generated with temperature $1 - 4$ keV, the double-thermal component spectra with temperature $0.5 - 1.5$ keV, and the triple-thermal component spectra with temperature $0.3 - 0.7$ keV.

N_1^{max}	N_1^{min}	N_2^{max}	N_2^{min}	N_3^{max}	N_3^{min}	R_2^{min}	R_3^{min}
10^{-3}	10^{-5}	$10^{-5}(10^{-4})$	$5 \cdot 10^{-6}(5 \cdot 10^{-5})$	$10^{-5}(10^{-4})$	$10^{-6}(10^{-5})$	0.5	0.1

Table 5: Selected normalization parameters for triple-temperature models. N_3^{min}, N_3^{max} represents the minimum and maximum of the normalization range for the third thermal component. The R_2^{min}, R_3^{min} parameter is the ratio between the minimum normalization values of the second-first and third-first components. The numbers in brackets were selected for the second model for *Chandra* satellite.

(a) *Chandra* ($N_1^{min} = 10^{-5}$) (b) *Chandra* ($N_1^{min} = 10^{-4}$)

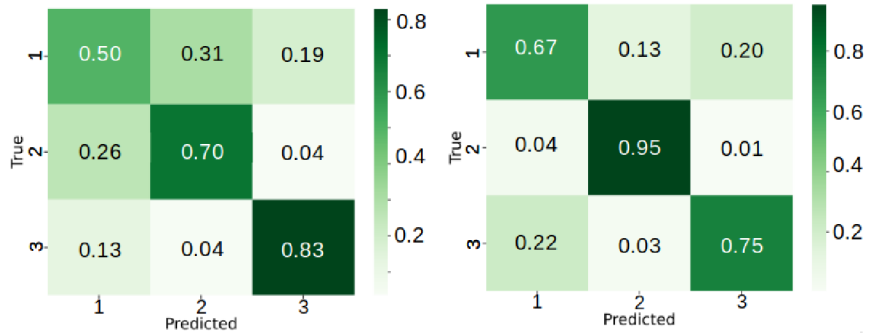

(c) *XRISM* (d) *Athena*

Figure 4.7: Selected confusion matrices for all triple-temperature component models .

From the selected confusion matrices in Figure 4.7 for each model, it is apparent that the algorithm is capable of detecting more than two thermal components in the spectrum. However, the model could not achieve the same accuracy as the two-temperature models, even though the normalization ranges were set slightly higher (see Table 3 and

Table 5). Despite these observations, the trend among satellites remains consistent: the *Athena* satellite continues to perform the best, while the *Chandra* satellite lags behind in the last place in both presented models.

Mission	$N_1^{\min}$	M_{acc}^V[%]	C_{var}^V[%]
Chandra	10^{-5}	53.38 ± 0.38	81.73 ± 0.28
	10^{-4}	67.47 ± 0.52	94.71 ± 0.04
XRISM	10^{-5}	68.89 ± 0.77	45.49 ± 0.36
Athena	10^{-5}	78.72 ± 0.30	96.01 ± 0.09

Table 6: Result prediction accuracy M_{acc}^V and component coverage C_{var}^V for triple-temperature models.

4.3 COMPARISON WITH XSPEC

To validate the performance of our trained RF models, we will compare them with the widely-used X-ray spectral analysis platform, XSPEC. For the evaluation, we generated a set of test data with a specified SNR (see Table 7) on which we examine the accuracy and speed of the models in comparison with XSPEC.

	Chandra		*XRISM*		*Athena*	
norm	SNR	Counts	SNR	Counts	SNR	Counts
10^{-3}	250	62500	350	122500	2100	4410000
$5 \cdot 10^{-4}$	170	28900	250	62500	1500	2250000
$5 \cdot 10^{-5}$	50	2500	80	6400	550	302500

Table 7: Signal-to-noise specifications for generated test sets of spectra for *Chandra*, *XRISM*, and *Athena* satellites.

The test spectra were generated as described in section 4.1.1, with the main thermal component matching the corresponding GC temperature ($1-4$ keV for Virgo and $2-5$ keV for Perseus) and the second thermal component mimicking the cooler temperature filaments ($0.5-0.75$ keV for Virgo and $0.6-0.85$ keV for Perseus). To ensure consistent signal-to-noise ratios for each test set, we fixed the normalization values N_1 and N_2. For the 1^{st}-thermal component, we used $N_1 = 10^{-3},\ 5 \cdot 10^{-4},\ 5 \cdot 10^{-5}$, while for the 2^{nd}-thermal component, we tied the normalizations to the 1^{st}-thermal component with ratios $N_2/N_1 = R_{2/1} = 0.1,\ 0.05,\ 0.01,\ 0.005,\ 0.001$. For each configuration, a total of one hundred single-temperature and double-temperature spectra were generated.

4.3.1 *XSPEC evaluation*

Extracting physical parameters of astrophysical sources, such as temperature or metallicity, requires the spectral fitting of the observed X-ray spectra. A crucial aspect of spectral analysis is the ability to distinguish between single and multi-temperature plasma components for which XSPEC platform is a widely-used and popular tool.

To evaluate the goodness of a fit and identify potential underlying components in the plasma, we used the χ^2 test statistic in our analysis. This statistical method compares the predicted fit to the spectral data and quantifies the differences between the two. To ensure the validity of the test, we binned the data to have at least one count per bin and have adequate degrees of freedom (*Chandra*: binning= 1, *XRISM*: binning= 20, *Athena*: binning= 500). The binning allows the independent random variables in each bin to be approximated by Poisson distribution. This enables the calculation of the expected counts for each bin, which are subsequently used in the calculation of the χ^2 value using the formula:

$$\chi^2 = \sum_{i=1}^{k} \frac{(A_i - E_i)^2}{E_i}, \tag{4.2}$$

where k is the number of classes and A_i, E_i is the number of observed and predicted counts in the i-th class (Liu H. and Setiono R., 1995). In order to obtain a precise evaluation of the goodness of the fit, it is necessary to calculate the reduced χ^2 statistic, which is defined as:

$$\chi^2_R = \frac{\chi^2}{\text{degrees of freedom}}. \tag{4.3}$$

In this section, we analyze the precision of XSPEC platform in identifying multi-temperature regions. To achieve this, we model both single and double-temperature spectra, perform spectral fitting analysis, and compare the results of individual fits. We introduce three criteria for classifying the synthetic test spectra as either single or double-temperature. Firstly, a good fit is indicated by a reduced χ^2_R value between $0.8 - 1.2$; otherwise, the algorithm does not include the fit in the final results. Secondly, the selection of the better fit, either single- or double-temperature, is based on the smaller value of the χ^2_R statistic. Thirdly, if the difference between the χ^2_R values of both fits for a given spectrum is less than 1% of the maximum difference allowed by the first condition, the simpler model (single-temperature) is chosen as, the better fit.

For the spectral fitting process, we used the default *levmar* method in XSPEC. Our approach involved fitting the normalization, temperature, and abundance independently. Although XSPEC offers more advanced and precise methods for spectral fitting, we chose this method due to its superior speed and sufficient fit statistics, which met our first criteria in 99.9% of the 12000 test spectra.

GC	SNR	$R_{2/1}$	XSEPC	$M^a{}_{0.1}$	$M^a{}_{0.05}$	$M^a{}_{0.01}$	$M^a{}_{0.005}$	$M^a{}_{0.001}$	$M^b{}_{0.1}$	$M^b{}_{0.05}$	$M^b{}_{0.01}$	$M^b{}_{0.005}$	$M^b{}_{0.001}$
Virgo	50	0.1	61.5	60.0	55.0	59.0	57.0	59.0	50.5	54.5	54.5	52.0	55.0
		0.05	53.5	52.0	51.0	53.5	54.0	56.5	55.0	48.5	50.5	51.0	54.0
		0.01	50.5	52.0	51.0	53.5	54.0	61.0	51.5	51.0	49.5	51.0	55.0
		0.005	51.0	47.5	47.5	53.5	45.5	48.0	51.5	52.0	53.5	52.5	50.5
		0.001	49.0	47.0	50.5	52.5	45.0	48.5	51.0	50.5	53.5	50.5	53.0
	170	0.1	95.0	76.5	65.5	58.0	52.5	58.5	57.5	67.0	66.0	58.0	59.5
		0.05	90.0	59.0	56.0	54.0	60.0	49.0	69.5	50.5	49.5	52.0	50.5
		0.01	56.5	59.0	56.0	54.0	60.0	49.0	51.5	51.0	50.0	45.5	50.5
		0.005	54.5	53.5	47.0	48.0	52.5	52.5	53.5	49.5	46.5	47.0	49.5
		0.001	51.0	50.5	48.5	52.5	53.0	49.5	51.0	48.5	46.5	43.5	46.5
	250	0.1	95.5	76.5	61.0	63.0	64.0	62.0	65.0	73.5	68.5	70.0	65.5
		0.05	94.0	57.5	56.5	52.5	56.0	54.0	74.0	52.0	52.0	52.5	54.0
		0.01	62.0	57.0	56.5	52.5	56.0	54.0	50.0	50.5	48.0	48.5	51.0
		0.005	53.5	49.5	49.0	55.0	56.0	56.0	51.0	52.0	51.5	49.0	47.5
		0.001	52.5	52.5	47.0	57.0	57.0	48.5	54.0	53.5	51.5	49.5	47.0
Perseus	50	0.1	64.5	72.0	71.5	61.0	55.0	58.5	66.5	69.0	71.0	72.0	66.5
		0.05	53.0	64.0	63.5	52.5	49.0	56.5	59.0	64.0	65.5	66.0	61.0
		0.01	49.0	49.5	50.5	44.5	47.5	50.5	46.0	47.0	45.5	48.5	47.0
		0.005	49.0	48.5	54.0	44.5	45.0	52.0	51.5	55.5	53.0	53.5	54.0
		0.001	51.0	49.0	52.0	46.5	47.5	46.5	49.0	46.5	49.5	49.0	48.0
	170	0.1	97.0	75.5	71.5	64.5	72.0	59.0	89.5	92.5	87.5	84.0	85.0
		0.05	92.0	69.0	66.0	59.5	60.5	56.5	75.5	82.5	80.5	73.0	76.5
		0.01	52.5	60.5	49.5	56.0	62.0	51.5	57.0	58.0	58.0	57.0	62.5
		0.005	49.0	50.0	51.0	55.0	57.0	55.5	46.5	48.5	48.5	49.5	50.5
		0.001	49.0	49.5	48.0	54.0	52.5	52.0	44.5	47.0	53.0	50.0	52.5
	250	0.1	97.5	75.5	74.0	66.5	68.0	56.0	94.0	96.0	80.5	76.0	85.5
		0.05	95.0	70.5	71.5	57.0	59.5	53.0	88.5	92.5	78.5	75.0	84.0
		0.01	58.0	56.5	58.5	57.0	50.5	44.5	56.5	62.0	58.5	56.0	62.0
		0.005	52.5	55.0	51.5	53.5	52.5	49.5	52.0	55.0	50.0	47.0	51.5
		0.001	48.5	47.0	56.0	54.0	49.5	44.5	56.0	57.0	48.5	48.0	61.5

Table 8: The capability of the XSPEC platform to distinguish between spectra containing single and double-temperature components, as well as the accuracy of our RF models on the same spectra evaluated for the *Chandra* mission. The M parameter represents the performance of RF models on test data based on their signal-to-noise ratio and $R_{2/1}$ parameter. The bottom numbers at parameter M are the $R_{\min}$ values, described in Section 4.2.1.

a model trained on data with $N_1^{\min} = 10^{-5}$
b model trained on data with $N_1^{\min} = 10^{-4}$

Mission	SNR	$R_{2/1}$	XSEPC^a	$M^a_{0.1}$	$M^a_{0.05}$	$M^a_{0.01}$	$M^a_{0.005}$	$M^a_{0.001}$	XSEPC^b	$M^b_{0.1}$	$M^b_{0.05}$	$M^b_{0.01}$	$M^b_{0.005}$	$M^b_{0.001}$
XRISM	80	0.1	94.0	99.0	99.0	96.5	81.0	95.5	48.5	47.0	56.0	54.0	49.5	44.5
		0.05	93.5	98.5	97.5	93.5	94.5	93.5	95.0	97.5	98.5	94.0	94.0	94.0
		0.01	93.5	59.5	64.5	71.0	68.5	68.5	74.5	56.5	64.0	68.0	72.0	71.0
		0.005	68.0	53.5	57.5	57.0	65.5	58.5	63.5	51.0	54.5	50.5	58.5	56.0
		0.001	48.5	49.5	51.5	51.0	48.5	49.0	53.0	49.0	52.0	51.5	51.5	50.5
	250	0.1	98.0	86.5	86.0	80.5	85.0	79.5	99.5	87.5	87.5	83.5	81.0	79.5
		0.05	99.5	86.5	86.0	80.5	85.0	79.0	99.5	87.5	87.5	83.5	81.0	79.5
		0.01	97.0	82.0	81.0	75.5	81.0	75.0	96.0	82.5	85.0	82.0	80.0	78.0
		0.005	86.5	72.5	71.0	67.0	70.0	63.5	73.5	68.5	73.0	71.5	71.0	68.0
		0.001	53.5	52.5	55.5	54.0	58.5	53.5	51.5	56.0	54.0	50.5	53.0	51.5
	350	0.1	100.0	81.5	76.5	75.0	81.5	76.0	100.0	83.5	79.5	77.5	78.5	75.5
		0.05	98.5	81.0	76.5	75.0	81.5	76.0	100.0	83.5	79.5	77.5	78.5	75.5
		0.01	98.5	79.0	72.5	73.5	78.0	70.0	97.5	83.0	78.5	77.0	77.5	73.5
		0.005	87.5	75.5	68.0	66.0	70.0	66.0	82.5	74.5	73.5	71.5	72.0	67.5
		0.001	53.0	57.0	51.5	56.0	60.5	59.0	50.0	52.0	50.0	48.5	50.5	51.5
Athena	550	0.1	96.5	99.0	96.5	96.5	93.5	92.5	95.0	99.0	100.0	99.0	99.0	95.0
		0.05	97.0	99.0	96.5	96.5	93.5	92.0	95.0	99.0	100.0	99.0	99.0	95.0
		0.01	96.5	83.0	83.5	87.5	85.0	82.0	94.5	85.5	88.5	97.5	98.0	94.0
		0.005	96.5	65.5	67.5	67.5	72.0	75.5	92.5	61.5	64.0	86.5	92.5	92.0
		0.001	81.0	54.5	55.5	54.0	52.0	57.0	67.0	51.0	52.0	53.0	54.5	62.5
	1500	0.1	99.5	96.0	92.5	91.5	91.5	84.0	100.0	98.0	98.0	97.0	94.0	87.5
		0.05	100.0	96.0	92.5	91.5	91.5	83.5	100.0	98.0	98.0	97.0	94.0	87.5
		0.01	99.5	90.5	91.0	89.0	91.0	80.5	100.0	98.0	98.0	96.5	94.0	87.5
		0.005	99.5	80.0	81.0	80.0	83.5	74.5	100.0	92.5	95.5	94.0	93.5	87.5
		0.001	94.5	51.0	56.5	59.5	60.5	62.5	92.5	54.5	54.5	67.0	71.0	74.0
	2100	0.1	100.0	96.5	94.5	93.5	94.0	85.0	100.0	98.5	94.0	95.5	97.0	91.0
		0.05	100.0	96.5	94.5	93.5	94.0	84.5	100.0	98.5	94.0	95.5	97.0	91.0
		0.01	100.0	94.5	93.5	91.5	92.0	82.0	100.0	98.5	94.0	95.5	97.0	91.0
		0.005	99.5	84.5	87.5	86.5	88.5	77.5	100.0	96.5	93.5	94.0	97.0	91.0
		0.001	98.5	51.5	53.5	60.5	59.0	57.0	94.0	56.0	59.5	72.5	76.5	79.0

Table 9: The capability of the XSPEC platform to distinguish between spectra containing single- and double-temperature components, as well as the accuracy of our models on the same spectra evaluated for the *XRISM* and *Athena* missions. The M parameter represents the performance of our models on test data based on their signal-to-noise ratio and $R_{2/1}$ parameter. The bottom numbers at parameter M are the R_{min} values, described in Section 4.2.1.

a values for Virgo-like spectra
b values for Perseus-like spectra

4.4 TESTS ON REAL OBSERVATIONS

To further evaluate the performance and effectiveness of our models, we conducted a test on real observations of the Virgo and Perseus clusters (see Table 10). Since from the investigated missions, *Chandra* is the only satellite with available observations, we explored only this mission in the test. For the purpose of this analysis, we chose to examine the observations of M87 (member of the Virgo cluster) and NGC1275 galaxy (member of the Perseus cluster). These two objects are one of the brightest and most massive exemplars in each cluster and comprise a wide range of temperatures, making them ideal targets for detailed multi-temperature studies.

GC	Object	ObsID	Detector	Exposure time [ks]	Date
Virgo	M87	18856	ACIS-S	25.46	2016
Perseus	NGC1275	1513	ACIS-S	24.88	2000

Table 10: Selected observations for objects in Virgo and Perseus cluster.

Both observations were obtained from *Chandra* Search & Retrieval archive *ChaSeR* (Harvard-Smithsonian Center for Astrophysics, 2021) and were selected for several reasons: their exposure time is comparable and long enough for good count statistics, and in both of the cases the detector device ACIS-S matches the instrument chosen for generating the synthetic spectra. Our aim is to extract real spectra from selected regions (see Figure 4.9), use XSPEC platform to determine the number of underlying components, and subsequently apply our models to the same spectrum.

4.4.1 *Data processing*

The processing of the data, starting with the initial level I file provided by the CXC, was done using the *Chandra* Interactive Analysis of Observations (CIAO) software package (version 4.15) that stores required calibration files in *Chandra* Calibration Database CALDB (version 4.10.2). In order to create quality spectra from selected regions, we followed the reduction and cleaning procedures described below.

The data was reprocessed to create level 2 event file using `chandra_repro` tool, followed by the detection of background and bright sources using `vtpdetect` routine and their subtraction from the original image (see Figure 4.9). In addition, we used `lc_sigma_clip` routine to filter remaining flares with 3σ factor. The final exposure times corrected by the filtering were for Virgo 25.21 ks and for Perseus 24.29 ks.

Moreover, a background file was created for each observation using the ASIC-S calibration files stored in the CALDB with `blansky` script. These files were subsequently used as background files in later analyses. A total of 20 regions were chosen for spectrum extraction using the contour analysis feature in the *SAOImageDS9* imaging tool,

with 10 regions being selected for each cluster. The selection was made based on the cluster's existing temperature maps and the number of counts in each region, which ranged from 800 to 6000 counts (see Table 11). The spectra for each region were extracted from the processed event file and the created background file using specextract tool and analyzed with Sherpa fitting package.

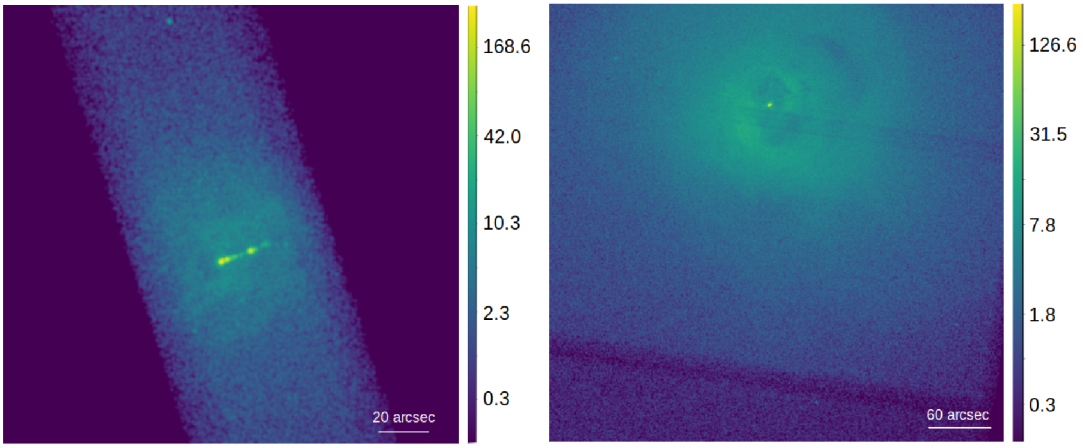

(a) Original data for Virgo

(b) Original data for Perseus

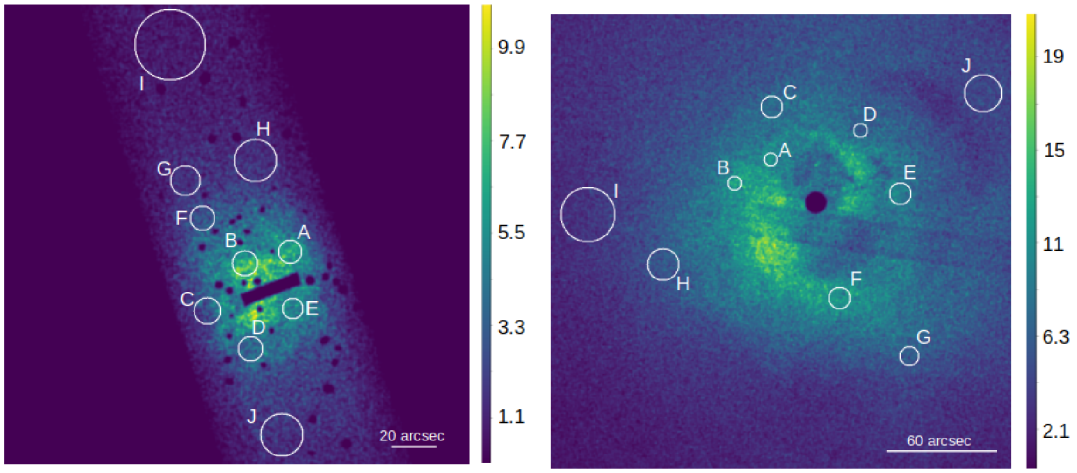

(c) Cleaned data for Virgo

(d) Cleaned data for Perseus

Figure 4.8: Selected *Chandra* observations (upper row) and reprocessed images with subtracted bright and background sources and outlined regions, later used in the analysis (lower row) visualized in *SAOImageDS9* application.

4.4.2 *Data fitting and comparison with models*

In order to determine the number of underlying components present in the extracted spectra, we employed a fitting approach using XSPEC, which was similar to that described in section 4.3.1 with few adjustments.

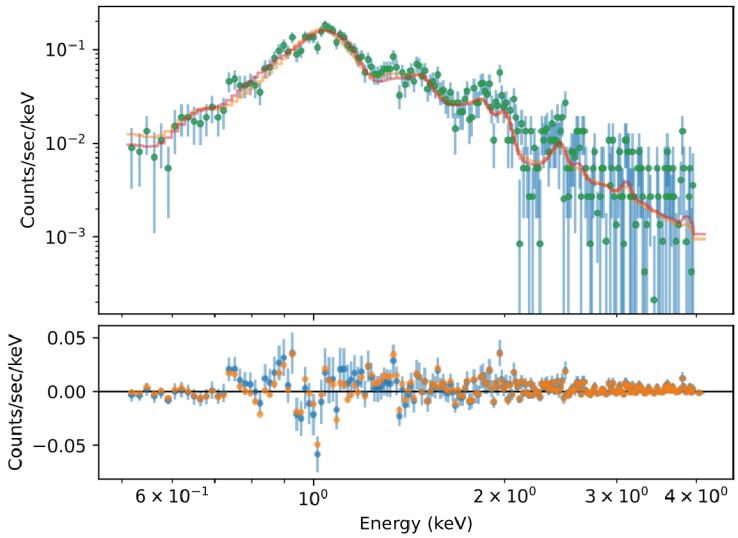

(a) Spectrum from region B in Virgo cluster

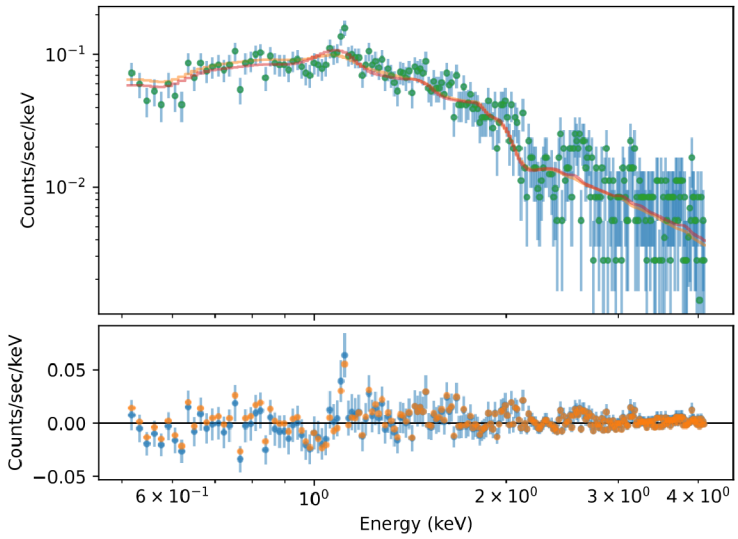

(b) Spectrum from region A in Perseus cluster

Figure 4.9: Selected spectra that were classified as double-temperature. Upper parts of the graphs: Extracted spectra fitted with single (orange) and double-temperature (red) models using Sherpa application. Lower parts of the graphs: Difference between observed data and single (blue), double-temperature (orange) models.

After the binning was applied to the data, the background spectrum was subtracted from each region. A power-law model with a photon index fixed to 1.56 was included in the fitting procedure to account for potential non-thermal processes (Irwin J. A. et al., 2003). The remaining parts of the algorithm were kept unchanged. The XSPEC model, which was characterized by better statistics, was subsequently considered to be the ground truth, and the RF model predictions were compared to this established model. Table 11 shows the final classifications derived from the best fits of the XSPEC models for spectra in each selected region.

	Virgo		Perseus	
Region	Class	Counts	Class	Counts
A	Single	2106	Double	2757
B	Double	2636	Double	3662
C	Single	1268	Double	4864
D	Single	1362	Single	1225
E	Single	1047	Single	4815
F	Single	865	Double	5425
G	Single	1462	Single	2446
H	Single	1718	Single	4971
I	Single	1682	Single	3140
J	Single	2315	Single	3026

Table 11: Classification results from XSPEC on selected regions and their number of counts.

The overall prediction accuracy of our models on all selected regions in real observations is presented in Table 12. The results indicate that the models could identify

$N_1^{\min}$	GC	$M_{0.1}$[%]	$M_{0.05}$[%]	$M_{0.01}$[%]	$M_{0.005}$[%]	$M_{0.001}$[%]
10^{-4}	Virgo	80	80	60	40	40
	Perseus	60	60	50	40	40
10^{-5}	Virgo	70	70	60	50	50
	Perseus	60	50	50	40	40

Table 12: Accuracy of models on all regions selected from real *Chandra* observations.

some of the key features in the synthetic data, successfully apply those findings to the real observation, and predict the presence of multi-temperature components with reasonable accuracy. Although the models demonstrated comparable performance on the synthetic data (see Figure 4.6), their performance differs when applied to real data,

as can be seen in Table 12, where the models developed for the Virgo cluster outperformed those developed for the Perseus cluster.

The results for the Perseus cluster could be attributed to the relatively lower coverage of parameter variance in the models for the Perseus cluster compared to those for the Virgo cluster (see Figure 4.6). Another potential factor contributing to the confusion of the algorithm could be our assumption of single-temperature and double-temperature plasma within the clusters. The selected regions in the Perseus cluster could contain more than two thermal components (see Section 4.2.3), which would introduce additional uncertainty to the outcome. Nonetheless, all the findings suggest that the models have the potential to identify complex spectral components in a variety of astrophysical environments.

5

DISCUSSION & FUTURE WORK

The results obtained in this study provide insight into the performance of the machine learning technique used for identifying the number of underlying components in X-ray spectra for galaxy clusters. By simulating both single and double-temperature plasma and training the RF algorithm on the spectra processed by PCA, we were able to successfully classify input spectra based on the number of thermal components. The validation on a test set demonstrated the efficacy of the algorithm and the superiority of *Athena* observatory over *Chandra* and *XRISM* satellites for both galaxy clusters. In this Chapter, we look into the limitations of our methodology, the factors that can impact the outcomes of the models we constructed, and outline the potential avenues of future research.

5.1 PRINCIPAL COMPONENTS

As discussed in Section 3.1.1, the principal component analysis (PCA) method effectively reduces the challenge of high dimensionality by transforming the data into a linear combination of eigenspectra $\vec{v}_j$ and mean emission $\vec{\mu}$ (see Equation 3.5). The eigenspectra represent the primary components projected onto the initial basis, and the selected sample for each satellite is shown in Figure 5.1. Notably, the PCA successfully captures the main variations in the soft X-ray region (ranging from 0.5 to 2 keV), which is expected to occur due to the modelling of mostly diffuse gas that primarily emits in this regime.

The physical interpretation of the individual eigenspectra is often an issue in the PCA. The problem lies in that the newly defined variables are usually linear functions of all the original variables. Therefore, many new variables have non-trivial coefficients, making the components difficult to interpret. However, with a thorough review of the relevant literature and a close examination of the eigenspectra presented in Figure 5.1 (Folkes S. et al., 1999; Jolliffe I. T. and Cadima J., 2016; Rhea C. et al., 2021), it is possible to suggest that the first two principal components captured by the algorithm for the *Chandra* satellite represent the Fe-L/Ne emission line complex close after 1 keV, resulting from the instrument's relatively poor energy resolution. However, the features captured by other displayed principal components for this satellite may require further investigation to be clearly interpreted.

The energy resolution of the *XRISM* and *Athena* satellites is undoubtedly better than that of the *Chandra* mission. This is reflected also in the eigenspectra and mean emission, which captured fine emission line structures visible in Figure 5.1 (see also

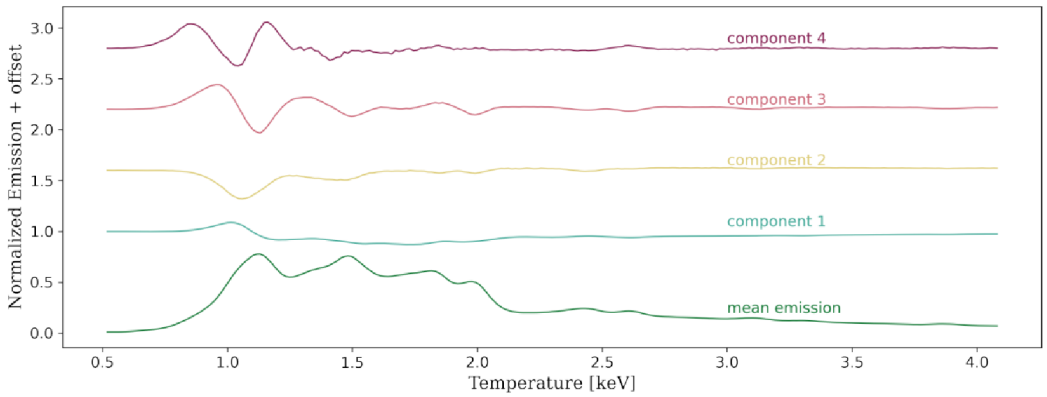

(a) *Chandra*

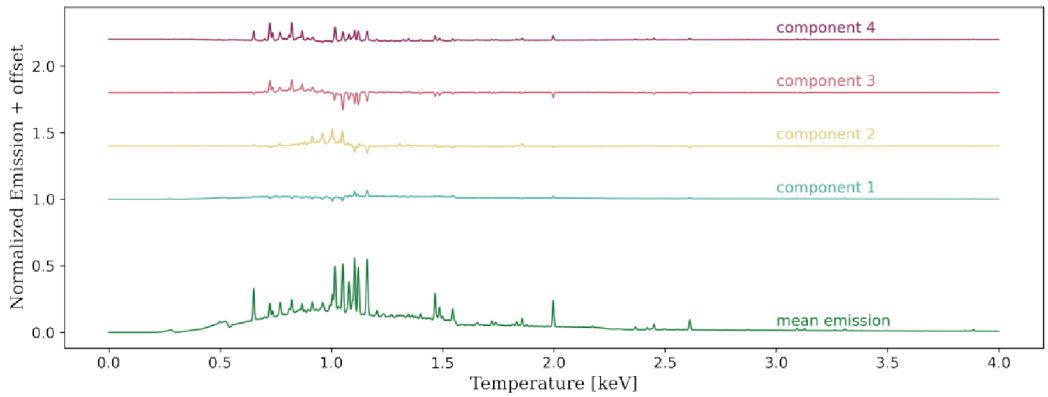

(b) *XRISM*

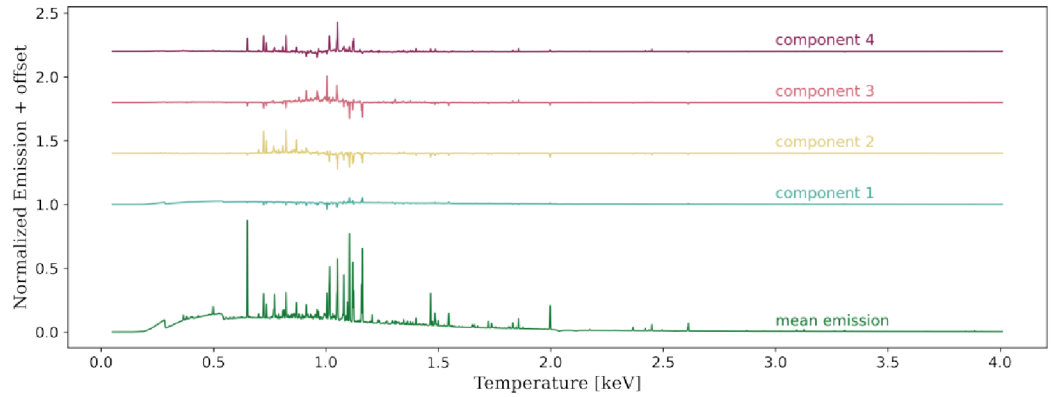

(c) *Athena*

Figure 5.1: Visualization of the first four principal components and the linear combination of all 25 components (mean emission) for investigated observatories. The components corresponds to model with $N_1^{\min} = 10^{-5}$ and $R_{\min} = 0.1$.

Appendix C). However, interpreting the eigenspectra for these satellites is still very difficult and requires additional investigation. Despite this, it is clear from the figure that *Athena* outperforms both *XRISM* and *Chandra* satellites and therefore has great potential to advance our understanding of obscured fields.

5.2 SATELLITES PERFORMANCE

The resulting prediction accuracy presented in Figure 4.6 and Table 4 demonstrates that the *Athena* observatory has performed exceptionally well across all models compared to the *Chandra* and *XRISM* satellites. This result was anticipatable and may be attributed to the outstanding spacecraft architecture of *Athena*, which has an effective area of 2 m^2, enabling it to capture a significantly higher number of photons and hold a better energy resolution as illustrated in Table 1. *Athena*'s favorable performance and the underperformance of the other satellites can be further drawn from the dependencies of the principal components (see Appendix B).

Since we investigated double temperature spectra with carefully balanced normalization ratios between their thermal constituents, the principal components did not segregate into visually distinct regions. Nonetheless, we can observe specific trends for the different number of underlying temperatures. For example, one of the trends can be observed in Figure B.1 generated for *Chandra* satellite, where the second principal component in single-temperature spectra gradually descends towards a negative value of -2 before changing direction and ascending towards a positive value. If a test spectrum falls near this trend line, it is highly probable to be categorized as a single-temperature spectrum. Similar or more intricate trends can also be seen in the component dependencies graphs of the *XRISM* and *Athena* satellites.

A noteworthy finding is that the strength of correlation among principal components is heightened as the signal-to-noise ratio of the thermal components increases (marked by the R_{min} value, corresponding to the normalization ratios). This pattern is consistently observed across all satellites and is noticeable from the graphs in Appendix B.

In addition, we tested the algorithm on triple-temperature plasma using the same architecture as for double-temperature spectra. Although the achieved accuracy was lower than that of the two-temperature models, the successful application of the algorithm on more complex datasets highlights its potential for further development and optimization to achieve greater accuracy in the future.

5.2.1 *Accuracy and speed*

To further evaluate our models, we conducted additional tests to compare their accuracy and efficiency with the current spectral analysis tool, XSPEC platform. While our

models were not designed to outperform the XSPEC but rather to expedite the classification process, they still achieved remarkable accuracies, which are approaching the same level of accuracy as XSPEC and, in some cases, are almost comparable. The results of these tests are presented in Tables 8 and 9.

Although none of the models for the *Chandra* satellite were able to surpass the performance of XSPEC platform, most of them were approaching its accuracy, especially those applied on spectra with the highest normalization ratios of the first and second thermal component ($R_{2/1} = 0.1$) and the highest signal-to-noise ratios (SNR $= 250$). The model's best prediction accuracy of 96.0% was achieved for the Perseus-like cluster, which is only slightly below the XSPEC's accuracy of 97.5%. For the Virgo-like cluster, we achieved the best prediction accuracy of 76.5%, which is still a highly accurate result.

A similar analysis performed for *XRISM* and *Athena* observatories (see Table 9) revealed significant improvements compared to the *Chandra* satellite. The models showed promising results and even outperformed XSPEC in some scenarios, mainly for spectra with the highest normalization ratios of the first and second thermal component ($R_{2/1} = 0.1$) and the lowest signal-to-noise ratios (SNR $= 80,550$). Specifically, the *XRISM* models attained an impressive 99.0% accuracy and the *Athena* models 99.5% accuracy, while the precision of the XSPEC platform was only 94.0% and 96.5%, respectively. However, the models experienced a decrease in accuracy for spectra with lower $R_{2/1}$ values and were unable to achieve the same level of precision as XSPEC in most cases.

Our models, while in most cases not achieving the same or higher accuracy as the XSPEC platform, demonstrated a remarkable advantage in terms of speed for analysis. In comparison to the standard fitting procedure using the *levmar* method in SHERPA that took approximately 9 seconds to classify one spectrum for *Chandra*, 25 seconds for *XRISM*, and 122 seconds for *Athena*, our ML approach was able to classify 100 spectra in only 0.5 seconds for *Chandra* ($\sim 1800x$ faster), 23 seconds for *XRISM* ($\sim 110x$ faster), and 14 seconds for *Athena* ($\sim 870x$ faster). This significant decrease in analysis time highlights the potential of ML algorithms to enhance the efficiency of spectral analysis in astrophysics, especially when dealing with large datasets such as those anticipated from future satellite missions like *Athena*.

In particular, this method could facilitate the preliminary data analysis phase by quickly identifying regions of interest in the observations, which could then be subjected to more detailed analysis using more accurate conventional fitting procedures. A promising strategy for advancing our analysis could be integrating a feature that can precisely determine the temperature of each underlying component. This modification could also speed up the process of finding the regions of interest, resulting in increased efficiency.

5.2.2 *Chandra performance on real observation*

The performance of the models on synthetic data seems to be unaffected by the principal component variance coverage, which is significantly different for each galaxy cluster for all satellites, with models for the Perseus cluster covering less dataset variability. However, when we test the *Chandra* models on the real observations (see Section 4.4 and Appendix D), the models applied to the Virgo cluster performed noticeably better than the models applied to Perseus.

The observed differences between the two clusters may be attributed to the diversity between the model's parameter variance coverage (see Figure 4.6) or to the fact that we selected regions within the Perseus cluster that might have contained additional thermal components beyond the ones we accounted for (see Section 4.2.3), although this hypothesis would require further inspection. Nonetheless, it should be noted that the models developed for both the Virgo and Perseus clusters successfully found the same features they were trained on in real observations.

To further enhance the accuracy of the models, additional physical parameters can be incorporated, and different ML algorithms and techniques could be explored. Moreover, it would be insightful to extend the application of the models to a wider range of galaxy clusters and compare the results.

6 CONCLUSION

In order to expedite the current analysis process, we explored a machine learning approach based on *Principal Component Analysis* and *Random Forest Classifier* to analyze the multi-temperature regions in Virgo-like and Perseus-like galaxy clusters using synthetic data from the *Athena*, *XRISM* and *Chandra* X-ray observatories. Our research was primarily motivated by the enormity of data that is expected to be collected by the forthcoming *Athena* observatory and the challenge of analyzing these vast datasets using conventional fitting methods, which are both time-consuming and computationally expensive. To thoroughly investigate the capabilities of individual satellites, we trained multiple models for each observatory, differing in the normalization ratio of the first and second thermal components (R^{min}).

The models were initially trained and tested on synthetic single and double temperature spectra as outlined in Section 4.2.2, where the resulting accuracy of the prediction demonstrates the *Athena* observatory's superiority. Specifically, the accuracies of *Athena*'s models range from approximately $92\% - 69\%$ for the Virgo cluster and $95\% - 77\%$ for the Perseus cluster, respectively. In comparison, the *XRISM* satellite follows closely behind *Athena* with accuracies ranging from $87\% - 62\%$ for the Virgo cluster and $87\% - 65\%$ for the Perseus cluster. Lastly, the *Chandra* satellite's performance falls behind with accuracies of $65\% - 52\%$ for the Virgo cluster and $64\% - 52\%$ for the Perseus cluster, in case of the same normalization ratio. The exact values of individual models are listed in Table 4.

Additionally, the performance of the algorithm with identical architecture was tested on triple-temperature plasma, which successfully demonstrated its ability to effectively process more complex data sets and its potential for further improvement and application.

In Section 4.3, we compare the performance of our models with the widely-used X-ray spectral analysis platform, XSPEC. For this purpose, we generated a new testing dataset with a specified signal-to-noise ratio (SNR) (see Table 7). The model's prediction accuracy was evaluated with the confusion matrices in the same way as in previous measurements. Within the XSPEC platform, we used a standard fitting procedure to identify potential underlying components in the plasma with reduced χ^2 statistics. In cases of high SNR data, the best-performing RF models for *XRISM* and *Athena* achieved impressive 99.0% and 99.5% accuracy, respectively, whereas the precision of the XSPEC platform was only 94.0% and 96.5%. As the SNR decreased, all the RF models and XSPEC experienced a decrease in accuracy. However, the models' accuracy dropped more rapidly, leading to better performance by XSPEC in most cases.

Although it was anticipated that the XSPEC platform would outperform our models, they exhibited promising results and demonstrated exceptional advantage in the speed of the analysis process. The speed gains with the *Athena* models were approximately 870 times faster, *XRISM* 110 times faster, and *Chandra* 1800 times faster. This noteworthy reduction in analysis time suggests that the method could be implemented in the early analysis phase, allowing for the rapid identification of regions of interest that could be further investigated using conventional fitting techniques to achieve greater accuracy.

Finally, the performance of the *Chandra* models was validated using real observations of M87 (for the Virgo cluster) and NGC1275 (for the Perseus cluster). The observational data were processed and cleaned using standard methods outlined in Section 4.4.1. Ten selected regions in each observation (see Figure 4.9) were then subjected to our models. The number of underlying thermal components was determined by the more precise fitting procedure in XSPEC, following the application of our RF models. The implemented models were successfully applied to the selected regions, and the top-performing models, which had the highest $R^{\min}$ value compared to the XSPEC classification, achieved an 80% accuracy for the Virgo cluster and a 60% accuracy for the Perseus cluster (see Table 12)

In summary, our study has revealed that machine learning techniques offer the capacity to efficiently classify multi-temperature regions in galaxy clusters while significantly reducing the analysis time compared to traditional fitting procedures. Furthermore, the findings demonstrate the extraordinary capabilities of the *Athena* satellite to advance our understanding of the properties and evolution of hot gas in galaxy clusters.

APENDIX A: CONFUSION MATRICES

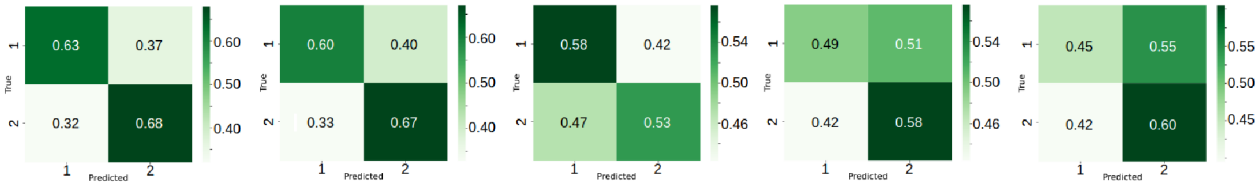

(a) $R^{\min} = 0.1$ (b) $R^{\min} = 0.05$ (c) $R^{\min} = 0.01$ (d) $R^{\min} = 0.005$ (e) $R^{\min} = 0.001$

Figure A.1: Confusion matrices for *Chandra* models with $N_1^{\min} = 10^{-5}$ for Virgo cluster.

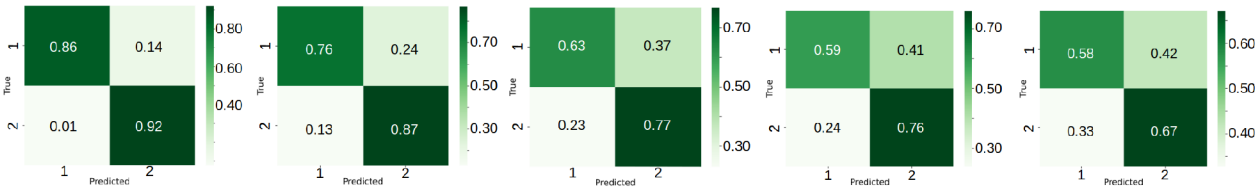

(a) $R^{\min} = 0.1$ (b) $R^{\min} = 0.05$ (c) $R^{\min} = 0.01$ (d) $R^{\min} = 0.005$ (e) $R^{\min} = 0.001$

Figure A.2: Confusion matrices for *Chandra* models with $N_1^{\min} = 10^{-4}$ for Virgo Cluster.

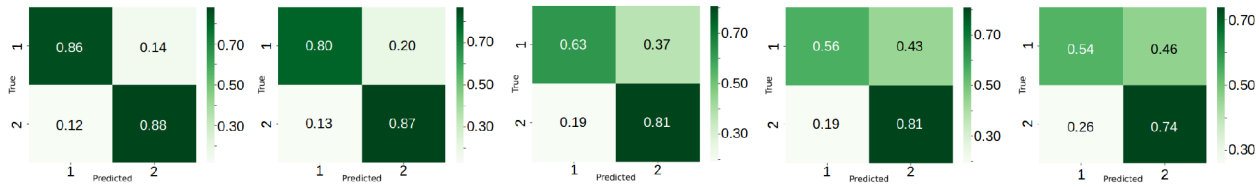

(a) $R^{\min} = 0.1$ (b) $R^{\min} = 0.05$ (c) $R^{\min} = 0.01$ (d) $R^{\min} = 0.005$ (e) $R^{\min} = 0.001$

Figure A.3: Confusion matrices for `XRISM` models for Virgo Cluster.

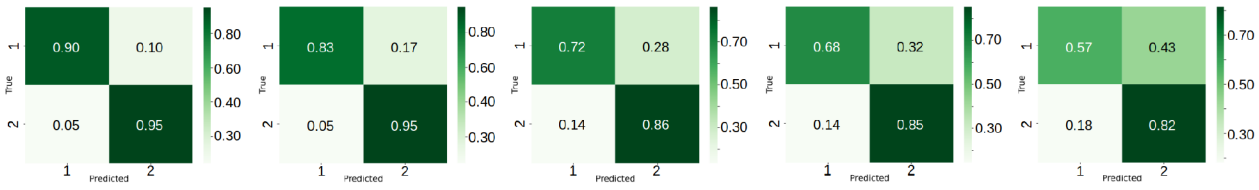

(a) $R^{\min} = 0.1$ (b) $R^{\min} = 0.05$ (c) $R^{\min} = 0.01$ (d) $R^{\min} = 0.005$ (e) $R^{\min} = 0.001$

Figure A.4: Confusion matrices for *Athena* models for Virgo Cluster.

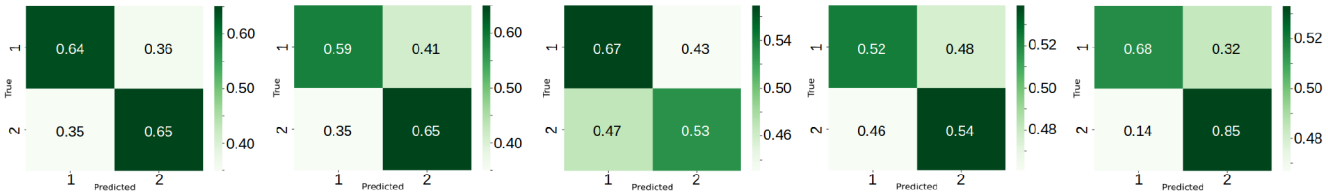

(a) $R^{\min} = 0.1$ (b) $R^{\min} = 0.05$ (c) $R^{\min} = 0.01$ (d) $R^{\min} = 0.005$ (e) $R^{\min} = 0.001$

Figure A.5: Confusion matrices for *Chandra* models with $N_1^{\min} = 10^{-5}$ for Perseus cluster.

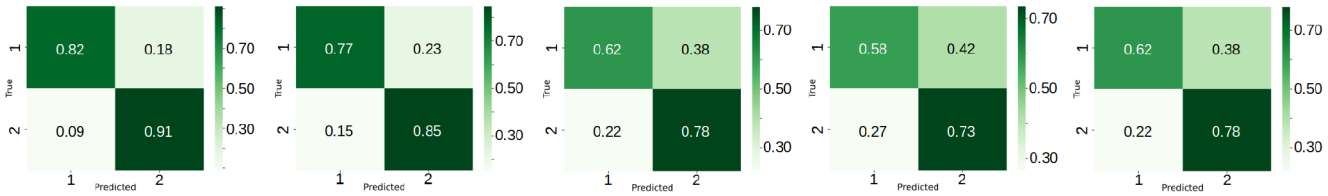

(a) $R^{\min} = 0.1$ (b) $R^{\min} = 0.05$ (c) $R^{\min} = 0.01$ (d) $R^{\min} = 0.005$ (e) $R^{\min} = 0.001$

Figure A.6: Confusion matrices for *Chandra* models with $N_1^{\min} = 10^{-4}$ for Perseus Cluster.

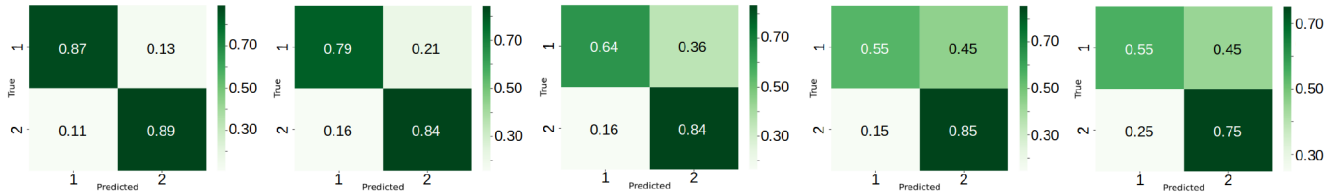

(a) $R^{\min} = 0.1$ (b) $R^{\min} = 0.05$ (c) $R^{\min} = 0.01$ (d) $R^{\min} = 0.005$ (e) $R^{\min} = 0.001$

Figure A.7: Confusion matrices for `XRISM` models for Perseus Cluster.

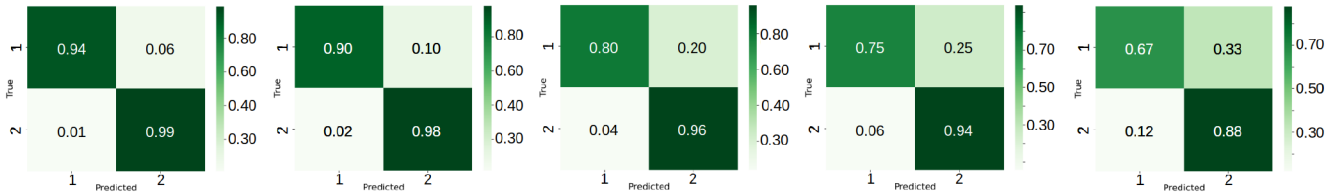

(a) $R^{\min} = 0.1$ (b) $R^{\min} = 0.05$ (c) $R^{\min} = 0.01$ (d) $R^{\min} = 0.005$ (e) $R^{\min} = 0.001$

Figure A.8: Confusion matrices for *Athena* models for Perseus Cluster.

B

APPENDIX B: PRINCIPAL COMPONENT DEPENDENCIES

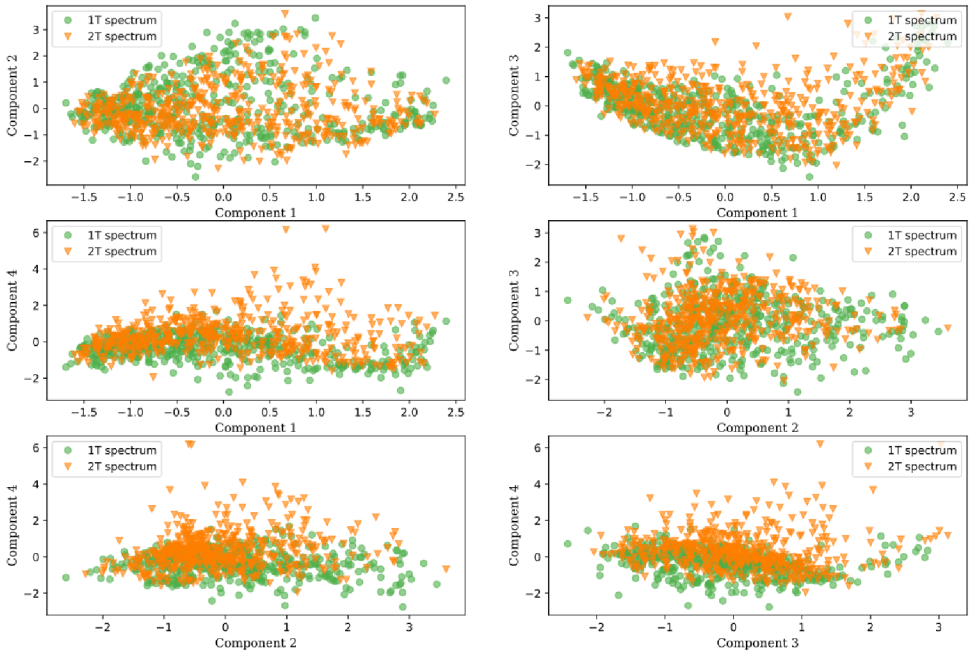

(a) $R^{\min} = 0.1$

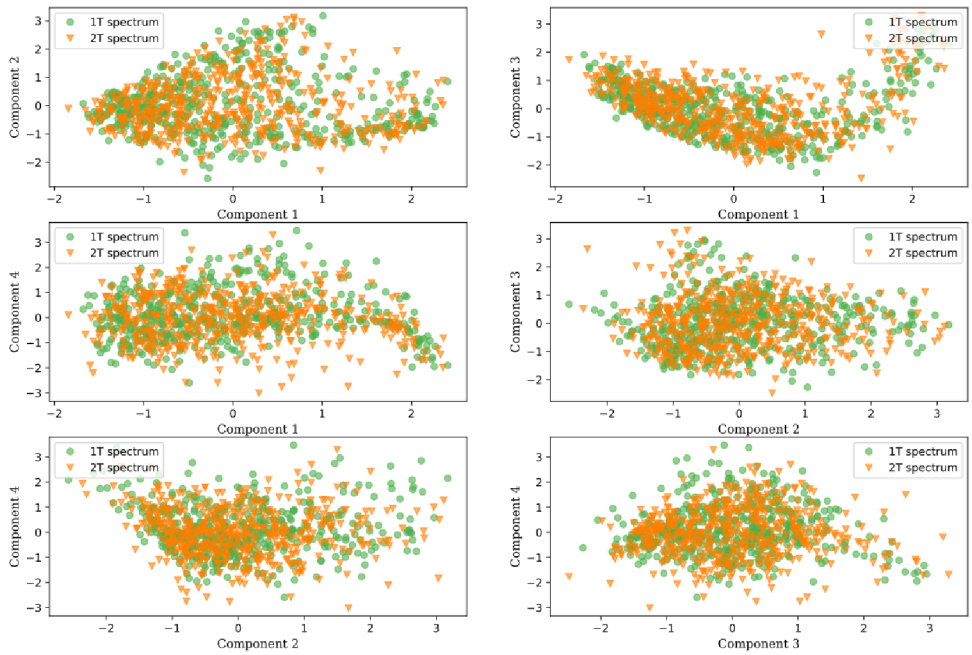

(b) $R^{\min} = 0.001$

Figure B.1: The interdependence of the initial four principal components for 500 single (circle) and double (triangle) temperature spectra of the *Chandra* satellite pertaining models with $N_1^{\min} = 10^{-5}$ for the Virgo Cluster.

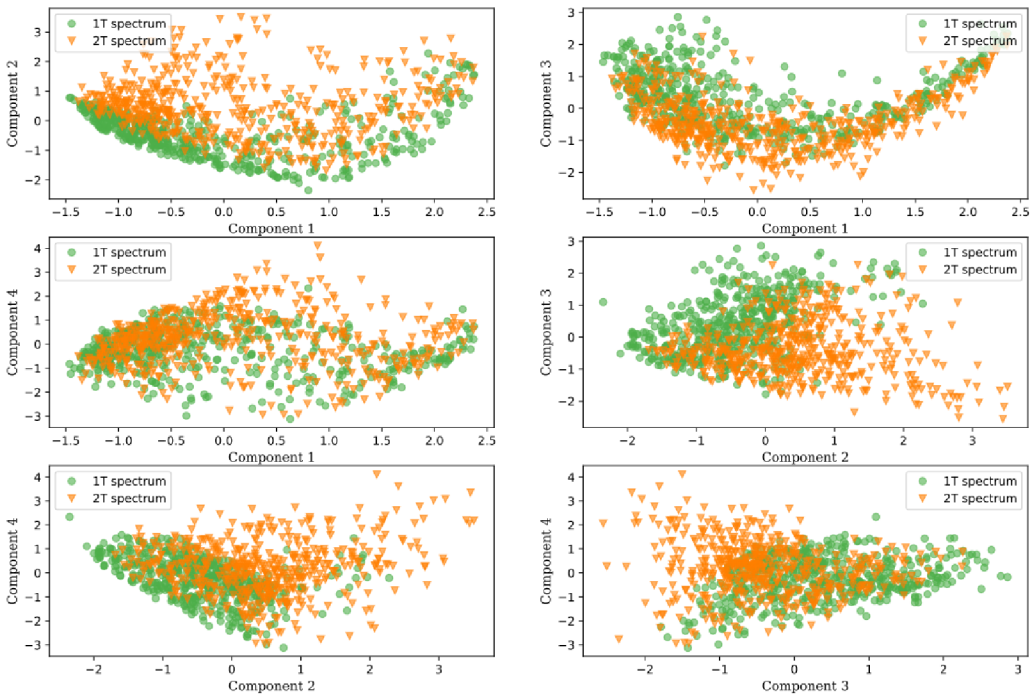

(a) $R^{\min} = 0.1$

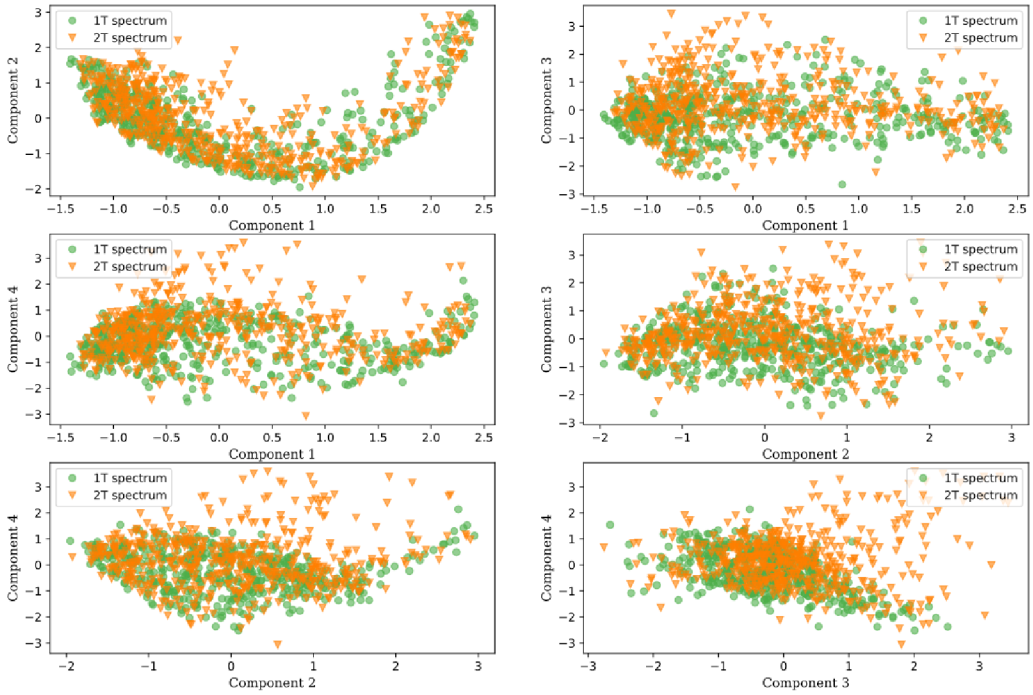

(b) $R^{\min} = 0.001$

Figure B.2: The interdependence of the initial four principal components for 500 single (circle) and double (triangle) temperature spectra of the *Chandra* satellite pertaining models with $N_1^{\min} = 10^{-4}$ for the Virgo Cluster.

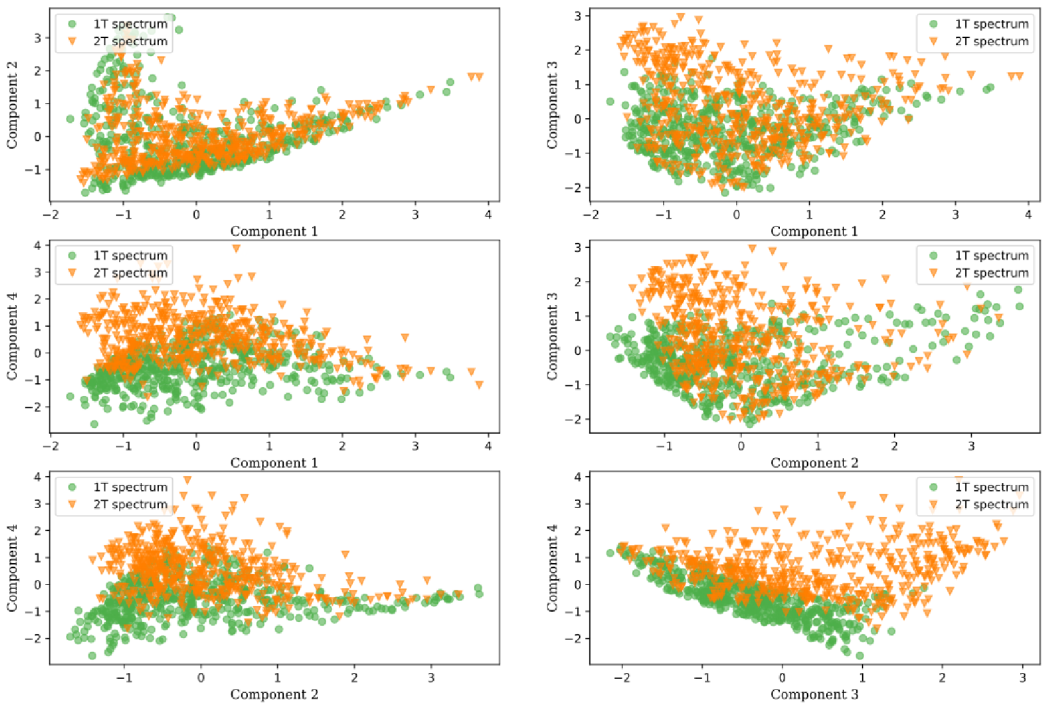

(a) $R^{\min} = 0.1$

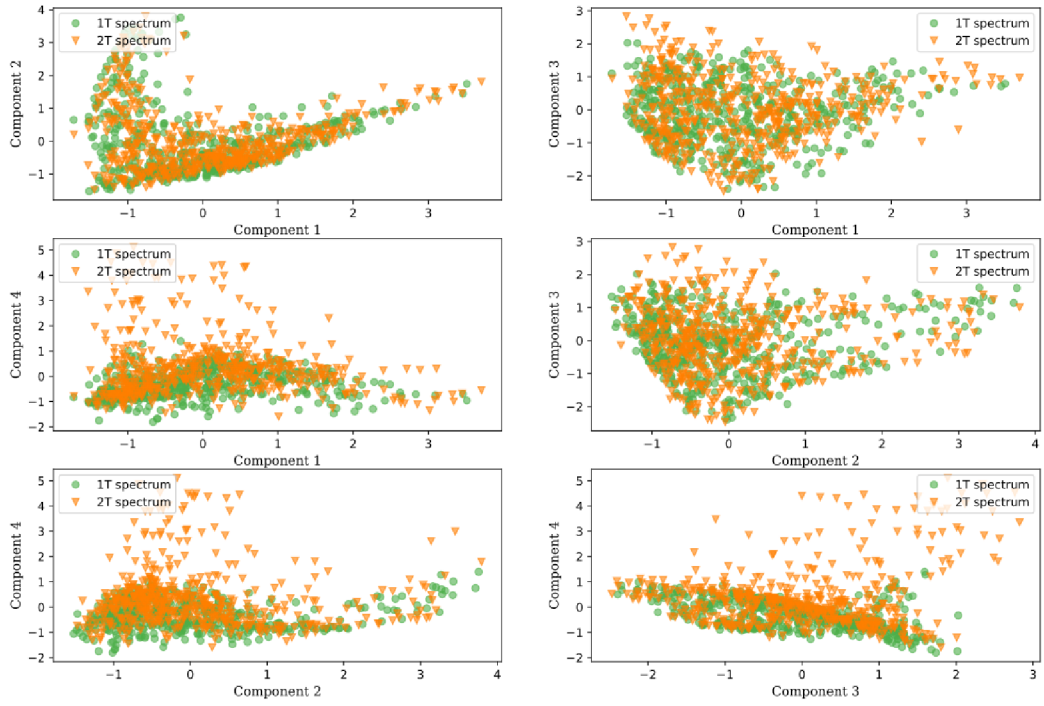

(b) $R^{\min} = 0.001$

Figure B.3: The interdependence of the initial four principal components for 500 single (circle) and double (triangle) temperature spectra of the XRISM satellite models for the Virgo Cluster.

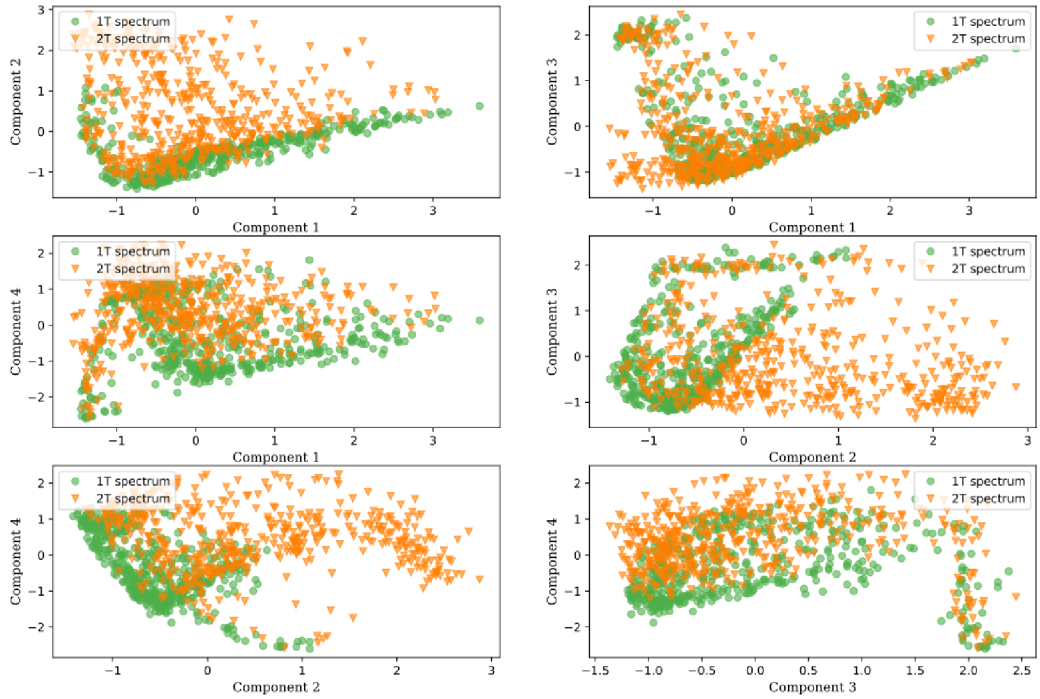

(a) $R^{\min} = 0.1$

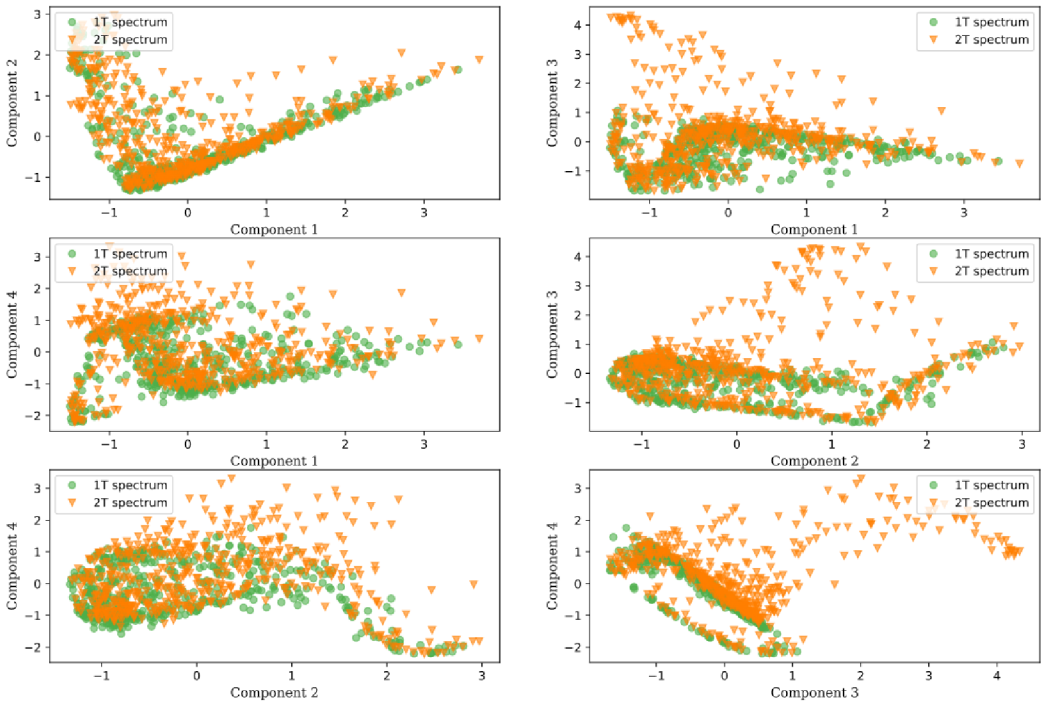

(b) $R^{\min} = 0.001$

Figure B.4: The interdependence of the initial four principal components for 500 single (circle) and double (triangle) temperature spectra of the *Athena* satellite models for the Virgo Cluster.

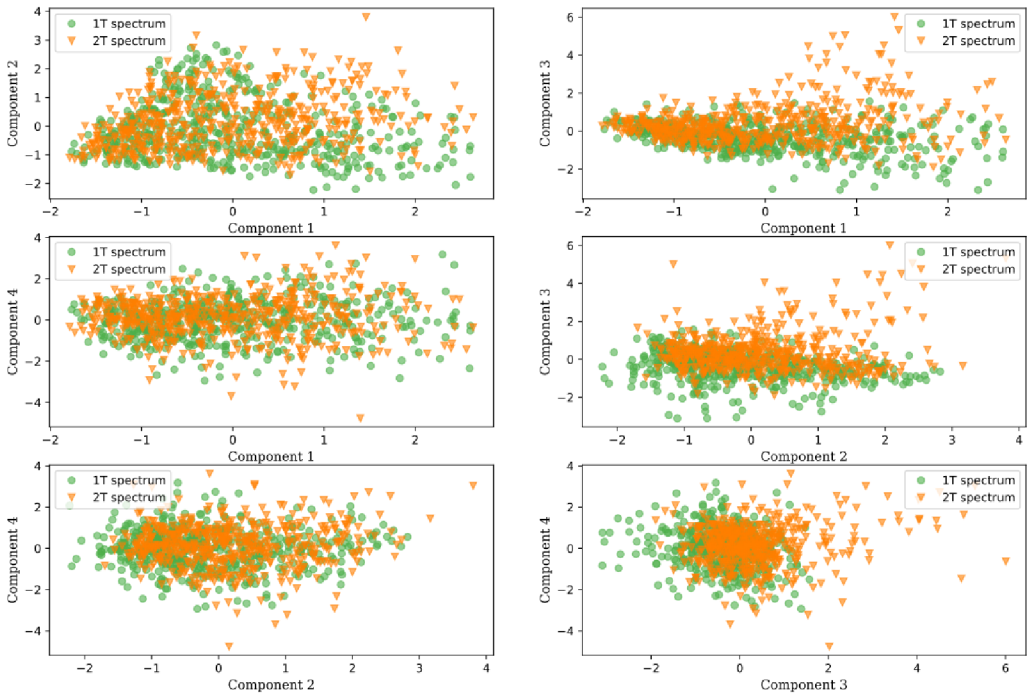

(a) $R^{\min} = 0.1$

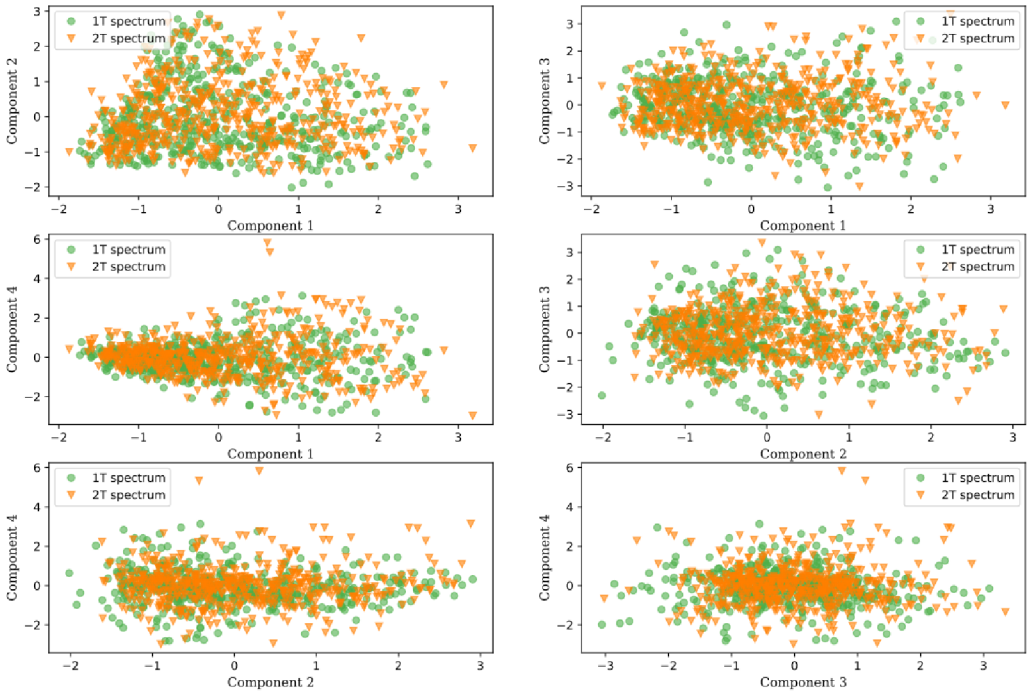

(b) $R^{\min} = 0.001$

Figure B.5: The interdependence of the initial four principal components for 500 single (circle) and double (triangle) temperature spectra of the *Chandra* satellite pertaining models with $N_1^{\min} = 10^{-5}$ for the Perseus Cluster.

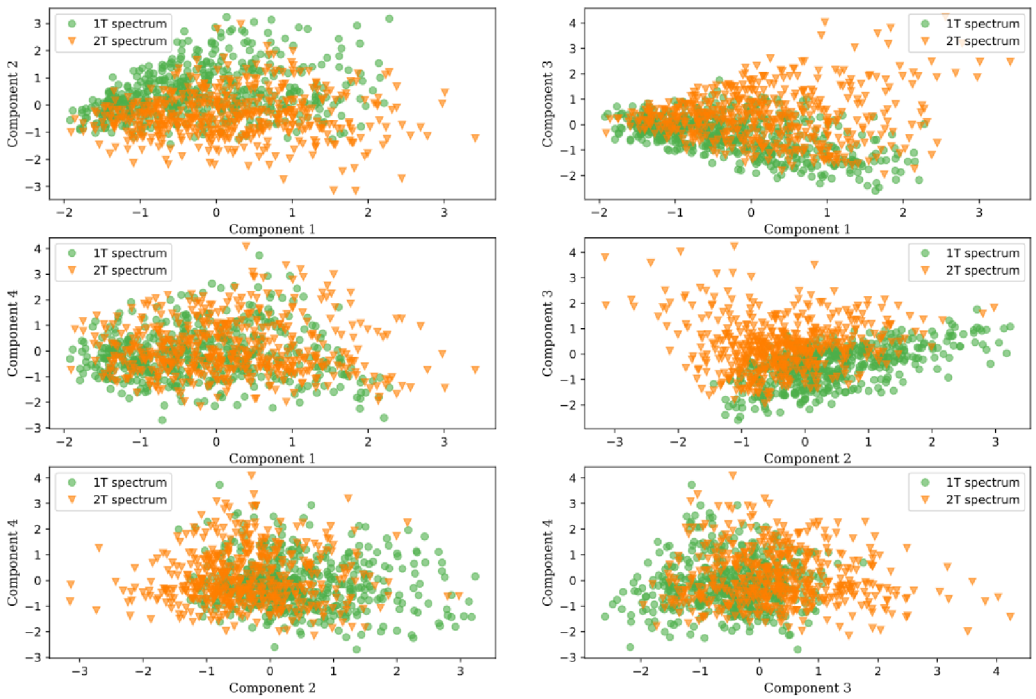

(a) $R^{\min} = 0.1$

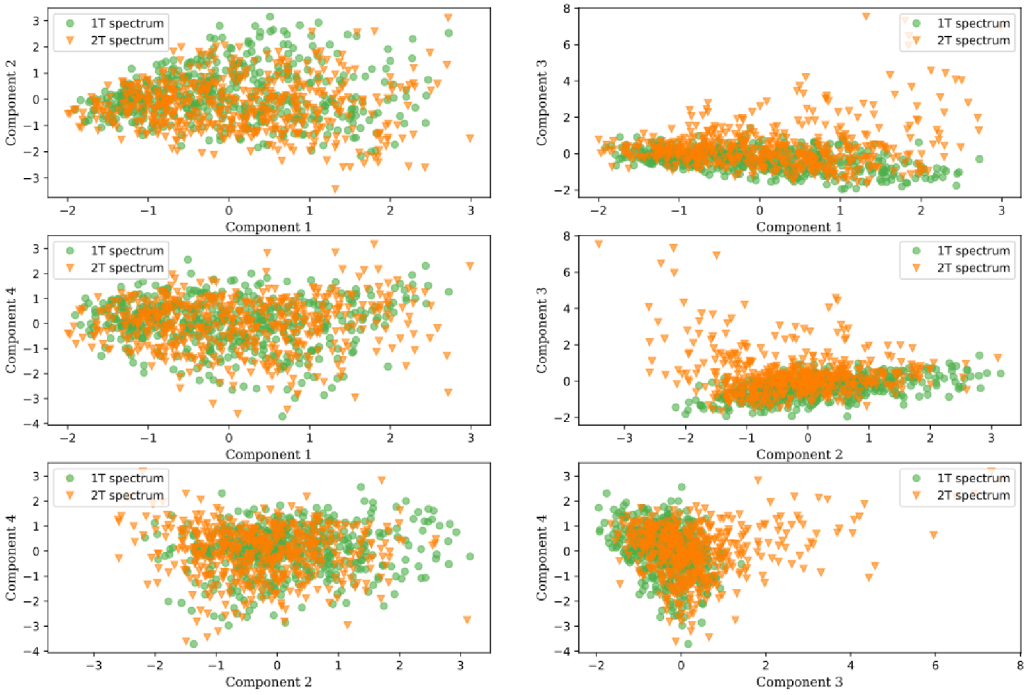

(b) $R^{\min} = 0.001$

Figure B.6: The interdependence of the initial four principal components for 500 single (circle) and double (triangle) temperature spectra of the *Chandra* satellite pertaining models with $N_1^{\min} = 10^{-4}$ for the Perseus Cluster.

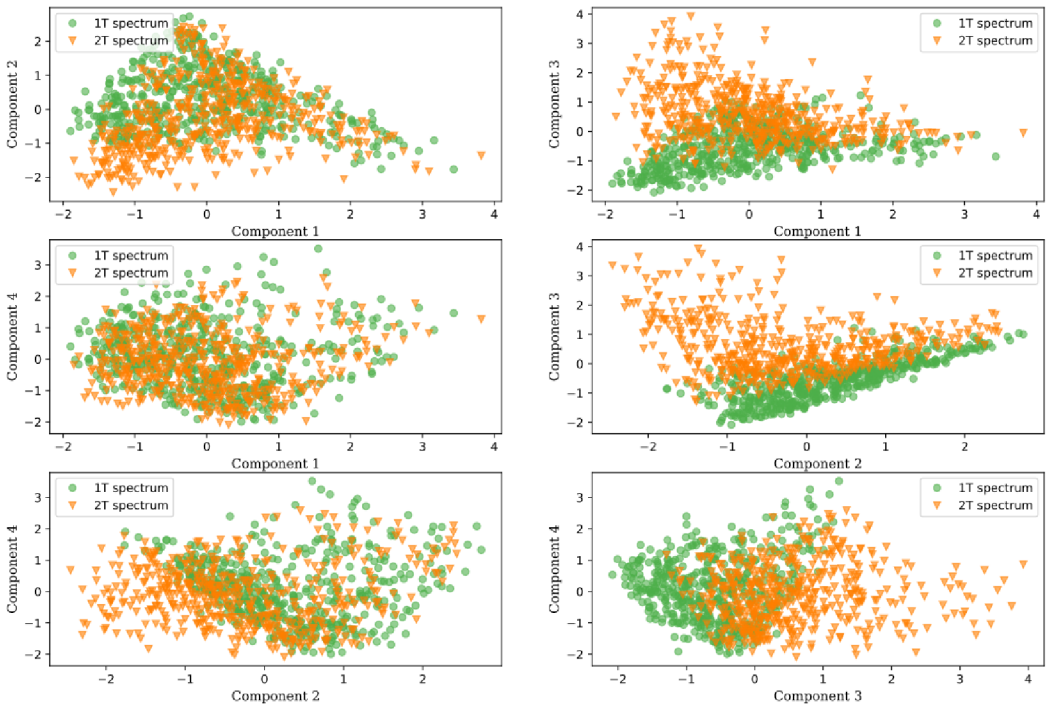

(a) $R^{\min} = 0.1$

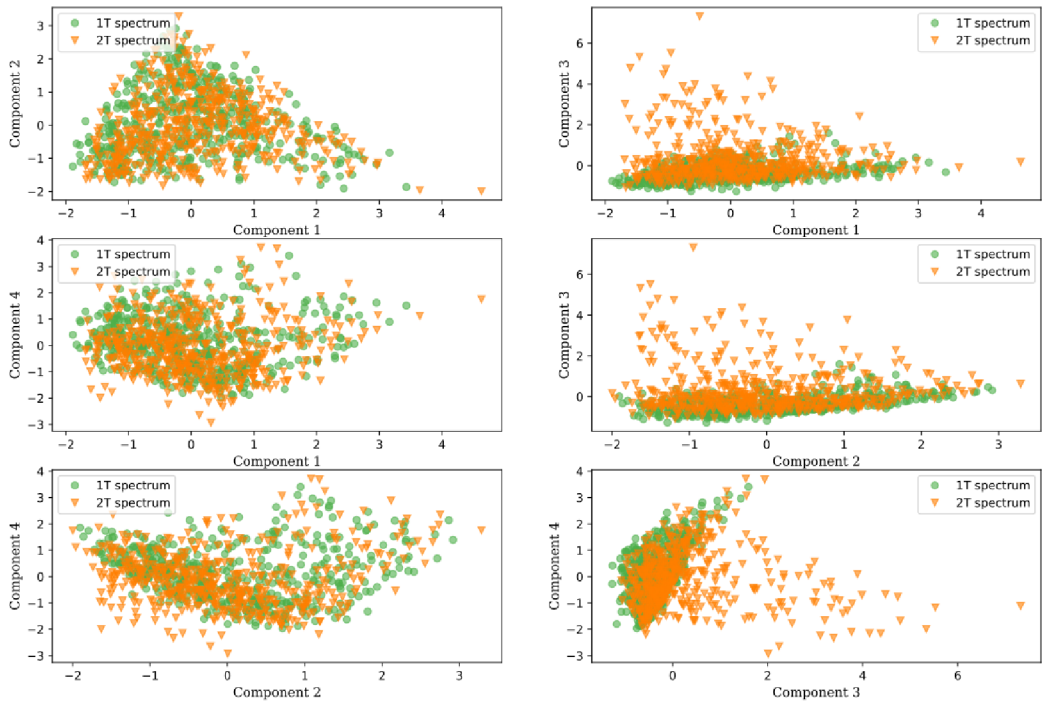

(b) $R^{\min} = 0.001$

Figure B.7: The interdependence of the initial four principal components for 500 single (circle) and double (triangle) temperature spectra of the XRISM satellite models for the Perseus Cluster.

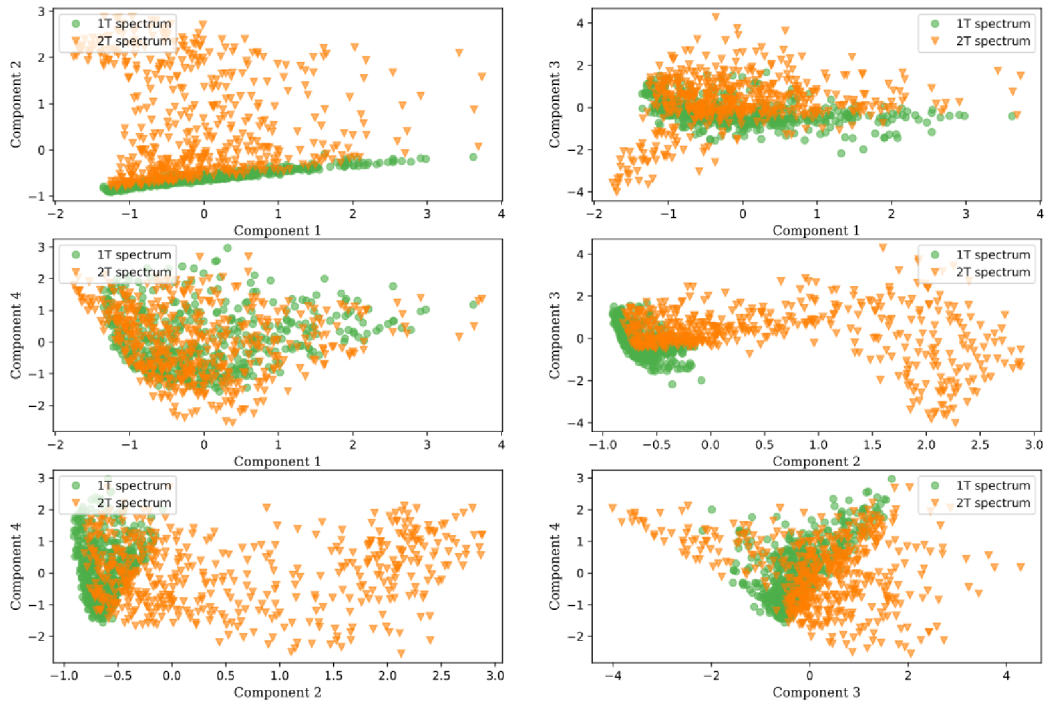

(a) $R^{\min} = 0.1$

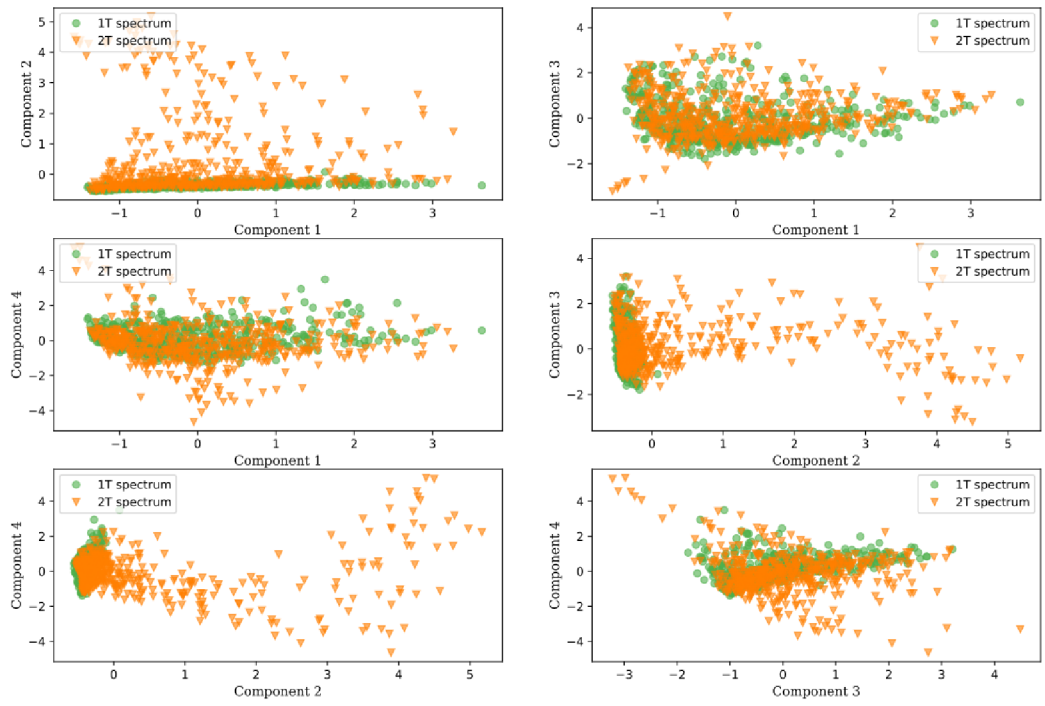

(b) $R^{\min} = 0.001$

Figure B.8: The interdependence of the initial four principal components for 500 single (circle) and double (triangle) temperature spectra of the *Athena* satellite models for the Perseus Cluster.

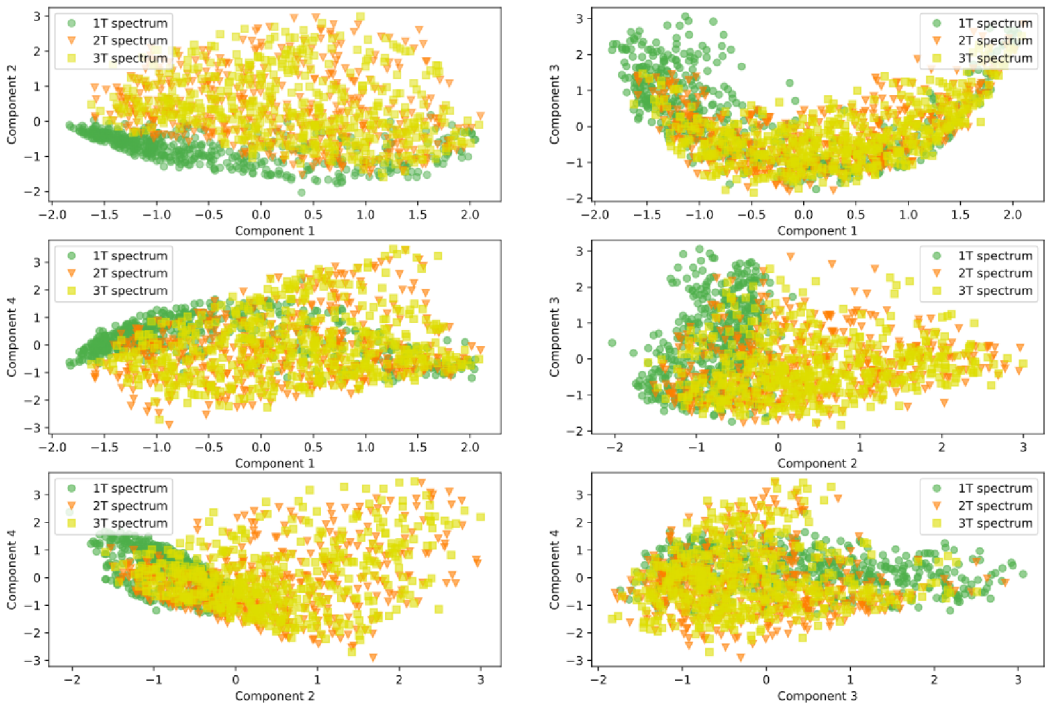

(a) $N_1^{\min} = 10^{-4}$

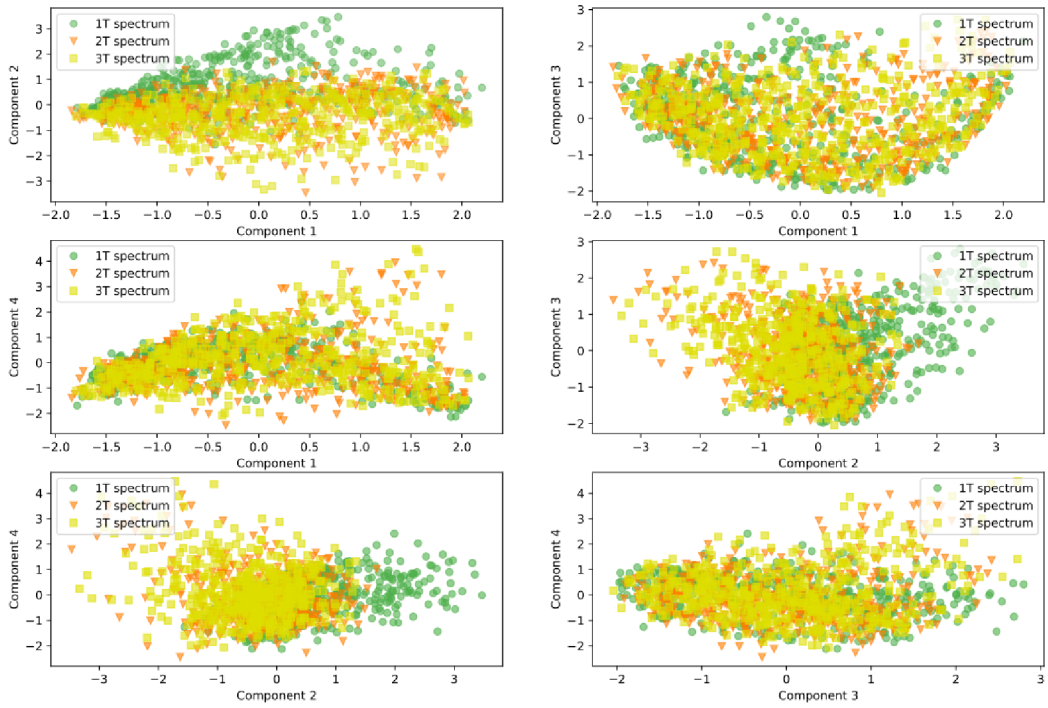

(b) $N_1^{\min} = 10^{-5}$

Figure B.9: The interdependence of the initial 4 principal components for 500 single (circle), double (triangle), and triple (square) temperature spectra of the *Chandra* satellite models for the Virgo cluster.

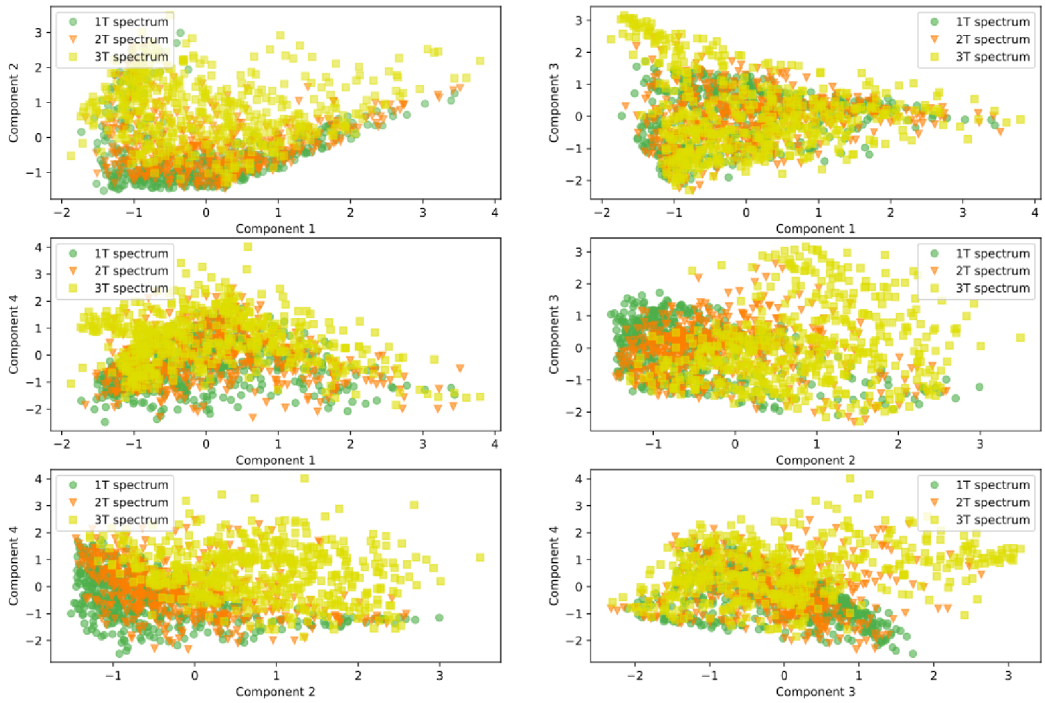

(a) XRISM

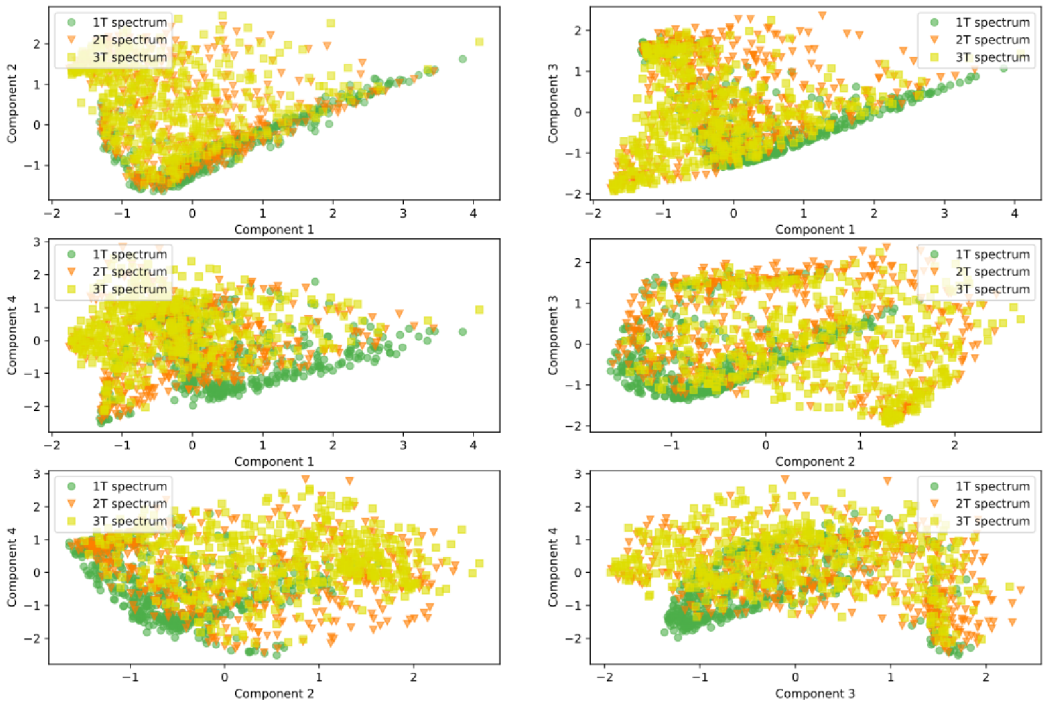

(b) *Athena*

Figure B.10: The interdependence of the initial 4 principal components for 500 single (circle), double (triangle), and triple- (square) temperature spectra of the XRISM and *Athena* satellite models for the Virgo cluster.

C

APENDIX C: INDIVIDUAL PRINCIPAL COMPONENTS & VARIANCE COVERAGE

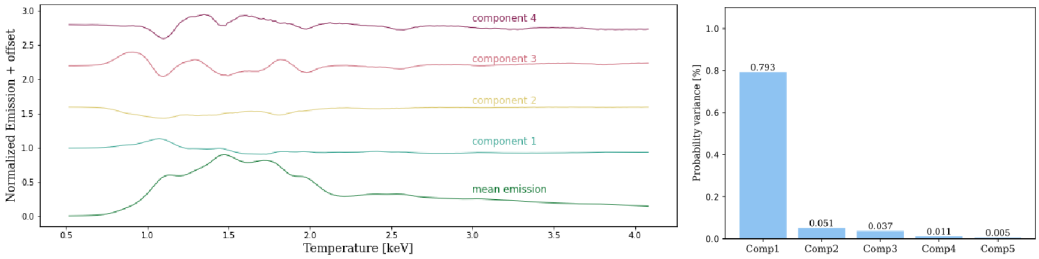

Figure C.1: First few individual components (left) and their variance coverage (right). *Chandra* $N_1^{\min} = 10^{-4}$, $R^{\min} = 0.1$ for Virgo.

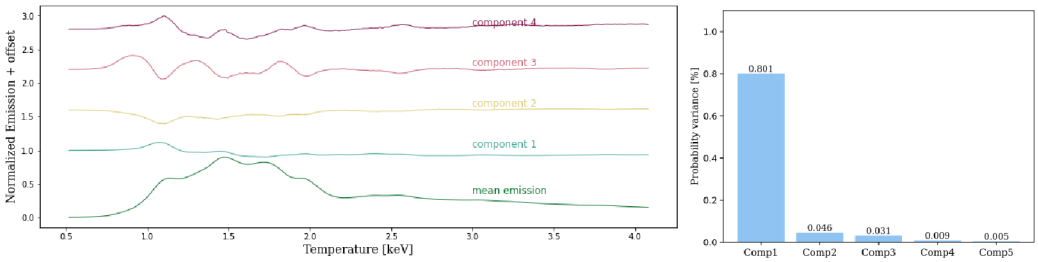

Figure C.2: First few individual components (left) and their variance coverage (right). *Chandra* $N_1^{\min} = 10^{-4}$, $R^{\min} = 0.001$ for Virgo.

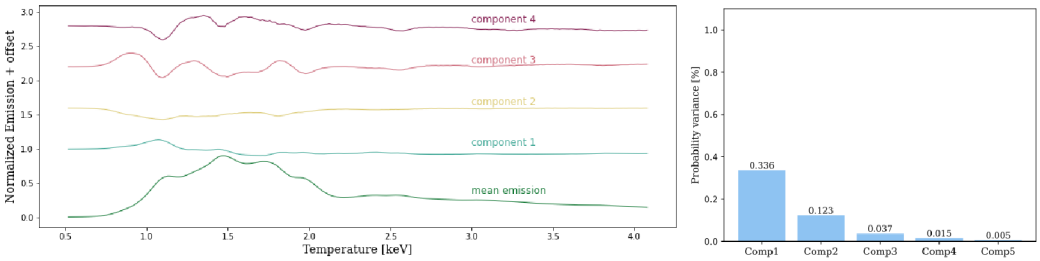

Figure C.3: First few individual components (left) and their variance coverage (right). *Chandra* $N_1^{\min} = 10^{-4}$, $R^{\min} = 0.1$ for Perseus.

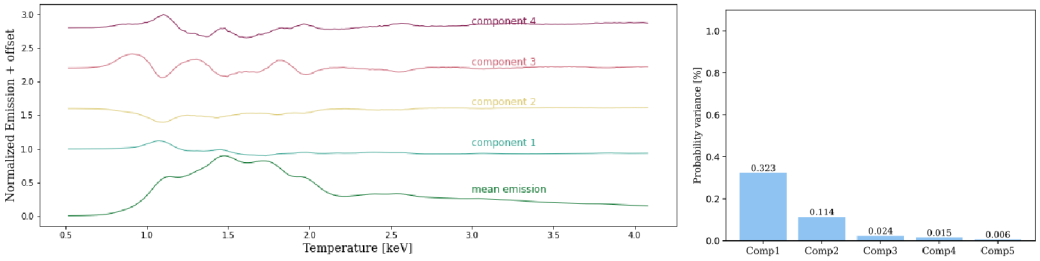

Figure C.4: First few individual components (left) and their variance coverage (right). *Chandra* $N_1^{\min} = 10^{-4}$, $R^{\min} = 0.001$ for Perseus.

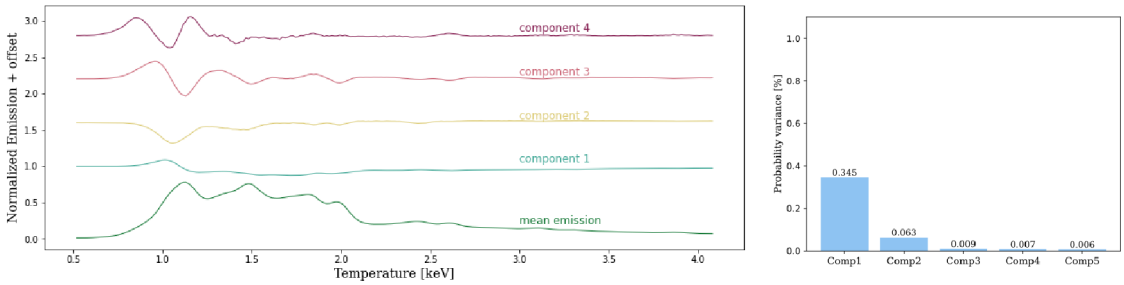

Figure C.5: First few individual components (left) and their variance coverage (right). *Chandra* $N_1^{\min} = 10^{-5}$, $R^{\min} = 0.1$ for Virgo.

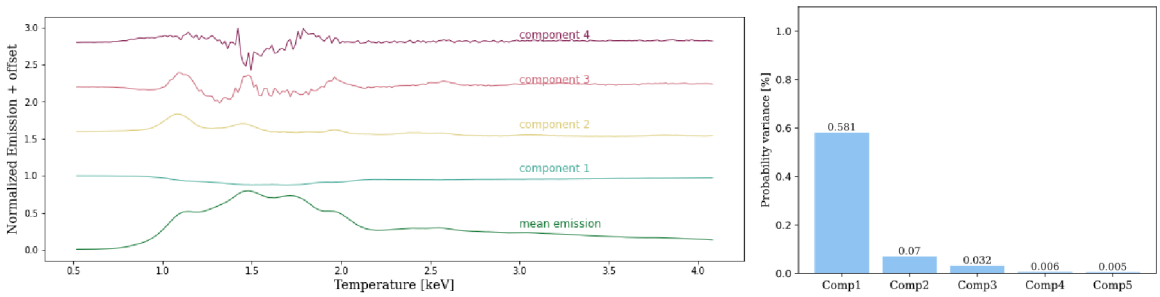

Figure C.6: First few individual components (left) and their variance coverage (right). *Chandra* $N_1^{\min} = 10^{-5}$, $R^{\min} = 0.001$ for Virgo.

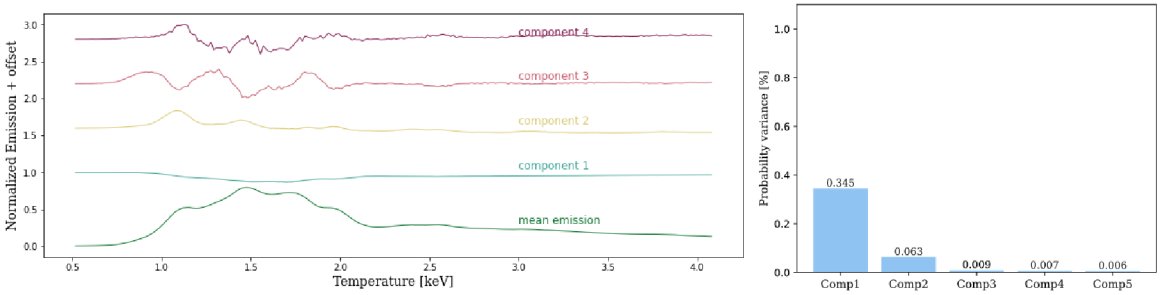

Figure C.7: First few individual components (left) and their variance coverage (right). *Chandra* $N_1^{\min} = 10^{-5}$, $R^{\min} = 0.1$ for Perseus.

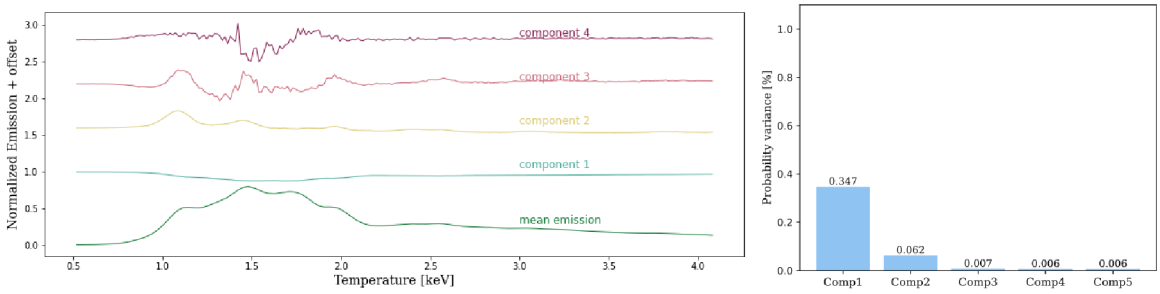

Figure C.8: First few individual components (left) and their variance coverage (right). *Chandra* $N_1^{\min} = 10^{-5}$, $R^{\min} = 0.001$ for Perseus.

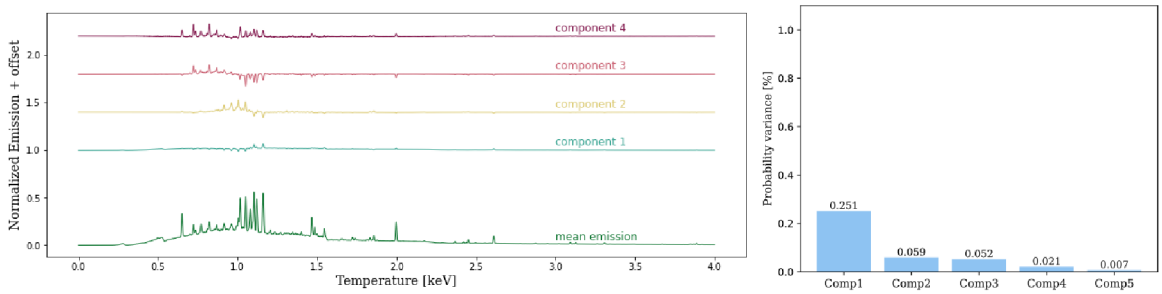

Figure C.9: First few individual components (left) and their variance coverage (right). *XRISM* $N_1^{\min} = 10^{-5}$, $R^{\min} = 0.1$ for Virgo.

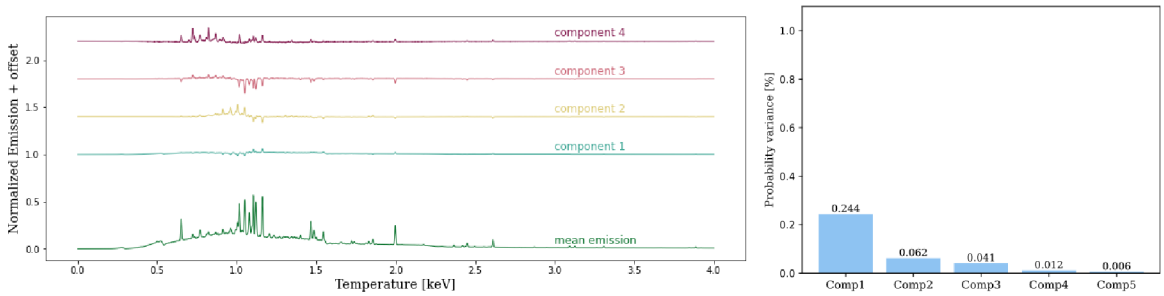

Figure C.10: First few individual components (left) and their variance coverage (right). *XRISM* $N_1^{\min} = 10^{-5}$, $R^{\min} = 0.001$ for Virgo.

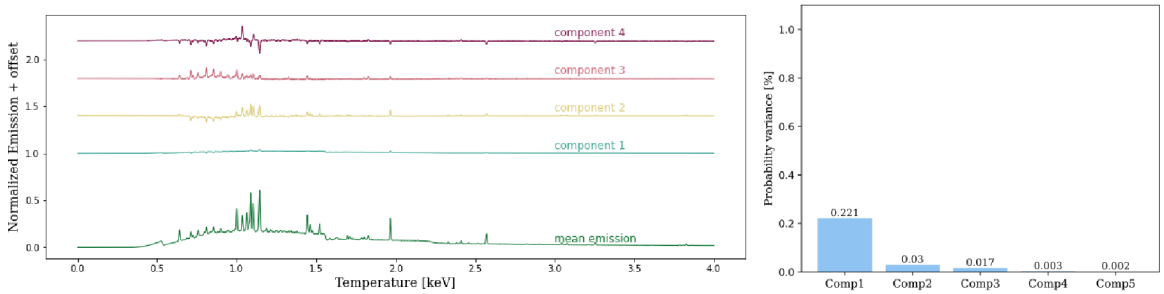

Figure C.11: First few individual components (left) and their variance coverage (right). *XRISM* $N_1^{\min} = 10^{-5}$, $R^{\min} = 0.1$ for Perseus.

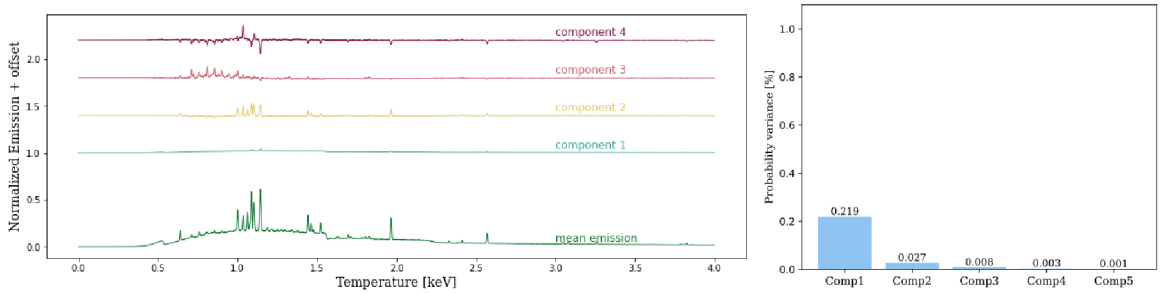

Figure C.12: First few individual components (left) and their variance coverage (right). *XRISM* $N_1^{\min} = 10^{-5}$, $R^{\min} = 0.001$ for Perseus.

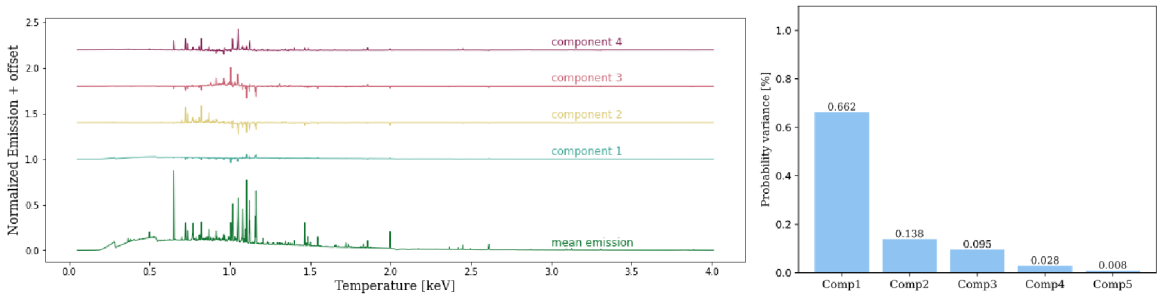

Figure C.13: First few individual components (left) and their variance coverage (right). *Athena* $N_1^{\min} = 10^{-5}$, $R^{\min} = 0.1$ for Virgo.

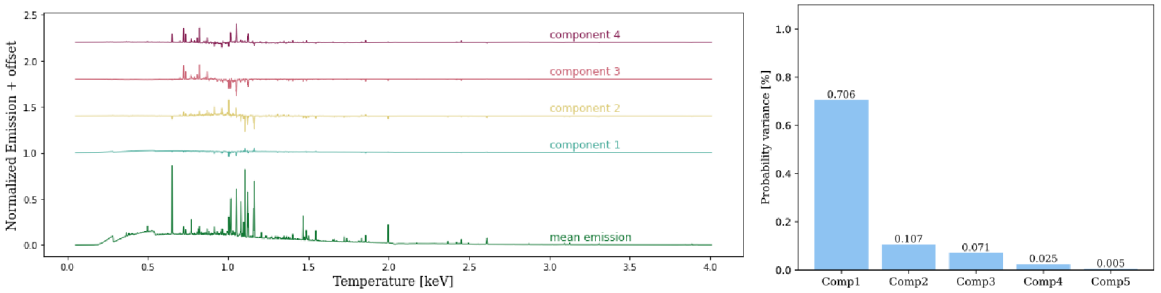

Figure C.14: First few individual components (left) and their variance coverage (right). *Athena* $N_1^{\min} = 10^{-5}$, $R^{\min} = 0.001$ for Virgo.

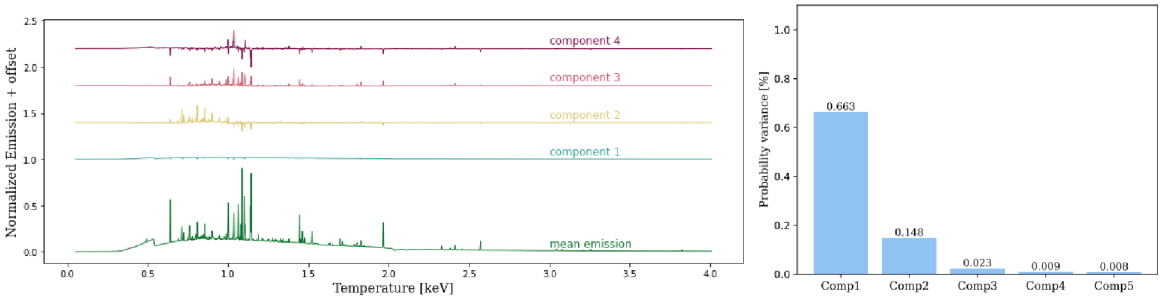

Figure C.15: First few individual components (left) and their variance coverage (right). *Athena* $N_1^{\min} = 10^{-5}$, $R^{\min} = 0.1$ for Perseus.

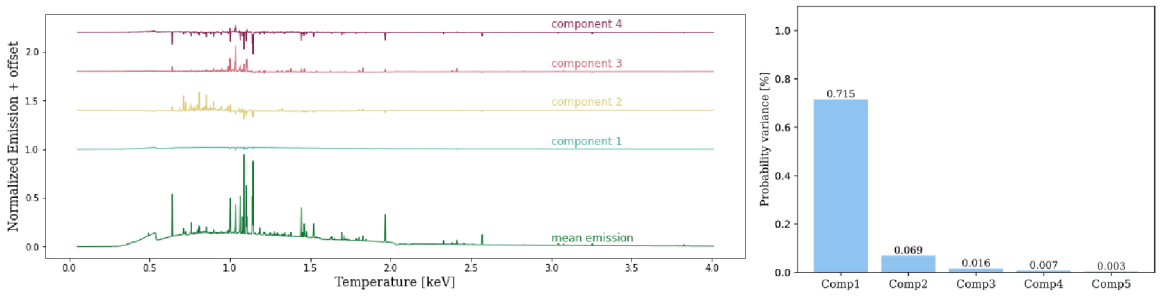

Figure C.16: First few individual components (left) and their variance coverage (right). *Athena* $N_1^{\min} = 10^{-5}$, $R^{\min} = 0.001$ for Perseus.

D

APENDIX D: RF MODEL PREDICTIONS ON SELECTED REGIONS

The correct and incorrect predictions of the *Chandra* RF models on selected regions from real observations. The Y-axis labels correspond to individual regions, while the X-axis values represent parameter R_{min} of models, with the index values a, b corresponding to N_1^{min} ($a = 10^{-4}$ and $b = 10^{-5}$). False model predictions are marked by the symbol 'x' in the cells.

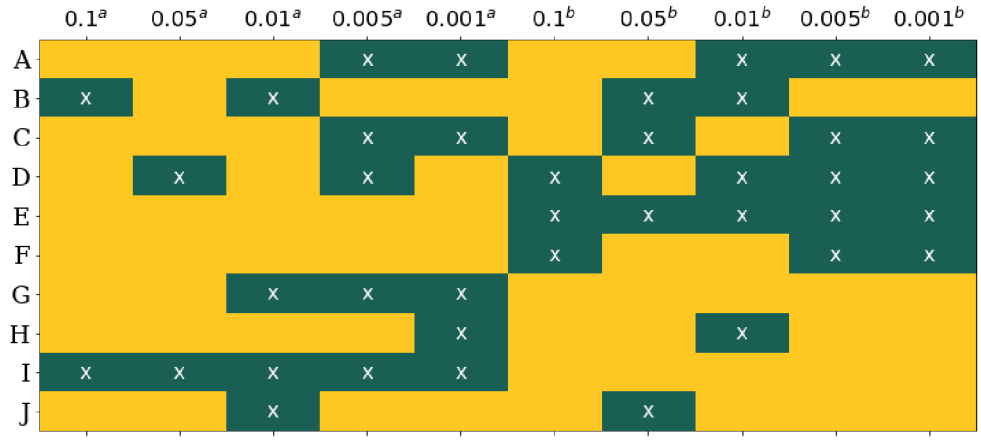

Figure D.1: Visualization of the correct (empty yellow cells) and incorrect (green cells with symbol ´x') classification of *Chandra* models on real spectra for Virgo cluster.

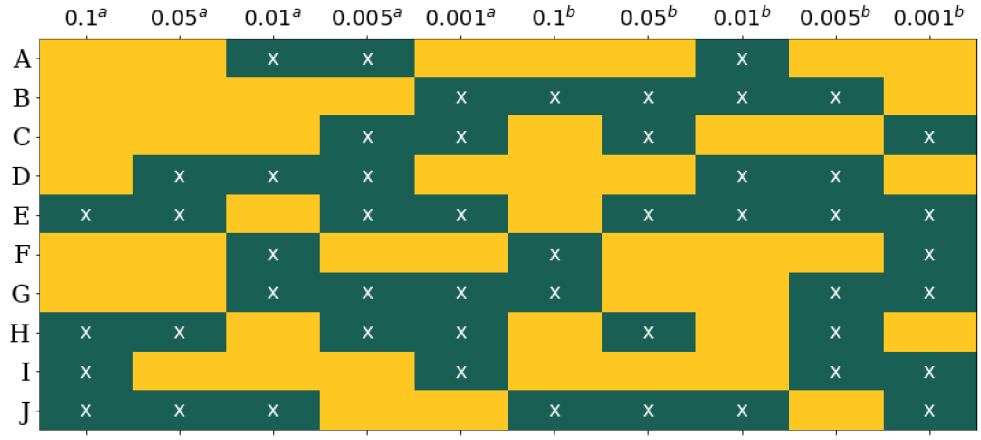

Figure D.2: Visualization of the correct (empty yellow cells) and incorrect (green cells with symbol ´x') classification of *Chandra* models on real spectra for Perseus cluster.

BIBLIOGRAPHY

[1]Arnaud K. A., "Xspec: the first ten years," in Astronomical data analysis software and systems v, Vol. 101, edited by G. H. Jacoby and J. Barnes, Astronomical Society of the Pacific Conference Series (1996), p. 17.

[2]Arnaud K. A., *Xspec user's guide: version 12.11.1*, HEASARC Astrophysics Science Division, NASA Goddard Space Flight Center (1996-2021).

[3]Balucinska-Church M. and McCammon D., "Photoelectric absorption cross sections with variable abundances," Astrophysical Journal **400**, 699 (1992).

[4]Barnett R. M., *Principal component analysis*, 2017.

[5]Belabbas M. A. and Wolfe P. J., "Spectral methods in machine learning and new strategies for very large datasets," PNAS **106**, 369–374 (2021).

[6]Belgiu M. and Drăguţ L., "Random forest in remote sensing: a review of applications and future directions," ISPRS Journal of Photogrammetry and Remote Sensing **114**, 24–31 (2016).

[7]Biau G., "Analysis of a random forests model," J. Mach. Learn. Res. **13**, 1063–1095 (2012).

[8]Böhringer H. and Werner N., "X-ray spectroscopy of galaxy clusters: studying astrophysical processes in the largest celestial laboratories," Astronomy and Astrophysics Reviews **18**, 127–196 (2010).

[9]Bonamente M., Lieu R., Joy M. K., and Nevalainen J. H., "The soft x-ray emission in a large sample of galaxy clusters with the rosat position sensitive proportional counter," The Astrophysical Journal **576**, 688 (2002).

[10]Breiman L., "Random forests," Machine Learning **45**, 5–32 (2001).

[11]Brickhouse N. S. and Smith R. K., "Spectral modeling with apec," Highlights of Astronomy **13**, 651–652 (2005).

[12]Brickhouse N. S., Smith R. K., Raymond J. C., and Liedahl D. A., "The astrophysical plasma emission code," in Aas/high energy astrophysics division #5, Vol. 5, AAS/High Energy Astrophysics Division (Oct. 2000), p. 27.01.

[13]Bro R. and Smilde A. K., "Principal component analysis," Anal. Methods **6**, 2812–2831 (2014).

[14]Burke B.E., Gregory J.A., Bautz M.W., Prigozhin G.Y., Kissel S.E., Kosicki B.B., Loomis A.H., and Young D.J., "Soft-x-ray ccd imagers for axaf," IEEE Transactions on Electron Devices **44**, 1633–1642 (1997).

[15]Böhringer H., "Galaxy clusters as probes for matter in the universe.," Space Science Reviews **100**, 49–60 (2002).

[16]Böhringer H., Pratt G. W., Finoguenov A., and Schuecker P., *Heating versus cooling in galaxies and clusters of galaxies* (2007).

[17]CXC, *Acis: advanced ccd imaging spectrometer*, (2023) https://cxc.harvard.edu/proposer/POG/html/chap6.html#tth_sEc6.2.2, (accessed: 17.03.2023).

[18]CXC, *Acis cycle 25 aimpoint and off-axis rmfs/arfs*, (2022) https://cxc.cfa.harvard.edu/caldb/prop_plan/imaging/index.html, (accessed: 09.10.2022).

[19]CXC, *Sherpa*, (2022) https://cxc.cfa.harvard.edu/sherpa/, (accessed: 09.11.2022).

[20]Calzadilla M. S., McDonald M., Donahue M., McNamara B. R., and ..., "Testing the limits of AGN feedback and the onset of thermal instability in the most rapidly star-forming brightest cluster galaxies," The Astrophysical Journal **940**, 140 (2022).

[21]Castellani F., Beaumont S., and ..., "A 50 mk test bench for demonstration of the readout chain of athena/x-ifu," in Space telescopes and instrumentation 2022: ultraviolet to gamma ray, Vol. 12181, edited by J.-W. A. den Herder, S. Nikzad, and K. Nakazawa, Society of Photo-Optical Instrumentation Engineers (SPIE) Conference Series (Aug. 2022), p. 1218144.

[22]Cavagnolo K. W., D. and Voit G. M., and Sun M., "Intracluster medium entropy profiles for a chandra archival sample of galaxy clusters," The Astrophysical Journal Supplement Series **182**, 12–32 (2009).

[23]Chartas G., Garmire G. P., Nousek J. A., Koch S., Kissel S. E., Prigozhin G. Y., and Bautz M. W., "Optimizing the acis effective area and energy resolution," in X-ray optics, instruments, and missions, Vol. 3444, edited by R. B. Hoover and A. B. Walker, Society of Photo-Optical Instrumentation Engineers (SPIE) Conference Series (Nov. 1998), pp. 258–266.

[24]Connor T., Donahue M., Sun M., Hoekstra H., Mahdavi A., Conselice Ch. J., and McNamara B., "Scaling relations and x-ray properties of moderate-luminosity galaxy clusters from $0.3 < z < 0.6$ with xmm-newton," apj **794**, 48, 48 (2014).

[25]Das H. K., Houdhury P. P., and Sharma, P., "Shatter or not: role of temperature and metallicity in the evolution of thermal instability," Monthly Notices of the Royal Astronomical Society **502**, 4935–4952 (2021).

[26]Dekel A. and Ostriker J.P., *Formation of structure in the universe* (1999).

[27]Ettori S., Tozzi P., Borgani S., and Rosat P., "Scaling laws in x-ray galaxy clusters at redshift between 0.4 and 1.3*," Astronomy & Astrophysics **417**, 13–27 (2004).

[28]Ezoe Y., Ishisaki Y., Fujimoto R., Takei Y., and The Xrism Resolve Team, "Cooling system for the resolve onboard xrism," Cryogenics **108**, 103016, 103016 (2020).

[29]Ezoe Y., Ohashi T., and Mitsuda K., "High-resolution x-ray spectroscopy of astrophysical plasmas with x-ray microcalorimeters," Reviews of Modern Plasma Physics **5**, 4, 4 (2021).

[30]Fabian A. C., "Cooling flows in clusters of galaxies," Annual review of astronomy and astrophysics **32**, 277–318 (1994).

[31]Fabian A. C., Ferland G. J., Sanders J. S., McNamara B. R., Pinto C., and Walker S. A., "Hidden cooling flows in clusters of galaxies," Monthly Notices of the Royal Astronomical Society **515**, 3336–3345 (2022).

[32]Fabian A. C., Hu E. M., Cowie L. L., and Grindlay J., "The distribution and morphology of x-ray emitting gas in the core of the perseus cluster," Astrophysical Journal **248**, 47–54 (1981).

[33]Fabian A. C., Nulsen P. E. J., and Canizares C. R., "Cooling flows in clusters of galaxies," Nature **310**, 733–740 (1984).

[34]Fabian A. C. and Ross R. R., "X-ray reflection," Space Science Reviews **157**, 167–176 (2010).

[35]Folkes S., Ronen S., Price I., Lahav O., M. Colless, Maddox S., and ..., "The 2df galaxy redshift survey: spectral types and luminosity functions," Monthly Notices of the Royal Astronomical Society **308**, 459–472 (1999).

[36]Foster A. and Smith R. K., "Atomdb: the atomic database for x-ray spectroscopy," Journal of Astrophysics and Astronomy **38**, 33–51 (2017).

[37]Frank K. A., Peterson J. R., Andersson K., Fabian A. C., and Sanders J. S., "Characterization of intracluster medium temperature distribution of 62 galaxy clusters with xmm-newton," The Astrophysical Journal **764**, 46 (2013).

[38]Fujita Y., Cen R., and Zhuravleva I., "Non-steady heating of cool cores of galaxy clusters by ubiquitous turbulence and agn," Monthly Notices of the Royal Astronomical Society **494**, 5507–5519 (2020).

[39]Garmire G. P., Bautz M. W., Ford P. G., Nousek J. A., and Ricker Jr. G. R., "Advanced ccd imaging spectrometer (acis) instrument on the chandra x-ray observatory," in X-ray and gamma-ray telescopes and instruments for astronomy, Vol. 4851, edited by J. E. Truemper and H. D. Tananbaum (International Society for Optics and Photonics, 2003), pp. 28 –44.

[40]Giles P. A., Maughan B. J., Pacaud F., Lieu M., Clerc N., Pierre M., Adami C., Chiappetti L., Démoclés J., Ettori S., Le Févre J. P., Ponman T., Sadibekova T., Smith G. P., Willis J. P., and Ziparo F., "The xxl survey - iii. luminosity-temperature relation of the bright cluster sample," Astronomy & Astrophysics **592**, A3 (2016).

[41]Goldman S. R., Sankrit R., Wolthuis N., Garner S., Gualdoni C., and Bolzoni S., "Sudden dimming of the symbiotic mira hm sge," Research Notes of the American Astronomical Society **6**, 159, 159 (2022).

[42]Gorenstein P., Bjorkholm P., Harris B., and Harnden F. R. Jr., "Soft x-ray flux of the coma cluster of galaxies," Astrophysical Journal Letters **183**, L57 (1973).

[43]Gottardi L. and Smith S., *Transition-edge sensors for cryogenic x-ray imaging spectrometers*, 2022.

[44]Gursky H., Kellogg E., Murray S., Leong C., Tananbaum H., and Giacconi R., "A strong x-ray source in the coma cluster observed by uhuru," Astrophysical Journal Letters **167**, L81 (1971).

[45]Haghighi M. H. Z., Afshordi N., and Khosroshahi H. G., "Cooling, heating flows in galaxy clusters: turbulent heating, spectral modeling, and cooling efficiency," The Astrophysical Journal **884**, 47 (2019).

[46]Harvard-Smithsonian Center for Astrophysics, *Chaser - chandra archive and source catalog query engine*, 2021.

[47]Hastie T., Tibshirani R., and Friedman J., *The elements of statistical learning, Random Forests* (2009).

[48]Heuer K., Foster A. R., and Smith R., "Spectral implications of atomic uncertainties in optically thin hot plasmas," Astrophysical Journal **908**, 3, 3 (2021).

[49]Hitomi Collaboration, Aharonian F., Akamatsu H., Akimoto F., Allen S. W., and ..., "Atmospheric gas dynamics in the perseus cluster observed with hitomi," Publications of the Astronomical Society of Japan **70**, `10.1093/pasj/psx138` (2018).

[50]Hitomi Collaboration, Aharonian F., Akamatusu H., Akimoto F., Allen S. W., and ..., "Temperature structure in the perseus cluster core observed with hitomi," Publications of the Astronomical Society of Japan **70**, 11 (2018).

[51]Ichinohe Y., Simionescu A., Werner N., Fabian A. C., and Takahashi T., "Substructures associated with the sloshing cold front in the perseus cluster," Monthly Notices of Royal Astronomical Society **483**, 1744–1753 (2019).

[52]Irwin J. A., Athey A. E., and Bregman J. N., "X-ray spectral properties of low-mass x-ray binaries in nearby galaxies," Astrophysical Journal **587**, 356–366 (2003).

[53]Ishisaki Y., Ezoe Y., Yamada S., Ichinohe Y., and ..., "Resolve instrument on x-ray astronomy recovery mission (xarm)," Journal of Low Temperature Physics **193**, 991–995 (2018).

[54]Ishisaki Y., Kelley R. L., and ..., "Status of resolve instrument onboard x-ray imaging and spectroscopy mission (xrism)," in Space telescopes and instrumentation 2022: ultraviolet to gamma ray, Vol. 12181, edited by J.-W. A. den Herder, S. Nikzad, and K. Nakazawa, Society of Photo-Optical Instrumentation Engineers (SPIE) Conference Series (Aug. 2022), 121811S.

[55]JAXA, *Mission instruments*, (2018) `https://xrism.isas.jaxa.jp/en/technology/detail_02/`, (accessed: 26.03.2023).

[56]JAXA, *Response & background files for point-source simulations*, (2022) https://xrism.isas.jaxa.jp/research/proposer/obsplan/response/index.html, (accessed: 15.10.2022).

[57]Jennings F., Beckmann R. S., Sijacki D., and Dubois Y., "Shattering and growth of cold clouds in galaxy clusters: the role of radiative cooling, magnetic fields, and thermal conduction," Monthly Notices of the Royal Astronomical Society **518**, 5215–5235 (2022).

[58]Jolliffe I. T. and Cadima J., "Principal component analysis: a review and recent developments," Philosophical Transactions of the Royal Society of London Series A **374**, 20150202 (2016).

[59]Kartun-Giles A., Krioukov D., Gleeson J., Moreno Y., and Bianconi G., "Sparse power-law network model for reliable statistical predictions based on sampled data," Entropy **20**, 257 (2018).

[60]Kerby S., Kaur A., Falcone A. D., Eskenasy R., Hancock F., Stroh M. C., Ferrara E. C., Ray P. C., Kennea J. A., and Grove E., "Multiwavelength spectral analysis and neural network classification of counterparts to 4fgl unassociated sources," The Astrophysical Journal **923**, 75 (2021).

[61]Kravtsov A. V. and Borgani S., "Formation of galaxy clusters," Annual Review of Astronomy and Astrophysics **50**, 353–409 (2012).

[62]Larmor J., "Lxiii. on the theory of the magnetic influence on spectra; and on the radiation from moving ions," The London, Edinburgh, and Dublin Philosophical Magazine and Journal of Science **44**, 503–512 (1897).

[63]Ley F., Zweibel E. G., Riquelme M., Sironi L., Miller D., and Tran A., *A heating mechanism via magnetic pumping in the intracluster medium*, 2022.

[64]Li J., Kastner J. H., Prigozhin G. Y., Schulz N. S., Feigelson E. D., and Getman K. V., "Chandra acis subpixel event repositioning: further refinements and comparison between backside- and frontside-illuminated x-ray ccds," The Astrophysical Journal **610**, 1204 (2004).

[65]Liaw A. and Wiener M., "Classification and regression by randomforest," Forest **23** (2001).

[66]Lindtroth E. and Indelicato P., "Inner shell transitions in heavy atoms," English, in (1993).

[67]Liu H., "X-ray Spectroscopy of Cool Core Galaxy Clusters," PhD thesis (University of Cambridge, 2021).

[68]Liu H., Fabian A. C., and Pinto C., "The inner gas mass-temperature profile in the core of nearby galaxy clusters," Monthly Notices of Royal Astronomical Society **497**, 1256–1262 (2020).

[69]Liu H. and Setiono R., "Chi2: feature selection and discretization of numeric attributes," 10.1109/TAI.1995.479783 (1995).

[70]Lotti S., D'Andrea M., Molendi S., Macculi C., Minervini G., Fioretti V., Laurenza M., Jacquey C., and Piro L., "Review of the particle background of the athena x-IFU instrument," The Astrophysical Journal **909**, 111 (2021).

[71]McDonald M., Benson B. A., Vikhlinin A., Stalder B., Bleem L. E., Haan T., Lin H. W., and ..., "The growth of cool cores and evolution of cooling properties in a sample of 83 galaxy clusters at $0.3 < z < 1.2$ selected from the spitzer survey.," The Astrophysical Journal **774**, 23 (2013).

[72]McNamara B.R. and Nulsen P.E.J., "Heating hot atmospheres with active galactic nuclei," Annual Review of Astronomy and Astrophysics **45**, 117–175 (2007).

[73]Mitchell R. J., Culhane J. L., Davison P. J. N., and Ives J. C., "Ariel 5 observation of the x-ray spectrum of the perseus cluster," English, Monthly Notices of Royal Astronomical Society (1976).

[74]Munari U., Righetti G. L., and Dallaporta S., "Multiple flares caused by mass ejection episodes during the advanced nebular phase of nova scuti 2019," Monthly Notices of the Royal Astronomical Society **516**, 4805–4813 (2022).

[75]Murtagh F. and Heck A., "Principal components analysis," in *Multivariate data analysis* (Springer Netherlands, Dordrecht, 1987), pp. 13–53.

[76]Mushotzky R., Loewenstein M., Arnaud K. A., Tamura T., Fukazawa Y., Matsushita K., Kikuchi K., and Hatsukade I., "Measurement of the elemental abundances in four rich clusters of galaxies. i. observations.," The Astrophysical Journal **466**, 10.1086/177541 (1996).

[77]NASA, *Chandra x-ray observatory*, (2022) https://universe.nasa.gov/resources/219/chandra-x-ray-observatory/, (accessed: 25.03.2023).

[78]NASA, *Xrism (x-ray imaging and spectroscopy mission)*, (2022) https://universe.nasa.gov/resources/250/xrism-x-ray-imaging-and-spectroscopy-mission/, (accessed: 25.03.2023).

[79]NASA, CXC, STSCI, MIT, E-H PENG ET AL, and Science photo library, *Abell 1689 galaxy cluster*, (2022) https://www.sciencephoto.com/media/113866/view/abell-1689-galaxy-cluster-x-ray-image, "(accessed: 18.12.2022)".

[80]Nandra K., Barret D., Barcons X., Fabian A., and ..., *The hot and energetic universe: a white paper presenting the science theme motivating the athena+ mission*, 2013.

[81]Nath B. B. and Roychowdhury S., "Heating of the intracluster medium by quasar outflows," Monthly Notices of the Royal Astronomical Society **333**, 145–155 (2002).

[82]Norman M. L. and Bryan G. L., "Cluster turbulence," in *The radio galaxy messier 87* (Springer Berlin Heidelberg, 1999), pp. 106–115.

[83]Nozawa S., Itoh N., and Kohyama Y., "Relativistic thermal bremsstrahlung gaunt factor for the intracluster plasma," The Astrophysical Journal **507**, 10.1086/306352 (1998).

[84]Ntampaka M., ZuHone J., Eisenstein D., Nagai D., Vikhlinin A., Hernquist L., Marinacci F., Nelson D., Pakmor R., Pillepich A., Torrey P., and Vogelsberger M., "A deep learning approach to galaxy cluster x-ray masses," The Astrophysical Journal **876**, 82 (2019).

[85]Peacock J. A., *Cosmological physics* (1999).

[86]Peterson J. R., Kahn S. M., Paerels F. B. S., Kaastra J. S., Tamura T., Bleeker J. A. M., F. C., and J. J. G., *High resolution x-ray spectroscopic constraints on cooling-flow models*, 2003.

[87]Peterson J.R. and Fabian A.C., "X-ray spectroscopy of cooling clusters," Physics Reports **427**, 1–39 (2006).

[88]PetersonJ. R., Paerels F. B. S., Kaastra J. S., Arnaud M., Reiprich T. H., Fabian A. C., Mushotzky R. F., Jernigan J. G., and Sakelliou I., "X-ray imaging-spectroscopy of abell 1835," Astronomy & Astrophysics **365**, L104–L109 (2001).

[89]Petrosian V. and East W. E., "Heating and acceleration of intracluster medium electrons by turbulence," The Astrophysical Journal **682**, 175–185 (2008).

[90]Plšek T., Werner N., Grossová R., Topinka M., Simionescu A., and Allen S. W., "The relation between accretion rate and jet power in early-type galaxies with thermally unstable hot atmospheres," Monthly Notices of the Royal Astronomical Society **517**, 3682–3710 (2022).

[91]Pratt G. W., Böhringer H., Croston J. H., Arnaud M., Borgani S., Finoguenov A., and Temple R. F., "Temperature profiles of a representative sample of nearby x-ray galaxy clusters," Astronomy & Astrophysics **461**, 71–80 (2007).

[92]Rafferty D. A., McNamara B. R., Nulsen P. E. J., and Wise M. W., "The feedback-regulated growth of black holes and bulges through gas accretion and starbursts in cluster central dominant galaxies," The Astrophysical Journal **652**, 216–231 (2006).

[93]Rhea C., Hlavacek-Larrondo J., Perreault-Levasseur L., Gendron-Marsolais M. L., and Kraft R., "A novel machine learning approach to disentangle multitemperature regions in galaxy clusters," The Astronomical Journal **160**, 202 (2020).

[94]Rhea C., Rousseau-Nepton L., Prunet S., Prasow-É mond M., Hlavacek-Larrondo J., Asari N. V., Grasha K., and Perreault-Levasseur L., "A machine-learning approach to integral field unit spectroscopy observations. II. h ii region line ratios," The Astrophysical Journal **910**, 129 (2021).

[95]Ruszkowski M. and Begelman M. C., "Heating, conduction, and minimum temperatures in cooling flows," The Astrophysical Journal **581**, 223–228 (2002).

[96]Sanders J. S. and Fabian A. C., "A deeper x-ray study of the core of the perseus galaxy cluster: the power of sound waves and the distribution of metals and cosmic rays," Monthly Notices of the Royal Astronomical Society **381**, 1381–1399 (2007).

[97]Sanderson A. J. R., Ponman T. J., and O'Sullivan E., "A statistically selected chandra sample of 20 galaxy clusters - i. temperature and cooling time profiles," English, Monthly Notices of the Royal Astronomical Society (2006).

[98]Sarazin C. L., "X-ray emission from clusters of galaxies," Reviews of Modern Physics **58**, 1–115 (1986).

[99]Sarazin, C.L., "Introduction to cluster cooling cores," in, edited by Böhringer H., Pratt G.W., Finoguenov A., and Schuecker P. (2007), pp. 3–12.

[100]Sato K., Uchida Y., and Ishikawa K., *Hitomi/xrism micro-calorimeter*, 2023.

[101]Shlens J., *A tutorial on principal component analysis*, 2014.

[102]Simionescu A., Werner N., Mantz A., Allen S. W., and Urban O., "Witnessing the growth of the nearest galaxy cluster: thermodynamics of the virgo cluster outskirts," Monthly Notices of the Royal Astronomical Society **469**, 1476–1495 (2017).

[103]Sparke L. S. S., *Galaxies in the universe: an introduction* (2007).

[104]Tashiro M., Maejima H., Toda K., and ..., "Status of x-ray imaging and spectroscopy mission (xrism)," in Space telescopes and instrumentation 2020: ultraviolet to gamma ray, Vol. 11444, edited by J.-W. A. den Herder, S. Nikzad, and K. Nakazawa (International Society for Optics and Photonics, 2020), p. 1144422.

[105]Taylor G. B., Gugliucci N. E., Fabian A. C., Sanders J. S., Gentile G., and Allen S. W., "Magnetic fields in the centre of the perseus cluster," Monthly Notices of the Royal Astronomical Society **368**, 1500–1506 (2006).

[106]Ubertosi F., Gitti M., Brighenti F., McDonald M., Nulsen P., Donahue M., Brunetti G., Randall S., Gaspari M., Ettori S., Calzadilla M., Ignesti A., Feretti L., and Blanton E. L., *Multiple shock fronts in rbs 797: the chandra window on shock heating in galaxy clusters*, 2022.

[107]Urdampilleta I., Mernier F., Kaastra J. S., Simionescu A., de Plaa J., Kara S., and Ercan E. N., "Iron abundance distribution in the hot gas of merging galaxy clusters," Astronomy & Astrophysics **629**, A31, A31 (2019).

[108]VanderPlas J., Connolly A. J., Ivezić Ž., and Gray A., "Introduction to astroml: machine learning for astrophysics," in 2012 conference on intelligent data understanding (2012), pp. 47–54.

[109]Voit G. M., "Tracing cosmic evolution with clusters of galaxies," Reviews of Modern Physics **77**, 207–258 (2005).

[110]Weisskopf M. C., Tananbaum H. D., Speybroeck L. P. V., and O'Dell S. L., "Chandra x-ray observatory (CXO): overview," in SPIE proceedings, edited by J. E. Truemper and B. Aschenbach (July 2000).

[111]Werner G. R., Philippov A. A., and Uzdensky D. A., "Particle acceleration in relativistic magnetic reconnection with strong inverse-compton cooling in pair plasmas," Monthly Notices of the Royal Astronomical Society: Letters **482**, L60–L64 (2018).

[112]Werner N. and Mernier F., "Hot atmospheres of galaxies, groups, and clusters of galaxies," in *Reviews in frontiers of modern astrophysics; from space debris to cosmology* (2020), pp. 279–310.

[113]Werner N., Oonk J. B. R., Canning R. E. A., Allen S. W., Simionescu A., Kos J., van Weeren R. J., Edge A. C., Fabian A. C., von der Linden A., Nulsen P. E. J., Reynolds C. S., and Ruszkowski M., "The nature of filamentary cold gas in the core of the vigro cluster," The Astrophysical Journal **767**, 153 (2013).

[114]Wilms J., Allen A., and McCray R., "On the absorption of x-rays in the interstellar medium," The Astrophysical Journal **542**, 914–924 (2000).

[115]X-IFU, *X-ifu response matrices*, (2020) `http://x-ifu.irap.omp.eu/resources/for-the-community`, (accessed: 28.10.2022).

[116]XRISM Science Team, *Science with the x-ray imaging and spectroscopy mission (xrism)*, 2020.

[117]Yang H.-Y. K. and Reynolds Ch. S., "Interplay among cooling, agn feedback, and anisotropic conduction in the cool cores of galaxy clusters," The Astrophysical Journal **818**, 181 (2016).

[118]Yi Z. and Pan J., "Application of random forest to stellar spectral classification," in 2010 3rd international congress on image and signal processing, Vol. 7 (2010), pp. 3129–3132.

[119]Yip C. W., Connolly A. J., Vanden BerkD. E., Ma Z., Frieman J. A., SubbaRao M., A. S. Szalay, Richards G. T., Hall P. B., Schneider D. P., Hopkins A. M., Trump J., and Brinkmann J., "Spectral classification of quasars in the sloan digital sky survey: eigenspectra, redshift, and luminosity effects," The Astronomical Journal **128**, 2603 (2004).

[120]Young A. J., Wilson A. S., and Mundell C. G., "Chandra imaging of the x-ray core of the virgo cluster," The Astrophysical Journal **579**, 560–570 (2002).

[121]de Plaa J., Werner N., Simionescu A., Kaastra J. S., Grange Y. G., and Vink J., "Cold fronts and multi-temperature structures in the core of abell 2052," Astronomy & Astrophysics **523**, A81, A81 (2010).